

Optimal Estimation of Water Vapour Profiles using a Combination of Raman Lidar and Microwave Radiometer

Der Fakultät für Physik und Geowissenschaften

der Universität Leipzig

genehmigte

DISSERTATION

zur Erlangung des akademischen Grades

Doktor der Naturwissenschaften

Dr. rer. nat.

vorgelegt

von M.Sc. Andreas Foth

geboren am 11.08.1985 in Blankenburg (Harz) / Sachsen Anhalt

Gutachter: Jun.-Prof. Dr. Bernhard Pospichal
Prof. Dr. Susanne Crewell

Tag der Verleihung 10.07.2017

Bibliographische Beschreibung:

Foth, Andreas

Optimal Estimation of Water Vapour Profiles using a Combination of Raman Lidar and Microwave Radiometer

Universität Leipzig, Dissertation

109 S., 161 Lit., 48 Abb., 5 Tab.

Referat:

In der vorliegenden Arbeit wird ein zweistufiger Algorithmus, das sogenannte Retrieval, zur Ableitung von Wasserdampfprofilen aus einer Kombination von Ramanlidar und Mikrowellenradiometer zur operationellen Anwendung vorgestellt. Beide Instrumente kamen während einer groß angelegten Kampagne nahe Jülich im Frühjahr 2013 zum Einsatz (HOPE). Ziel der Arbeit ist es, kontinuierliche Zeitreihen der vertikalen Wasserdampfverteilung abzuleiten. Dies erfordert eine Kalibrierung des Ramanlidars. Im Rahmen dieser Arbeit wurde ein automatisches Kalibrierschema entwickelt, welches auf dem integrierten Wasserdampfgehalt abgeleitet aus Mikrowellenradiometermessungen basiert. Die Methode zeigt eine gute Übereinstimmung mit herkömmlichen Ansätzen, welche auf Radiosondenaufstiegen beruhen. Der Kalibrierfaktor ist sehr stabil mit einer relativen Abweichung von 5%. Diese Stabilität bietet den Vorteil, das Lidar auch unter bewölkten Bedingungen zu kalibrieren. Hierfür wird der Kalibrierfaktor des letzten wolkenfreien Zeitraums herangezogen. Dies ermöglicht die kontinuierliche Messung von Wasserdampfprofilen bis zu einer möglichen Wolkenbasis. Um verlässliche Wasserdampfinformationen innerhalb und oberhalb einer Wolke zu erhalten, wird ein zweistufiger Algorithmus angewandt. Der erste Schritt ist ein Kalman Filter, der die an der Wolkenbasis abgeschnittenen Wasserdampfprofile vom Ramanlidar mittels eines vorherigen Profils zu einem kompletten Profil (bis zu 10 km) kombiniert. Das komplette Wasserdampfprofil dient dann als Input für die eindimensionale variationelle (1D-VAR) Methode, auch als optimale Schätzung bekannt. Für dieses Profil werden die Helligkeitstemperaturen simuliert, die das Mikrowellenradiometer in der gegebenen Atmosphäre messen würde und anschließend mit den tatsächlich gemessenen verglichen. Das Profil wird dann iterativ entsprechend seiner Fehlerbalken so lange modifiziert, bis die modellierten mit den gemessenen Helligkeitstemperaturen hinreichend übereinstimmen. Die Funktionsweise des Retrievals wird mit Hilfe von Fallstudien unter verschiedenen Bedingungen detailliert beleuchtet. Eine statistische Analyse zeigt, dass die Verfügbarkeit von Ramanlidardaten (nachts) die Genauigkeit der abgeleiteten Profile verbessert. Tagsüber resultiert das Fehlen der Lidarinformationen in größeren Unterschieden zu Referenzradiosonden. Die Datenabdeckung der kompletten Lidarprofile von 17% während der zweimonatigen Kampagne wird durch Anwendung des Retrievals auf 60% signifikant erhöht. Da die relative Feuchte oftmals ein nützliches Maß für die Beschreibung von Wolkenbildung und Aerosolwachstum ist, wird die Bestimmung der relativen Feuchte aus den abgeleiteten Profilen unter verschiedenen Temperaturannahmen behandelt. Die Annahme eines Temperaturprofils vom Mikrowellenradiometer resultiert in einem absoluten Bias von 4.7 g kg^{-1} . Weiterhin wird in der Arbeit die flexible und vielfältige Anwendung des Retrievals an verschiedenen Messstationen in Jülich, Lindenberg und auf dem Forschungsschiff Polarstern sowie unterschiedlichen Ramanlidargeräten und Mikrowellenradiometern präsentiert. Ein besonders hervorzuhebender positiver Aspekt der Arbeit ist die Implementierung des Retrievals in die Cloudnet-Prozessierung, welche die Untersuchung von Wolken und Niederschlag bereichert. Die gewonnenen Profile werden außerdem für eine Evaluierung des Klima- und Vorhersagemodells ICON verwendet.

Bibliographic Description:

Foth, Andreas

Optimal Estimation of Water Vapour Profiles using a Combination of Raman Lidar and Microwave Radiometer

University of Leipzig, Dissertation

109 pp., 161 ref., 48 fig., 5 tab.

Abstract:

In this work, a two-step algorithm to obtain water vapour profiles from a combination of Raman lidar and microwave radiometer is presented. Both instruments were applied during an intensive two-month measurement campaign (HOPE) close to Jülich during spring 2013. The aim of the work is to retrieve a continuous time series of the vertical water vapour distribution. This requires a calibration of the Raman lidar. In the framework of this work an automated calibration scheme was developed that is based on the integrated water vapour derived by the microwave radiometer. This method shows good agreement with conventional approaches based on radiosonde launches. The determined calibration factor is very stable with a relative deviation of 5%. This stability offers a calibration of the Raman lidar even under cloudy conditions. In these cases, the calibration factor of the last clear sky interval is used. This enables the continuous observation of water vapour up to the cloud base, if present. To retrieve reliable water vapour information from inside or above the cloud a two-step algorithm is applied. The first step is a Kalman filter that enhances the profiles, truncated at cloud base, to the full height range (up to 10 km) by combining previous information and current measurement. Then the complete water vapour profile serves as input to the one-dimensional variational (1D-VAR) method, also known as optimal estimation. A forward model simulates the brightness temperatures which would be observed by the microwave radiometer for the given atmosphere. The profile is iteratively modified according to its error bars until the modelled and the actually measured brightness temperatures sufficiently coincide. The functionality of the retrieval is treated in detail by means of case studies under different conditions. A statistical analysis shows that the availability of Raman lidar data (night) improves the accuracy of the profiles. During the day, the absence of lidar data results in larger differences in comparison to reference radiosondes. The data availability of the full height lidar profiles of 17% during the two-month campaign is significantly enhanced to 60% by applying the retrieval. Since relative humidity often is a beneficial measure for the description of cloud formation and aerosol growth, the determination of the relative humidity from the derived profiles assuming different temperature profiles is treated. The assumption of temperature profiles from microwave radiometer results in an absolute bias of 4.7 g kg^{-1} . Additionally, this work presents the flexible and multifarious application of the retrieval to different measurement locations in Jülich, Lindenberg and aboard the research vessel Polarstern as well as to diverse Raman lidars and microwave radiometers. A highlight of the work is the implementation of the retrieval to the Cloudnet processing enhancing the investigations of clouds and precipitation. The retrieved profiles are used for an evaluation of the climate and prediction model ICON.

Contents

Zusammenfassung	iii
Abstract	iv
1 Introduction	1
2 Instrumentation and utilities	5
2.1 Experiment: locations and observations	5
2.1.1 HD(CP) ² Observational Prototype Experiment (HOPE)	5
2.1.2 OCEANET – Research vessel Polarstern	5
2.1.3 Richard Aßmann Observatory in Lindenberg (RAO)	6
2.2 Raman lidars	7
2.2.1 Polly ^{XT}	7
2.2.2 BASIL	9
2.2.3 RAMSES	10
2.3 Microwave radiometers	10
2.3.1 HATPRO	10
2.3.2 Radiometric profiler TP/WVP-3000	11
2.4 Radiosondes	12
2.4.1 Graw	12
2.4.2 Vaisala RS92	12
2.5 Cloudnet	12
2.6 ICON	13
2.7 GDAS	13
3 Theory and methodology	15
3.1 Lidar methodology	15
3.1.1 Lidar equation	15
3.1.2 Raman lidar method	16
3.1.3 Determination of water vapour mixing ratio	17
3.2 Microwave radiometry	19
4 Retrieval methodology	23
4.1 Definition of quantities	23
4.2 Kalman filter	25
4.3 Forward model	26
4.4 Liquid water assumption	28
4.5 Optimal estimation method (OEM)	29
5 Automatic Raman lidar calibration	35
5.1 Calibration methods	35
5.1.1 Regression method	35

5.1.2	Profile method	35
5.1.3	IWV method	36
5.2	Stability of the calibration factors	37
5.3	Water vapour measurements	39
5.3.1	Overview over Polly ^{XT} water vapour observations during HOPE	39
5.3.2	Comparison of water vapour measurements on 4 May 2013	40
5.3.3	Statistical analysis of calibrated profiles	40
5.3.4	Water vapour measurements below clouds	43
6	Retrieval application to LACROS platform during HOPE	45
6.1	Case Studies	45
6.1.1	Cloud free conditions	45
6.1.2	Cloudy conditions	49
6.2	Statistical analysis	52
6.3	Estimation of the relative humidity	59
7	Retrieval application to other data sets	63
7.1	BASIL – HOPE	63
7.2	Polly ^{XT} aboard of RV Polarstern – OCEANET	65
7.3	RAMSES at RAO	68
7.4	Retrieval implementation to Cloudnet	69
8	ICON model evaluation	73
8.1	ICON evaluation using OEM based on Polly ^{XT} at LACROS	73
8.2	ICON-LEM evaluation using OEM based on BASIL at JOYCE	73
9	Summary, conclusion and outlook	77
A	Appendix	81
A.1	Forward model error induced by liquid water	81
A.2	Additional formulas	81
A.3	Statistical analysis: differentiation between three initial conditions	82
	List of Figures	83
	List of Tables	85
	Bibliography	87
	Nomenclature	101
	Acknowledgements	107
	Curriculum Vitae	108

1 Introduction

In accordance with the latest report of the Intergovernmental Panel on Climate Change (IPCC) from 2013, water vapour plays a key role in the description of the thermodynamic state of the atmosphere [Hartmann *et al.*, 2013] and it is the most important greenhouse gas [Twomey, 1991]. Its amount in the atmosphere is controlled mostly by the air temperature, rather than by emissions. Therefore, tropospheric water vapour is considered as a feedback agent more than a forcing to climate change [Soden and Held, 2006]. The water vapour amount is highly variable in space and time, since it can considerably increase due to evaporation or decrease due to condensation and precipitation [Stevens and Bony, 2013]. Furthermore, the latent heat strongly influences the energy cycle. The typical residence time of water vapour in the atmosphere amounts to ten days [Myhre *et al.*, 2013]. Due to its spatio-temporal variability and its involvement in many atmospheric processes (e.g. cloud formation) it is difficult to properly implement water vapour in climate models [Held and Soden, 2000; Tompkins, 2002]. Spaceborne observations provide a global view of the water vapour distribution and are suitable to evaluate global climate models and to assess their uncertainties [Pierce *et al.*, 2006; Su *et al.*, 2006; Jiang *et al.*, 2010]. The Moderate Resolution Imaging Spectroradiometer (MODIS) is able to observe the integrated water vapour (IWV) during clear sky conditions [Gao and Kaufman, 2003; Seemann *et al.*, 2003]. Based on passive microwave radiometry, water vapour profiles [Aires *et al.*, 2013; Bernardo *et al.*, 2013] as well as the column integrated liquid water path (LWP) can be retrieved [O'Dell *et al.*, 2008]. However, spaceborne microwave radiometry is mostly available over the sea. Additionally, the vertical and temporal resolution of spaceborne observations is limited preventing a detailed evaluation.

In the last decades, models have been increased their spatial and vertical resolution, more atmospheric processes have been incorporated and the parametrisations of physical processes have been improved [Randall *et al.*, 2007]. In order to evaluate and improve model forecasts, parametrisation schemes and satellite retrievals, the observations need to be enhanced. Uncertainties in both observations and modelling of water vapour strongly affect the representation of clouds and precipitation in climate models and predictions. For that reason the German research project High Definition Clouds and Precipitation for advancing Climate Prediction (HD(CP)²) was initiated aiming to improve the clouds and precipitation representation in models and to quantify the errors associated¹. One part within the HD(CP)² initiative was the intensive observation campaign HD(CP)² Observational Prototype Experiment (HOPE) in Jülich [Macke *et al.*, 2016]. Data from this campaign will be mainly used in this work which presents a retrieval of water vapour profiles from ground-based remote sensing. During HOPE, different remote sensing instruments to measure water vapour, both active and passive, were deployed.

An active method is given by the Raman lidar technique [Ansmann *et al.*, 1992; Whiteman *et al.*, 1992; Wandinger, 2005]. Water vapour mixing ratio has been determined for several

¹<http://hdcp2.eu>

decades using this technique [Melfi *et al.*, 1969; Cooney, 1970; Melfi, 1972]. However, with advancing technology Raman lidars enabled high vertical resolution measurements of water vapour and extended their range to the whole troposphere [Ferrare *et al.*, 1995; Sherlock *et al.*, 1999; Di Girolamo *et al.*, 2009; Leblanc *et al.*, 2012], during daytime [Renaut *et al.*, 1980; Ferrare *et al.*, 2006] or automatically [Goldsmith *et al.*, 1998; Turner *et al.*, 2002]. However, water vapour Raman lidars need to be calibrated with an instrument measuring simultaneously for example a microwave radiometer (MWR) or radiosonde (RS) [Mattis *et al.*, 2002; Madonna *et al.*, 2011; Foth *et al.*, 2015]. Another possibility to observe high resolution water vapour profiles is provided by the differential absorption lidar (DIAL) technique [Browell *et al.*, 1979; Bösenberg, 2005]. DIAL systems are well suited for ground-based boundary layer studies during daytime [Bösenberg and Linné, 2002] or airborne applications [Wirth *et al.*, 2009; Bruneau *et al.*, 2001a,b]. Although DIAL systems do not require calibrations, they are costly to apply. Both Raman lidar and DIAL methods were applied in several field studies [Weckwerth *et al.*, 2004; Whiteman *et al.*, 2006b; Wulfmeyer *et al.*, 2011; Bhawar *et al.*, 2011]. However, lidars were mainly used as research instruments that did not work unattended or automatically on a routine basis.

One major drawback of Raman lidars (or DIAL systems) is that they do not provide any water vapour information from inside the cloud or above due to the strong signal attenuation, especially in liquid clouds. Hence, lidar measurements are limited from the surface to the cloud base. Furthermore, daytime measurements are limited in height due to the presence of scattered solar radiation [Turner and Goldsmith, 1999].

Another approach is to use passive remote sensing to sound the thermodynamic state of the atmosphere. Passive microwave radiometry can provide atmospheric water vapour observations with high temporal resolution, but limited vertical information [Solheim *et al.*, 1998; Westwater *et al.*, 2005]. However, the IWV can be retrieved very accurately. Microwave radiometers can be operated during all weather conditions except for precipitation [Güldner and Spänkuch, 1999]. Like for many remote sensing techniques accurate calibrations are crucial for obtaining precise measurements [Maschwitz *et al.*, 2013; Kuchler *et al.*, 2016]. Moreover, infrared spectrometry shows high potential for retrieving humidity, especially in the boundary layer [Löhnert *et al.*, 2009]. Another possibility to passively observe the IWV is given by sun photometry [Thome *et al.*, 1992; Alexandrov *et al.*, 2009]. Since sun photometers measure the direct sunlight, their retrievals are limited to daytime and cloud free conditions. Global positioning system (GPS) ground stations are also able to provide IWV information but with low spatial representativeness [Dick *et al.*, 2001; Gendt *et al.*, 2004].

In contrast to the already presented remote sensing observations water vapour profiles can be measured in-situ using RS [Miloshevich *et al.*, 2006]. RS launches are mostly performed by the national weather services and usually twice a day. Therefore, the horizontal and temporal resolution of routine measurements are rather low. However, these profiles can serve as reference for remote sensing observations.

As described above, it is a challenge to provide continuous high-resolution water vapour profiles with a single instrument at a sufficient resolution. In recent years, several supersites, like the Jülich Observatory for Cloud Evolution (JOYCE) [Löhnert *et al.*, 2015], the Leipzig Aerosol and Cloud Remote Observations System (LACROS) [Bühl *et al.*, 2013] and the Richard Assmann Observatory (RAO), installed a combination of ground-based remote sens-

ing systems. The synergy of complementary information from both active and passive instruments can provide a more comprehensive understanding of atmospheric processes [Stankov, 1998; Furumoto et al., 2003; Bianco et al., 2005; Delanoë and Hogan, 2008]. From a combination of radar reflectivities and liquid water path from MWR, Frisch et al. [1998] successfully derived liquid water content (LWC) profiles. Han and Westwater [1995] significantly improved the retrieval of water vapour and cloud liquid by using a combination of MWR, radio acoustic sounding system (RASS), ceilometer and surface meteorology instead of a single MWR. Later on, Han et al. [1997] presented a method based on a Kalman Filter [Kalman, 1960; Kalman and Bucy, 1961] that incorporates current and past measurements followed by a statistical inversion that combines the lidar with the radiometer measurement. Additionally, the inclusion of in-situ measurements in a combination of remote sensing systems improves the results [Westwater, 1997]. The Cloudnet project comprises of a number of algorithms for the continuous analysis of cloud properties by means of remote sensing with lidar, MWR and cloud radar [Illingworth A. J. et al., 2007]. The combination enables the continuous evaluation of the representation of clouds in climate and weather forecast models [Sengupta et al., 2004; Hogan et al., 2009; Bouniol et al., 2010]. Additionally, the data set enables the development and validation of new cloud remote sensing synergy algorithms.

Löhnert et al. [2004, 2008] developed the so-called integrated profiling technique (IPT) that integrates a ground-based MWR, a cloud radar and a priori information, e.g. from RS. This approach enables the derivation of temperature, humidity and liquid water content profiles [Ebell et al., 2010] and their associated error estimates. The IPT is based on a variational scheme, also known as optimal estimation [Rodgers, 2000]. Cimini et al. [2010] as well as Hewison and Gaffard [2006] used a similar approach as Löhnert et al. [2004] but with background information from a short-range numerical weather prediction model instead of RS climatology.

The synergy of Raman lidar and MWR is beneficial for continuously observing the vertical water vapour distribution. When both Raman lidar and MWR are measuring collocated and simultaneously, continuous water vapour profiles can be obtained operationally [Ferrare et al., 2006; Adam and Venable, 2007; Adam et al., 2010]. However, the Raman lidar needs to be calibrated on a routine basis. A calibration method that is based on the IWV from MWR is suited for this issue [Foth et al., 2015]. In previous approaches the total precipitable water from MWR in combination with RS has been used to calibrate the water vapour Raman lidar [Turner and Goldsmith, 1999; Turner et al., 2002]. Calibration methods only based on RS [England et al., 1992; Mattis et al., 2002; Reichardt et al., 2012] are inappropriate for continuous monitoring of the tropospheric water vapour with Raman lidar because of their low spatial and temporal resolution.

The aim of the work presented in this thesis is to develop a two-step algorithm that combines a Raman lidar and a MWR by using an optimal estimation approach. The retrieval can be seen as an extension of the IPT by Löhnert et al. [2009]. Barrera-Verdejo et al. [2016] also generated a variational retrieval based on these two instruments. On a first glance, both approaches seem to be similar, but they are fundamentally different with regard to the optimal estimation method. Barrera-Verdejo et al. [2016] used both, Raman lidar and MWR, as part of the observation vector. Since the water vapour profiles from Raman lidar are strongly disturbed by clouds, they are truncated at the cloud base. In the present work, the truncated Raman lidar profiles are extended to the full height range by using a Kalman Filter in a first step. Then the Kalman-filtered profiles serve as input to the optimal estimation.

This approach is based on the studies of *Schneebeili [2009]*. Additionally, the focus of the presented work is to routinely retrieve a continuous time series of water vapour profiles during all non-precipitating conditions and to implement this retrieval into the Cloudnet processing.

The thesis is outlined as follows: Chapter 2 gives a detailed description of the experiments, the used instrumentation and utilities. Chapter 3 presents the Raman lidar methodology and its ability for water vapour profiling as well as the theory of microwave radiometry. The retrieval methodology including the Kalman filter and the optimal estimation are introduced in Chapter 4. The automated calibration of the Raman lidar only based on the IWV from a collocated MWR is presented in Chapter 5. The calibration scheme is designed in a very straightforward way to offer a broad application. It enables the determination of water vapour profiles up to cloud base, if present, during all non-precipitating conditions on a routine basis. This issue has already been published in *Foth et al. [2015]*. Chapter 6 shows the results of a comprehensive evaluation of the two-step algorithm combining the Raman lidar mass mixing ratio with the MWR brightness temperatures. The functionality of the retrieval is shown in detail by means of cloud free and cloudy cases and in dependency of Raman lidar data availability. Afterwards, the accuracy of the retrieved profiles is evaluated based on RS launches during the HOPE campaign. Additionally, the derivation of relative humidity is presented since it is a useful atmospheric measure for the investigation of cloud formation or aerosol hygroscopic growth. Chapter 7 describes the manifold application of the retrieval using different lidar systems and MWR at diverse observation platforms such as JOYCE, RAO or even the research vessel Polarstern. This chapter also includes a description of the implementation of the algorithm into the Cloudnet processing. The high vertical and temporal resolution of the retrieved profiles enable the evaluation of numerical weather prediction and climate models. Such a comparison is represented in Chapter 8 by using the ICON model. Finally, the thesis is completed with a summary, conclusion and outlook in Chapter 9.

2 Instrumentation and utilities

The application of the water vapour retrieval method that is developed in this work requires different ground-based remote sensing instruments such as MWR and Raman lidar. For the evaluation of the retrieval collocated RS launches are important. These data were gathered at several supersites as well as during specialised measurement campaigns and is summarised in Tab. 2.1. In the following sections the experiments and campaigns are explicated in detail.

2.1 Experiment: locations and observations

2.1.1 HD(CP)² Observational Prototype Experiment (HOPE)

In the framework of the HD(CP)² initiative HOPE was conducted around Jülich in western Germany during April and May 2013. This campaign is explained in detail in [Macke et al. \[2016\]](#). The goal of HOPE was to probe the atmosphere with a specific focus on the development of clouds and precipitation. HOPE was further conceived for a critical model evaluation and to provide informations on sub-grid variability and microphysical properties. Figure 2.1 illustrates the area around Jülich and specifies some instruments. Two observatories were set up in addition to JOYCE [[Löhnert et al., 2015](#)]. The LACROS site [[Wandinger et al., 2012](#); [Bühl et al., 2013](#)] was temporarily built up in Krauthausen which is about 4 km south of JOYCE. Both JOYCE and LACROS observatories are equipped with a set of active and passive remote sensing instruments such as lidars and MWRs which allow the application of the proposed retrieval. Radiosondes were launched in Hambach (KIT station [[Maurer et al., 2016](#)]) which is about 4 km away from JOYCE and LACROS. Furthermore, a 120 m tower provide surface meteorological data as pressure, temperature and humidity.

2.1.2 OCEANET – Research vessel Polarstern

The OCEANET project is a shipborne facility to investigate continuously both, the energy and material transport, between atmosphere and ocean [[Macke et al., 2010](#)]. The OCEANET platform is the German research vessel Polarstern that is mostly operating under summer

Table 2.1: Overview over the instrumentation at various experiments.

Experiment	HOPE	HOPE	OCEANET	RAO	Cloudnet
Platform	LACROS	JOYCE	RV Polarstern	—	LACROS
Location	Krauthausen	Jülich	Atlantic	Lindenberg	Krauthausen
Raman Lidar	Polly ^{XT}	BASIL	Polly ^{XT} Arielle	RAMSES	Polly ^{XT}
MWR	HATPRO	HATPRO	HATPRO	Radiometrics MP profiler	HATPRO
RS	Graw	Graw	Vaisala RS92	Vaisala RS92	Graw

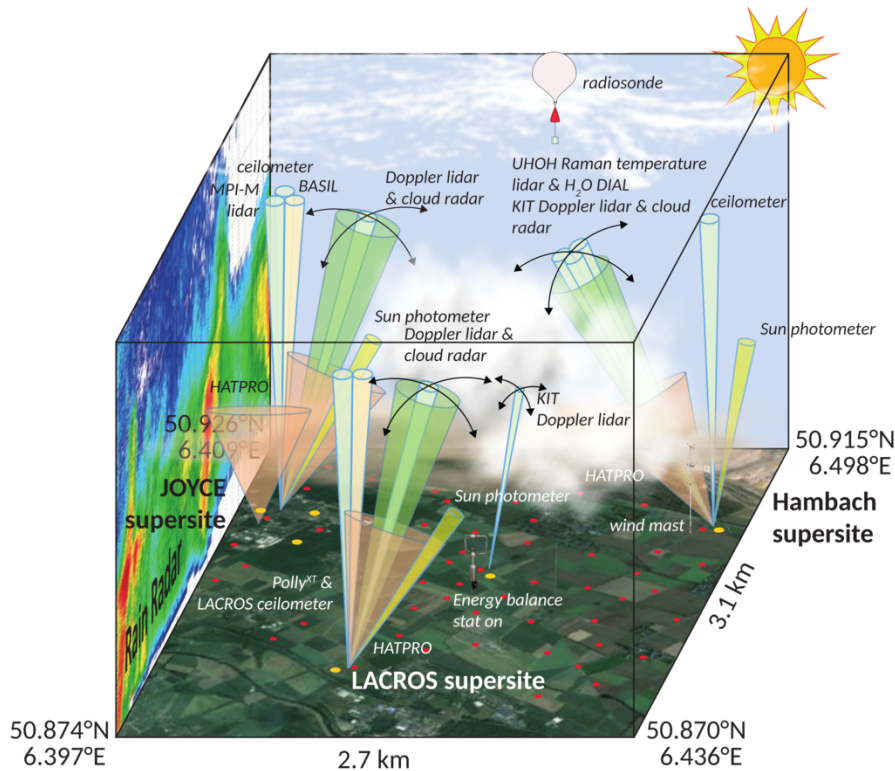


Figure 2.1: HOPE 3D instruments map. Courtesy of Patric Seifert and Katja Schmieder, TROPOS

polar conditions either in the Arctic or in the Antarctic. The resulting transfer cruises provide an ideal opportunity to perform atmospheric observations over different climate conditions including tropical, subtropical and midlatitudinal conditions in both hemispheres. During several cruises the radiative effect of aerosols [Kanitz *et al.*, 2013b] and their vertical distribution [Kanitz *et al.*, 2013a] over the Atlantic as well as the impact of aerosol on heterogeneous cloud formation [Kanitz *et al.*, 2011] were intensively investigated. Furthermore, estimations of the cloud coverage [Kalisch, 2011] and the derivation of cloud microphysical properties [Zoll, 2012; Brückner *et al.*, 2014] were performed.

On the cruise leg ANT-XXIX/10 from 8 March to 14 April 2014 between Cape Town (South Africa) and Bremerhaven (Germany), the OCEANET measurement container was equipped with the Raman lidar Polly^{XT} and the microwave radiometer HATPRO. The container was located on the the helicopter deck close to the stern of the ship. Surface meteorology and the GPS position are available from a weatherstation on the upperdeck.

2.1.3 Richard Aßmann Observatory in Lindenberg (RAO)

The Richard Aßmann observatory (RAO) in Lindenberg, also known as meteorological observatory Lindenberg (MOL), is operated by the German weather service (DWD) in the south east of Berlin, Germany. Its key mission is the vertical sounding of the atmosphere in order to provide a reference data set on the physical structures and processes in the atmosphere – the so-called *Lindenberg column* [Beyrich and Engelbart, 2008]. The observatory offers, amongst others, measurements of a Raman lidar for atmospheric moisture sensing

(RAMSES) [Reichardt *et al.*, 2012] and a multichannel radiometric profiler of temperature, humidity, and cloud liquid (TP/WVP-3000) [Ware *et al.*, 2003]. The surface meteorology as temperature, pressure and humidity is provided by the MWR.

2.2 Raman lidars

In the following section the Raman lidars which are used in this work are explained. Especially Polly^{XT} is explained in detail because it is the main lidar in this work measuring 24/7¹ and it provided the most complete data. Moreover, the proposed retrieval based on Polly^{XT} data at LACROS, is illustrated and presented by means of case studies and a statistical analysis (Chapter 6).

2.2.1 Polly^{XT}

Polly^{XT} (Portable lidar system extended) is a fully automatic portable multiwavelength Raman and polarisation lidar [Althausen *et al.*, 2009]. The optical set-up is illustrated in Fig. 2.2. The lidar is a biaxial system. The Nd:YAG laser generates pulses at 1064, 532 and 355 nm with a repetition rate of 20 Hz. The emitter unit contains the laser head and the second- and third harmonic-generator (SHG, THG). The beam is redirected by prisms (E1) into the beam expander (E2) which decreases the beam divergence to less than 2 mrad. The light at 532 nm is linearly polarized.

The backscattered photons are collected by a Newtonian telescope (R1) with a diameter of 300 mm. The secondary mirror (R2) directs the light to a pinhole (R3) that defines the

¹Continuously 24 h a day, 7 days per week.

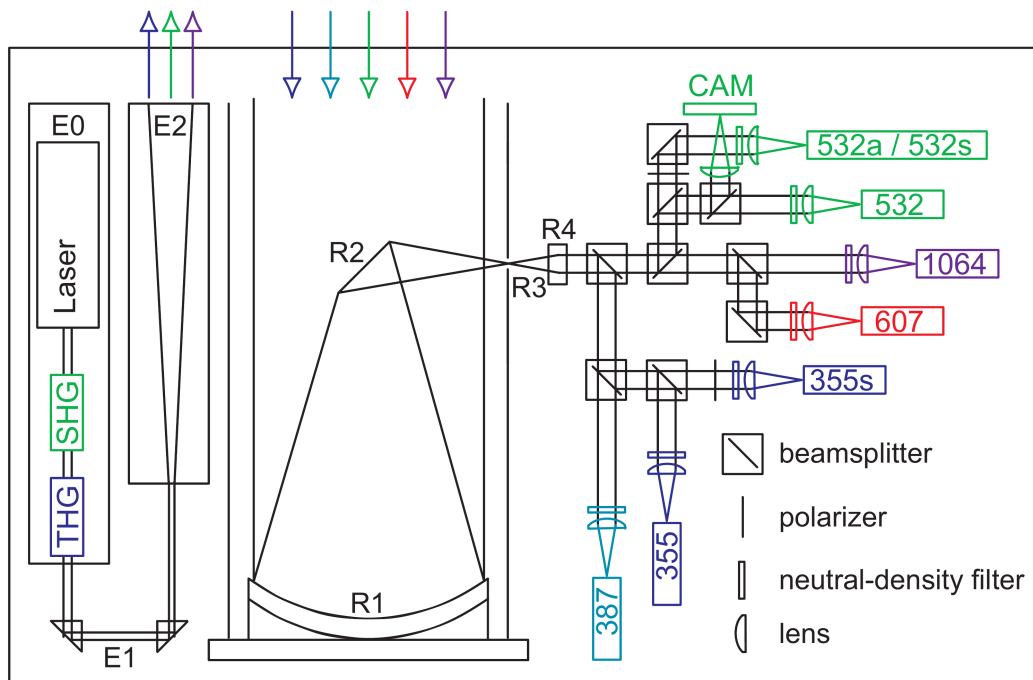


Figure 2.2: Optical set-up of Polly^{XT} [Kanitz, 2012]. Details are explained in the text.



Figure 2.3: Polly^{XT} cabinet with open doors: (1) roof cover, (2) sensors for outdoor temperature, air pressure and rain, (3) air condition, (4) uninterruptible power supply, (5) computer with data acquisition, (6) laser power supply, (7) laser head, (8) beam expander, (9) receiver telescope and (10) receiver with seven channels [Baars, 2012].

the receiver field-of-view of 1 mrad. An achromatic lens collimates and transmits the light to the right part of the receiver unit (right side in Fig. 2.2). Herein, the light is separated by dichroic and polarising beam splitters into the three elastically scattered wavelengths at 1064, 532 and 355 nm, the Raman-shifted wavelengths of the nitrogen molecule at 607 and 387 nm and of the water vapour molecule at 407 nm, the cross polarised signal component at 532 nm and a camera (CAM). The camera is used to adjust the laser beam to the receiver field-of-view. In front of each photo multiplier tube absorptive neutral density filters and planconvex lenses are placed which attenuate the received light to proper count rates and focus the beam to the detection area of the photomultipliers, respectively. The signals of the photon counting are adapted to the data acquisition. The recorded profiles are averaged and stored over 30 m in height and 30 s in time.

The whole system is built in a waterproof air-conditioned telecommunication cabinet 2.3. In the roof two quartz plates are installed to avoid exchange with ambient air and to enable an undisturbed penetration of the emitted and received light. These plates can be protected by an automatic roof cover (1) which is controlled by the computer (5) using the rain sensor (2). During precipitation the roof cover closes, the laser shuts down and the data acquisition (5) and measurement stops. The air-condition (3) maintains a stable temperature inside the cab-

inet. The main computer and the laser power supply (6) are connected to the uninterruptible power supply (4) to bypass short power failures. The laser head (7), beam expander (8), receiver telescope (9) and the wavelength separation unit (10) are tilted by 5° off zenith to avoid specular reflections on horizontally aligned planar ice crystals [Westbrook *et al.*, 2010; Seifert, 2010]. The whole system is controlled by the computer and can be operated remotely.

From the 387 and the 407 nm Raman-channel water vapour profiles can be determined (see section 3.1.3). In the lowermost heights the overlap of the laser beam with the receiver field-of-view of the bistatic system is incomplete. However, the overlap of both Raman channels is assumed to be identical and for that reason the overlap effect is negligible regarding water vapour measurements. Nevertheless, the lowermost 400 m of the signal ratio are set constant to account for the overlap problem. During daytime, no water vapour measurements can be performed due to the high daylight background.

The OCEANET Polly^{XT} version that is described in Engelmann *et al.* [2016] is very similar to the one presented above, but with another vertical raw resolution of 7.5 m.

The Polly^{XT} raw data is processed and calibrated to mixing ratio profiles as explained in Sec. 3.1.3. These calibrated water vapour profiles are then used for the proposed retrieval.

An overview of the comprehensive area of operation and the automated measurement capabilities of Polly systems all over the world is extensively introduced by Baars *et al.* [2016]. The observations are conducted by the lidar group from the Leibniz Institute for Tropospheric Research (TROPOS) and are presented online at <http://polly.tropos.de>.

2.2.2 BASIL

The University of Basilicata lidar system (BASIL) has been developed by the Engineering School (formerly the Department of Environmental Engineering and Physics) of the University of Basilicata in Potenza. The principal set-up of BASIL and Polly^{XT} is similar. However, BASIL performs high resolution and accurate measurements of atmospheric water vapour and temperature. In contrast to Polly^{XT} the more powerful laser of BASIL enables water vapour measurements also during daytime. A thorough description of the technical characteristics, measurement capabilities and performances is given in Di Girolamo *et al.* [2016]. For water vapour measurements BASIL uses the same wavelengths as Polly^{XT}. The maximum vertical and temporal resolution are 7.5 m in height and 1 s in time, respectively, and can be traded-off to improve the measurement precision. Due to the use of a non-paralyzable counting system and the high count rate of the BASIL measurements, a dead time correction is applied. For an automated analysis of the BASIL data only the digital signals are used. For that reason a dry bias in the lowermost 500 m is expected. The accuracy of the profiles could be improved by *gluing* the analogue and the digital signals [Whiteman *et al.*, 2006a; Newsom *et al.*, 2009], but this approach is not considered in this work which is focussed on demonstrating the automated calibration procedure (see Chapter 5). This in order to simplify the data analysis procedure and allow an easier implementation of the automated calibration procedure. Additionally, the lowermost 100 m of the signal ratio are assumed to be well mixed and are set constant to account for the overlap problem

For the application of the water vapour retrieval (Sec. 7.1) already calibrated mixing ratio profiles from the HD(CP)² database are used. The calibration of this data is based on

RS profiles.

2.2.3 RAMSES

The Raman lidar for atmospheric moisture sensing (RAMSES) provides unattended continuous multiparameter atmospheric profiles. A detailed description of the technical characteristics and measurement application is given by *Reichardt et al. [2012]*. RAMSES uses a seeded frequency-tripled Nd:YAG laser and emits laser pulses at 355 nm. The backscattered light is collected by a far range telescope with a diameter of 790 mm and a near range telescope with a diameter of 200 mm. Water vapour mixing ratio is also retrieved using the inelastic backscatter at 387 and 407 nm. Under favourable conditions water vapour can be retrieved up to 14 km during the night and up to 5 km at daytime. The water vapour data used in the retrievals is already calibrated by means of RS profiles. The overlap height amounts to 200 to 300 m during the night and around 1 km at daytime. The time resolution of the used data is 10 min.

In addition RAMSES is able to retrieve temperature profiles as well as optical particle parameters which are not considered in this work.

2.3 Microwave radiometers

2.3.1 HATPRO

The humidity and temperature profiler (HATPRO), built by Radiometer Physics GmbH, Germany, is a passive instrument that measures atmospheric emission at two frequency bands in the microwave spectrum (see also 3.2). Seven channels are along the 22.235 GHz H₂O absorption line. From these observations humidity information can be retrieved. The seven channels of the other band from 51 to 58 GHz along the O₂ absorption complex contain the vertical temperature profile information. The fully automatic microwave radiometer HATPRO allows to derive temperature and humidity profiles as well as integrated quantities such as IWV and liquid water path (LWP) with a high temporal resolution up to 1 s [*Rose et al., 2005*]. Their uncertainties amount to 0.5 kg m⁻² for IWV [*Steinke et al., 2015*] and to 22 g m⁻² for low LWP values and increase up to 45 g m⁻² for LWP values higher than 500 g m⁻², respectively [*Ebell et al., 2011*]. Observations are possible during nearly all weather conditions except precipitation.

To retrieve atmospheric quantities from the measured brightness temperatures, statistical algorithms were used by means of a multi-linear regression between modelled brightness temperatures and atmospheric profiles. Both MWRs from JOYCE and LACROS use the same retrieval algorithms which are based on a long-term dataset of De Bilt radiosondes [*Löhnert and Crewell, 2003*]. The accuracy of the temperature information in the planetary boundary layer can be enhanced through measurements at different elevation angles [*Crewell and Löhnert, 2007*]. The scan mode requires horizontally homogeneous atmospheric conditions in the direct horizontal vicinity (~ 3 km).

Weighting functions, also called Jacobians, are well suited to describe the ability for humidity profiling. Figure 2.4 shows the weighting functions for the seven HATPRO frequencies along the H₂O absorption band. Generally, the measured brightness temperature does not originate from an isolated height level. The weighting function describe the contribution of

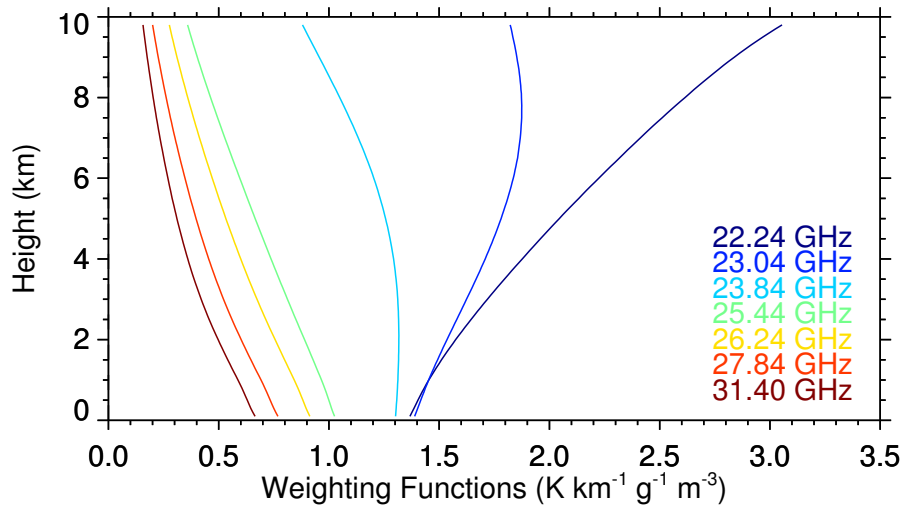


Figure 2.4: Absolute humidity weighting function for the HATPRO frequencies for a cloud free model atmosphere.

a certain height. Three weighting functions (22.24, 23.04 and 23.84 GHz) differ considerably from each other. However, the others have a similar shape as the atmosphere is optically thin at these frequencies. For that reason they add less information to the vertical distribution of humidity. Ideally, the weighting functions are peaked functions and several frequencies contribute information from different height levels. Nevertheless, the HATPRO frequencies provide limited vertical distribution.

The usage of the 31 GHz channel of both LACROS and JOYCE HATPRO instruments caused unrealistic results. The reason for that behaviour was not identified but might be induced by the forward model.

2.3.2 Radiometric profiler TP/WVP-3000

The TP/WVP-3000 is a commercially available radiometric 12 channel profiler built by Radiometrics Corp. Boulder, CO, USA [Ware et al., 2003]. 4 channels in the water vapour absorption band are used for humidity profiling. Humidity and temperature profiles, as well as IWV and LWP are also retrieved using statistical algorithms or neural networks. The time resolution of the data provided by the RAO team amounts to 10 min. This relatively long integration time might lead to enhanced errors due to changes in the atmosphere. Especially the LWP value is critical because its variation within a 10 min interval can be large caused by passing clouds. This is an error source that should be taken into account when interpreting the according results. It also provides surface meteorology as temperature, pressure and humidity.

Both introduced radiometers provide brightness temperatures and surface humidity which form the observation vector in the optimal estimation algorithms. The MWR humidity profiles are only used for comparisons, whereas the temperature profiles are used in the forward model (see Sec. 4.3).

2.4 Radiosondes

2.4.1 Graw

During HOPE, radiosondes (RS) were launched minimum twice a day (11:00 and 23:00 UTC) and more often during intensive observation periods (IOP) at the KITCube site in Hambach. The RS (type Graw DFM-09) measures temperature, humidity, pressure and wind velocity [Nash *et al.*, 2011; Wang and Zhang, 2008]. Due to the vicinity of the RS station to the open-cast mining and its depth of nearly 400 m, horizontal inhomogeneities between the RS and the lidar locations are likely (Fig. 2.1).

2.4.2 Vaisala RS92

At both, RV Polarstern and RAO, the Vaisala RS92 were used that measures standard meteorological properties as humidity, pressure and temperature. Daily RS launches at Polarstern were performed at the helicopter deck (10 m asl). At RAO RS are launched four times a day every 6 h. The GCOS (Global Climate Observing System) Reference Upper-Air Network (GRUAN) data processing for RS92 was developed to achieve the criteria for reference measurements. Therefore, also a ground-check is performed [Dirksen *et al.*, 2014].

2.5 Cloudnet

Cloudnet is a framework for the continuous observation of cloud properties based on three main remote sensing instruments: MWR, cloud radar and ceilometer (lidar) [Illingworth *A. J. et al.*, 2007]. Goals of Cloudnet² are:

- To optimise the use of existing data sets to develop and validate new cloud remote sensing synergy algorithms.
- To continuously evaluate the representation of clouds in climate and weather forecast models.
- To demonstrate the potential of an operational network to improve the representation of clouds in models.

The idea behind is to have a standardised procedure to retrieve consistent cloud properties at different stations:

- Cabauw, Netherlands
- Leipzig, Germany
- Potenza, Italy
- Chilbolton, UK
- Lindenberg, Germany
- Sodankyla, Finland.
- Hyttiälä, Finland
- Mace Head, Ireland
- Jülich, Germany
- Palaiseau, France
- several others

In the Cloudnet processing features are classified according to their optical properties. It is distinguished, amongst others, between ice, cloud droplets, drizzle or rain, supercooled droplets etc. For each target a radar and lidar detection status is stated. Furthermore, one can extract drizzle, ice water content and **LWC** profiles. In this work, the retrieval is implemented into the Cloudnet processing at the temporarily LACROS site in Krauthausen during HOPE. Quicklooks³ of the Cloudnet processed data at the permanent LACROS site

²<http://www.cloud-net.org/>

³<http://www.cloud-net.org/quicklooks/>

at TROPOS in Leipzig are presented on the LACROS webpage⁴.

2.6 ICON

The DWD and the Max Planck Institute for Meteorology jointly developed the icosahedral nonhydrostatic (ICON) modelling framework [Zängl *et al.*, 2015]. It is a next generation numerical weather prediction (NWP) and climate model and has a grid size of 13 km with 90 vertical layers up to 75 km height. The HD(CP)² model is called ICON-LEM (ICON Large-Eddy Model), which is a modified version of the ICON-NWP branch. ICON-LEM was developed within the framework HD(CP)² and is constantly updated. ICON-LEM provide data with three different resolutions based on three domains. The humidity taken from the ICON-LEM data has a resolution of 9 s in time and 156 m in space. The vertical resolution amounts to 150 layers from surface to 21 km with highest resolution from 24 m near the surface up to 355 m. The high resolution allows to explicitly resolve processes that are even parameterised in the consortium for small-scale modelling (COSMO) simulations [Baldauf *et al.*, 2011] and to represent processes on a subgrid-scale for regular numerical weather prediction and climate models. Heinze *et al.* [2016] present a comprehensive evaluation of large-eddy simulations with ICON during HOPE. They focus on assessing the moist processes including cloud-, precipitation- and convection dynamics, cloud- and precipitation microphysical processes as well as boundary layer dynamics. Until the completion of the presented work, ICON-LEM runs provide data for six specific days during HOPE: 20, 24, 25, 26 April, 2 and 11 May 2013.

2.7 GDAS

The Global Data Assimilation System (GDAS)⁵ is a publicly available free of charge archive of modelled and assimilated meteorological informations with a resolution of 1° latitude and longitude. This data set provides temperature and relative humidity profiles for the comparison study in Sec. 6.3. A detailed description about GDAS and a comparison with RS is given in Abreu *et al.* [2012].

⁴<http://lacros.rsd.tropos.de/cloudnet/cloudnet.php>

⁵<http://ready.arl.noaa.gov/gdas1.php>

3 Theory and methodology

3.1 Lidar methodology

In this Section, the lidar principles are introduced. A Raman lidar emits laser pulses and receives the backscattered photons. In this way, aerosol, clouds or trace gases can be observed throughout the troposphere. The method to derive water vapour presented in this chapter especially section 3.1.3 is already described and presented in *Foth et al. [2015]* without explicitly citing.

3.1.1 Lidar equation

The basic equation for all lidar applications is the lidar equation which relates the emitted and received power of the lidar:

$$P_{\lambda}(r) = P_{0,\lambda} \underbrace{\frac{t_p c A_T \eta_{\lambda}}{2}}_{\text{I}} \underbrace{\frac{O_{\lambda}(r)}{r^2}}_{\text{II}} \underbrace{\beta_{\lambda}(r)}_{\text{III}} \underbrace{\exp \left\{ -2 \int_0^r \alpha_{\lambda}(\xi) d\xi \right\}}_{\text{IV}}. \quad (3.1)$$

The lidar equation is described in more detail in *Wandinger [2005]*. The parameters in Eq. 3.1 denote:

- λ the wavelength of detection,
- r the range from the lidar receiver,
- $P_{\lambda}(r)$ the received power from the range r ,
- $P_{0,\lambda}$ the emitted power at wavelength λ_0 ,
- t_p the temporal pulse length,
- c the speed of light,
- A_T the area of the receiver telescope,
- η_{λ} the transmission efficiency of the lidar receiver,
- $O_{\lambda}(r)$ the overlap function,
- $\beta_{\lambda}(r)$ the backscatter coefficient and
- $\alpha_{\lambda}(r)$ the extinction coefficient.

Beside the emitted laser power $P_{0,\lambda}$, Eq. 3.1 consists of four terms which are explained in the following paragraphs.

Term I combines the range-independent parameters of the lidar system and is usually called system-efficiency term E_{λ} . The area of the telescope A_T dictates the solid angle A_T/r^2 of the cone of volume of signal detection.

Term II includes the geometrical effects. $O_{\lambda}(r)$ describes the overlap of the laser beam with the receiver field of view and depends on the geometrical properties of the receiver telescope. A complete overlap is defined as $O_{\lambda}(r) = 1$. Below this height which usually varies between a few hundred meters and several kilometers, the signal has to be corrected by means of the overlap function $O_{\lambda}(r) < 1$ [*Wandinger and Ansmann, 2002*].

Term III consists of the the backscatter coefficient $\beta_\lambda(r)$ that describes the amount of light which is scattered by particles and molecules at 180° from the range r .

Term IV, the transmission term, accounts for the attenuation of light along its path through the atmosphere caused by absorption and scattering. According to Lambert-Beer's law it depends on the extinction coefficient $\alpha_\lambda(r)$ and on the path. In case of lidar the path is twice the distance between the instrument and the scattered volume.

Absorption and scattering are both caused by molecules (superscript m) and particles (superscript p):

$$\alpha(r) = \alpha_\lambda^m(r) + \alpha_\lambda^p(r) \quad (3.2)$$

$$\beta(r) = \beta_\lambda^m(r) + \beta_\lambda^p(r). \quad (3.3)$$

The vertical integration over the particle extinction coefficients $\alpha_\lambda^p(r)$ from the instrument to the maximum measurement height (e.g. cloud base or tropopause) at different wavelengths results in the aerosol optical depth (AOD)

$$\text{AOD}_\lambda = \int_0^{r_{\max}} \alpha_\lambda^p(r) dr. \quad (3.4)$$

The relation between the extinction $\alpha_\lambda(r)$ and backscatter coefficient $\beta_\lambda(r)$ is denoted as lidar ratio S (i.e. extinction-to-backscatter ratio):

$$S_\lambda^p(r) = \frac{\alpha_\lambda^p(r)}{\beta_\lambda^p(r)} \quad (3.5)$$

$$S_\lambda^m(r) = \frac{\alpha_\lambda^m(r)}{\beta_\lambda^m(r)} = \frac{8\pi}{3} K. \quad (3.6)$$

K indicates the King factor [Collis and Russell, 1976]. $\beta_\lambda^m(r)$ and $\alpha_\lambda^m(r)$ can be calculated by given temperature and pressure profiles [Bucholtz, 1995]. Nevertheless, the lidar equation (Eq. 3.1) comprises two unknowns ($\beta_\lambda^p(r)$ and $\alpha_\lambda^p(r)$) and is under-determined. Two common approaches are usually used to solve the lidar equation. First, the Klett method is based on the assumption of a constant height independent lidar ratio [Klett, 1981; Fernald, 1984; Sasano et al., 1985]. However, the method is not applied in this work. Second, the Raman lidar method that is described in more detail in the following subsection.

3.1.2 Raman lidar method

For the independent determination of particle extinction and backscatter coefficients the Raman lidar method is applied [Ansmann et al., 1990]. Besides the elastic backscatter at λ the Raman signals from a reference gas (e.g. nitrogen) are measured at λ_R , resulting in the lidar equation for inelastic backscatter (Raman lidar equation):

$$P_{\lambda_R}(r) = P_{0,\lambda_0} \frac{\tau_P c A_T \eta_{\lambda_R}}{2} \frac{O_{\lambda_R}(r)}{r^2} \beta_{\lambda_R}(r) \exp \left\{ - \int_0^r [\alpha_{\lambda_0}(\xi) + \alpha_{\lambda_R}(\xi)] d\xi \right\} \quad (3.7)$$

Here, the backscatter is solely caused by molecules. The transmission term considers light extinction on the way to the scatterer at wavelength λ and on the way back to the instrument

at the Raman-shifted wavelength λ_R . The particle extinction coefficient can be directly calculated using the Raman signal from the reference gas P_{λ_R} :

$$\alpha_{\lambda_0}^p(r) = \frac{\frac{d}{dr} \ln \frac{N_R(r)}{r^2 P_{\lambda_R}(r)/O(r)} - \alpha_{\lambda_0}^m(r) - \alpha_{\lambda_R}^m(r)}{1 + \left(\frac{\lambda_0}{\lambda_R}\right)^{\mathring{A}_\alpha(r)}} \quad (3.8)$$

with the extinction-related Ångström exponent [*Ångström, 1964; Ansmann and Müller, 2005*]:

$$\mathring{A}_\alpha(r) = -\frac{\ln[\alpha_{\lambda_0}(r)/\alpha_{\lambda_R}(r)]}{\ln(\lambda_0/\lambda_R)} \quad (3.9)$$

and the molecule number density of the reference gas $N_R(r)$. $N_R(r)$ can be calculated using temperature and pressure informations [*Bucholtz, 1995*]. $\mathring{A}_\alpha(r)$ describes the wavelength dependence of the extinction coefficient. The backscatter coefficient can be determined from the ratio of the elastic and the Raman signals [*Ansmann et al., 1992*]:

$$\begin{aligned} \beta_{\lambda_0}^p(r) &= \left[\beta_{\lambda_0}^p(r_0) + \beta_{\lambda_0}^m(r_0) \right] \frac{P_{\lambda_0}(r) P_{\lambda_R}(r_0) N_R(r)}{P_{\lambda_R}(r) P_{\lambda_0}(r_0) N_R(r)} \\ &\times \frac{\exp \left[- \int_{r_0}^r \alpha_{\lambda_R}^p(\xi) + \alpha_{\lambda_R}^m(\xi) d\xi \right]}{\exp \left[- \int_{r_0}^r \alpha_{\lambda_0}^p(\xi) + \alpha_{\lambda_0}^m(\xi) d\xi \right]} - \beta_{\lambda_0}^m(r). \end{aligned} \quad (3.10)$$

Here, a reference value has to be estimated at height r_0 . This is usually done at heights where the particle backscatter is much smaller than the molecular backscatter [*Ansmann and Müller, 2005*].

3.1.3 Determination of water vapour mixing ratio

The Raman lidar technique enables the determination of water vapour mixing ratio profiles using the inelastic backscatter from nitrogen at 387 nm and from water vapour at 407 nm [*Whiteman, 2003; Wandinger, 2005*]. The mixing ratio of water vapour to dry air (from now on mixing ratio) is defined as

$$m_{\text{H}_2\text{O}}(r) = \frac{\rho_{\text{H}_2\text{O}}(r)}{\rho_{\text{air}}(r)} = f \frac{N_{\text{H}_2\text{O}}(r)}{N_{\text{N}_2}(r)} \frac{M_{\text{H}_2\text{O}}}{M_{\text{air}}} \quad (3.11)$$

with

$$f = \frac{\rho_{\text{N}_2}(r)}{\rho_{\text{air}}(r)}. \quad (3.12)$$

M and N are the molar masses and the molecular number densities of water vapour and dry air, respectively. Here, nitrogen is used as reference gas. The Raman backscatter coefficient

$$\beta_{\lambda_R}(r) = N_R(r) \frac{d\sigma_{\lambda_R}(\pi)}{d\Omega} \quad (3.13)$$

is given by the molecule number density $N_{\text{N}_2}(r)$ of the Raman-active gas and the differential cross section for the backward direction $d\sigma_{\lambda_R}(\pi)/d\Omega$. Rearranging and inserting Eqs. (3.7 and 3.13) in Eq. (3.11) results in:

$$m_{\text{H}_2\text{O}}(r) = C_{\text{H}_2\text{O}} \frac{P_{\text{H}_2\text{O}}(r)}{P_{\text{N}_2}(r)} \frac{\exp \left[- \int_0^r \alpha_{\lambda_{\text{N}_2}}(\xi) d(\xi) \right]}{\exp \left[- \int_0^r \alpha_{\lambda_{\text{H}_2\text{O}}}(\xi) d(\xi) \right]} \quad (3.14)$$

wherein the calibration factor

$$C_{\text{H}_2\text{O}} = f \frac{M_{\text{H}_2\text{O}}}{M_{\text{air}}} \frac{E_{\lambda_{\text{N}_2}}}{E_{\lambda_{\text{H}_2\text{O}}}} \frac{\eta_{\lambda_{\text{N}_2}}(r)}{\eta_{\lambda_{\text{H}_2\text{O}}}(r)} \frac{\left[\frac{d\sigma_{\lambda_{\text{N}_2}}(\pi)}{d\Omega} \right]}{\left[\frac{d\sigma_{\lambda_{\text{H}_2\text{O}}}(\pi)}{d\Omega} \right]} \quad (3.15)$$

has to be determined experimentally. In Equation (3.14) identical overlap factors for both wavelengths are assumed. Differences in the range-independent Raman backscatter cross sections for both channels are adsorbed within the calibration factor $C_{\text{H}_2\text{O}}$ which is described in more detail in section 5. The second term in Eq. (3.14) indicates the signal ratio which is directly measured. The third term describes the difference between the atmospheric transmission at λ_{N_2} and $\lambda_{\text{H}_2\text{O}}$.

The molecular extinction coefficients $\alpha^{\text{m}}(r)$ are calculated by temperature profiles from the MWR and standard atmosphere pressure profiles [Bucholtz, 1995]. Their vertical profiles measured with Polly^{XT} are illustrated in Figure 3.1 (a). $\alpha^{\text{p}}(r)$ can be determined by the Raman method using the particle extinction coefficient at 355 nm and a certain Ångström-exponent, but they are strongly influenced by the overlap effect. In contrast, the particle backscatter coefficient from the Raman method is a ratio product from the elastic signal at 355 nm and the inelastic signal at 387 nm and is therefore not affected by the overlap [Ansmann et al., 1992]. Hence, the particle extinction coefficients are calculated from the particle backscatter coefficients multiplied by a certain height-independent lidar ratio of 50 sr [Müller et al., 2007] to receive more reliable values below 1 km. The particle extinction coefficients are strongly smoothed, therefore, there is no strong decrease in the lowermost layers (Fig. 3.1 b). For the calculation of the particle backscatter coefficient at the Raman wavelengths, a spectral dependence with a backscatter-related Ångström-exponent of 1 is assumed. The determined aerosol optical depth (AOD) at 355 nm amounts to 0.22 on 5 May 2013, 23:10 UTC.

The resulting differential transmission ratios are illustrated in Fig. 3.1 (c). They indicate the influence by the differences in the atmospheric transmission at both Raman wavelengths. With a longer path through the atmosphere the influence of the differential transmission increases. By completely neglecting the differences in the atmospheric transmission, the error is less than 2.9 % below 2 km where most of the water vapour is located. In 10 km the value is 6.8 % but in this altitude the amount of water vapour is rather low. Since it is quite an effort to retrieve aerosol extinction profiles operationally, we neglect the particle contribution to the transmission. The resulting error amounts to 1.3 % at 2 km (blue line). These values are in a good agreement with studies on a modelled atmosphere [Whiteman, 2003].

The temperature dependence of the water vapour Raman spectrum portion that is selected by the interference filter is not considered in this work. For the optical setup of both lidars used here, the effect is negligible in the lower troposphere according to Whiteman [2003].

The uncertainty of the mixing ratio profiles is composed by three terms:

$$\Delta m_{\text{H}_2\text{O}} = \sqrt{\left(\frac{\partial m_{\text{H}_2\text{O}}}{\partial P_{\text{H}_2\text{O}}} \Delta P_{\text{H}_2\text{O}} \right)^2 + \left(\frac{\partial m_{\text{H}_2\text{O}}}{\partial P_{\text{N}_2}} \Delta P_{\text{N}_2} \right)^2 + \left(\frac{\partial m_{\text{H}_2\text{O}}}{\partial C_{\text{H}_2\text{O}}} \Delta C_{\text{H}_2\text{O}} \right)^2} \quad (3.16)$$

The first two describe the statistical error of the lidar signals called Poisson noise. The third one represents the uncertainty of the calibration factor which is assumed to be 6 %.

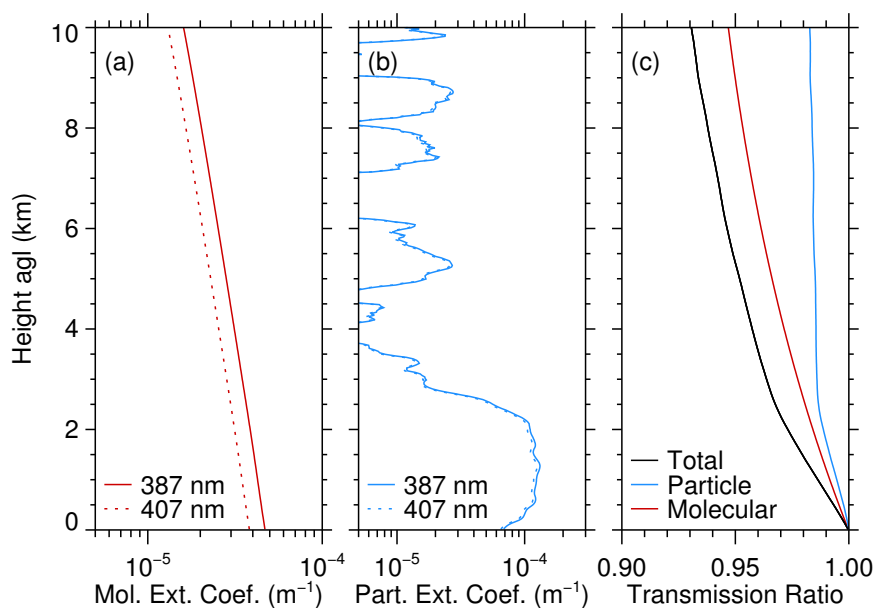


Figure 3.1: (a) Calculated profiles of the molecular extinction coefficient at 387 and 407 nm. (b) Determined particle extinction coefficient at 387 and 407 nm from a Polly^{XT} measurement on 5 May 2013, 23:10 UTC. (c) Resulting transmission ratio considering the molecular (red), the particle (blue) contribution and the the sum of both (black).

3.2 Microwave radiometry

In contrast to the lidar methodology, microwave radiometry is based on passive radiation observations. It makes use of the thermal emission of atmospheric constituents as water vapour, oxygen and liquid water in the microwave frequency range (3-300 GHz). The principles of radiative transfer, thermal emission [Bohren and Clothiaux, 2006] and their application to microwave radiometric remote sensing with passive instruments are outlined in Ulaby *et al.* [1981] and Janssen [1993]. The following section explains the fundamentals of microwave radiometry and the derivation of brightness temperatures which can be measured by a microwave radiometer (Sec. 2.3).

The *Planck*-function B_ν describes the thermal emission of a blackbody (emissivity $\epsilon = 1$) with temperature T at a frequency ν :

$$I_\nu = B_\nu(T) = \frac{2 h \nu^3}{c^2 [\exp(h \nu / k_B T) - 1]} \quad (3.17)$$

in a non-scattering medium for frequencies below 100 GHz [Janssen, 1993]. c denotes the speed of light, h Planck's constant and k_B Boltzmann's constant. Since particles or cloud droplets are small in contrast to the wavelength, scattering can be neglected in the microwave region, except for rain drops. For typical atmospheric temperatures and frequencies in the microwave region the *Rayleigh-Jeans* approximation $h \nu / k_B T \ll 1$ can be applied. Using this assumption Eq. (3.17) is simplified to

$$B_\nu(T) \approx \frac{2 k_B T \nu^2}{c^2}. \quad (3.18)$$

After rearranging Eq (3.18) the relation between the physical temperature and the blackbody radiance is expressed as

$$T_B(\nu) \approx \frac{c^2}{2 k_B \nu^2} I_\nu. \quad (3.19)$$

With this definition, the solution of the radiative transfer equation for a ground-base microwave radiometer in a non-scattering plane-parallel atmosphere is given by ([Janssen, 1993])

$$T_B(\nu) = T_{B_{\text{cos}}}(\nu) \exp(-\tau_\nu) + \int_0^\infty \alpha_\nu^a(r) T(r) \exp[-\tau_\nu(r)] dr. \quad (3.20)$$

This equation consists of two terms. The first one accounts for the cosmic background with $T_{B_{\text{cos}}} = 2.7$ K. The second one describes the emission of atmospheric gases and hydrometeors at temperature $T(r)$ attenuated by absorption through the atmosphere determined by the absorption coefficient $\alpha_\nu^a(r)$ and the optical depth between emission level and receiver

$$\tau_\nu(r) = \int_0^r \alpha_\nu^a(\xi) d\xi. \quad (3.21)$$

Figure 3.2 presents a modelled absorption spectrum in a cloudy atmosphere (liquid water path LWP = 0.2 kg m^{-2}) for frequencies below 100 GHz. The total extinction in this frequency range is characterised by two peaks that are caused by transitions from different rotational states of the gas molecules. The first peak is at the 22.235 GHz water vapour

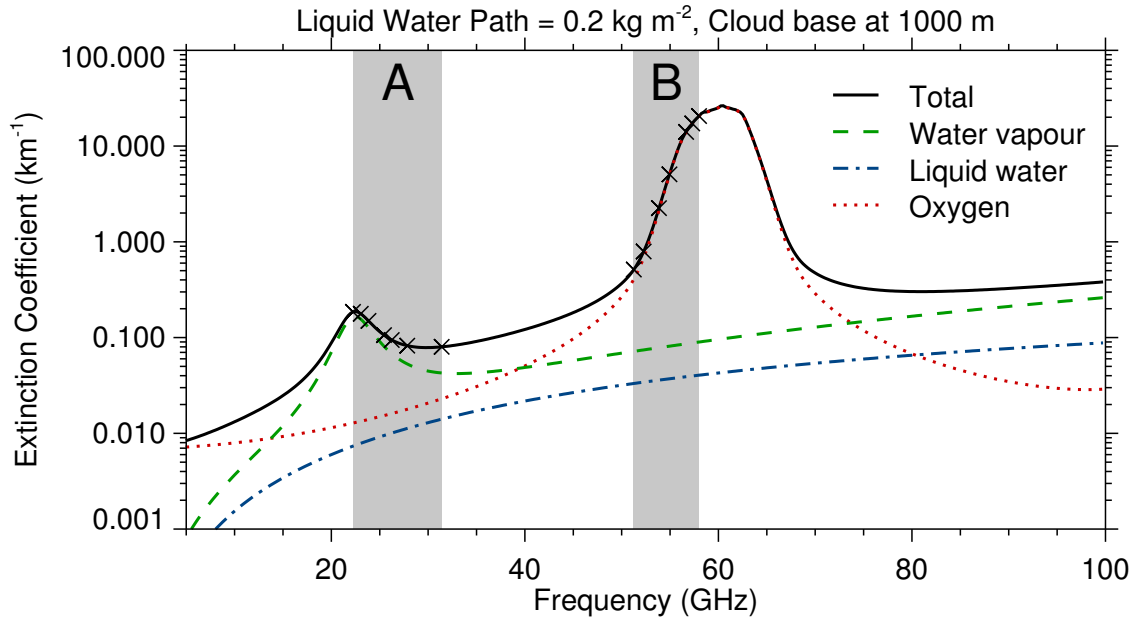


Figure 3.2: Modelled atmospheric extinction in the microwave spectrum for a cloudy atmosphere. The red, green and blue line shows show the contributions of oxygen, water vapour and cloud liquid with a liquid water path (LWP) of 0.2 kg m^{-2} and a cloud base at 1000 m. The black line represents the sum of all components. HATPRO measurements are performed at seven frequencies (crosses) in the frequency bands A and B, respectively. The figure is adapted from Pospichal [2009].

line. The second one is at the oxygen absorption complex around 60 GHz which consists of more than 30 absorption lines. Due to Doppler broadening and pressure broadening the absorption lines are smeared. For that reason, lower atmospheric layers are characterised by a wide oxygen absorption complex. In addition to the line absorption, the continuum absorption of water vapour affects the absorption spectrum. Liquid water shows a quadratic increase of absorption with frequency (dotted dashed blue line in Fig. 3.2).

4 Retrieval methodology

The focus of this work is to retrieve a continuous time series of water vapour profiles from a combination of ground-based remote sensing with Raman lidar and MWR in a straightforward way to offer a broad application. The retrieval is a two-step algorithm combining the Raman lidar mixing ratio profile with the MWR brightness temperatures. The Kalman filter (first step) eliminates measurement disruptions (e.g. clouds) to provide a full height mixing ratio profile that serves as input to the one-dimensional variational assimilation (optimal estimation method). Both steps, the Kalman filter and the one-dimensional variational (1D-VAR) assimilation, are explained in this chapter. The quantities as measurement resolution or uncertainty assumptions occurring herein, are referred to the main application at the LACROS station during HOPE that is intensively treated in Chapter 6.

The program code is written in the *interactive data language (idl)*. However, the water vapour retrieval is created to operate in a runtime engine that allows to work without a licence. It enables a straightforward and cost-efficient application of the retrieval and simplifies its distribution.

Figure 4.1 gives a brief overview of the retrieval framework. It starts with the latest analysed state $\hat{\mathbf{x}}_{k-1}$ which is projected in time to the estimated state \mathbf{x}_k^E with k being the time index. This state is then combined with the current lidar measurement \mathbf{y}_k to the filtered state \mathbf{x}_k^F using the Kalman filter. \mathbf{x}_k^F is then used as the a priori input to the one-dimensional variational assimilation. The a priori profile is modified such that the modelled brightness temperature match those measured with the microwave radiometer (MWR) \mathbf{z}_k resulting in the most probable estimated state $\hat{\mathbf{x}}_k$ which is again projected in time in the consecutive step. Inverse methods for atmospheric sounding are well described in *Rodgers [2000]*. For clarity the same notation is used.

4.1 Definition of quantities

In this section the state vector and the two measurement vectors are described. The first measurement vector contains the mixing ratio profile from the lidar measurement. It is used in the first retrieval step (Kalman filter). The second measurement vector consists of the brightness temperatures from the MWR measurement and a surface mixing ratio from a standard meteorological station. This vector is used in the optimal estimation.

The atmospheric state is described by the state vector

$$\mathbf{x} = [q_1, \dots, q_n]^T \quad (4.1)$$

which contains the humidity variable q at different height levels from 0 to height n (e.g. 10 km). The vertical resolution originates from the lidar measurements and accounts to 90 m. The humidity q variable is given as the natural logarithm of water vapour mixing ratio. The benefit is the limited range of variation and the prevention of negative unphysical values [*Phalippou*,

1996].

The lidar measurement vector of length m_y

$$\mathbf{y} = [q_1, \dots, q_{m_y}]^T \quad (4.2)$$

contains the water vapour mixing ratio at each height level from ground up to a possible cloud base. The lidar profiles \mathbf{y} and the associated errors ϵ_y are usually given in mixing ratio. For the reasons mentioned above, both have to be transformed into q values. The transformed errors define the diagonal elements of the lidar measurement covariance matrix \mathbf{S}_y . The off-diagonal elements are assumed to be zero which means that no correlation exists between the errors at certain height levels.

The second measurement vector, from now on observation vector, is given as:

$$\mathbf{z} = [T_{B,1}, \dots, T_{B,m_\nu}, q_s]^T \quad (4.3)$$

with the dimension m_z . It contains the brightness temperature \mathbf{T}_B at a certain frequency ν and the surface mixing ratio q_s from a standard meteorological station. In this study only zenith observations and frequencies along the water vapour absorption band are chosen. The combined measurement and forward model covariance matrix \mathbf{S}_z contains the errors from the MWR observation, from the surface mixing ratio measurement and from the forward model. The errors from the MWR observation are the radiometric noise. Its variance is set to 0.25 K^2 at each frequency. The off-diagonal elements are set to 0.01 K^2 meaning small covariances between the frequencies. The determination of the forward model error described in Sec. 4.3. Forward model uncertainties that occur due to assumptions in the **LWC** profiles are illustrated in Sec. 4.4. The measurement uncertainty of the surface mixing ratio amounts to 0.1 g kg^{-1} . However, the uncertainty is increased due to the distance between the observation platform and the surface humidity sensor (see Sec. 2.1) and is assumed to be 0.3 g kg^{-1} .

First guess profiles and errors are created for each campaign. Usually they are formed

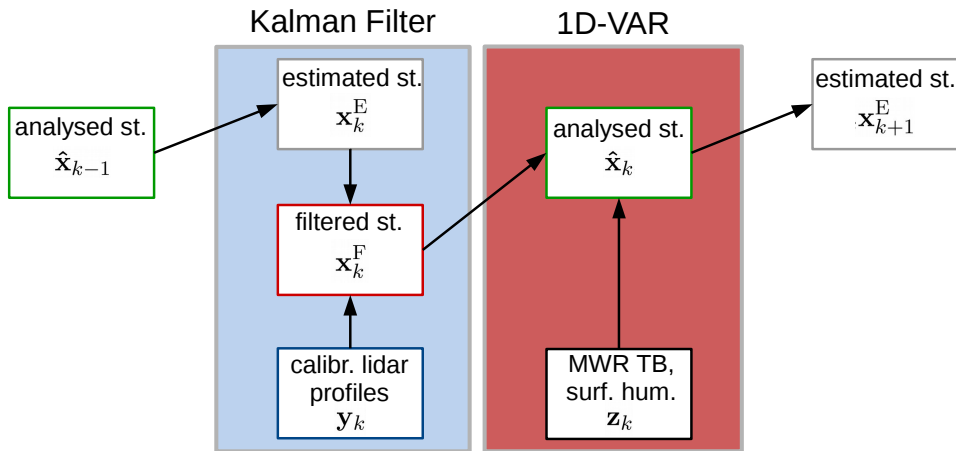


Figure 4.1: Sketch of the retrieval scheme. Details are given in the text. This figure is adapted from *Schneebeli* [2009].

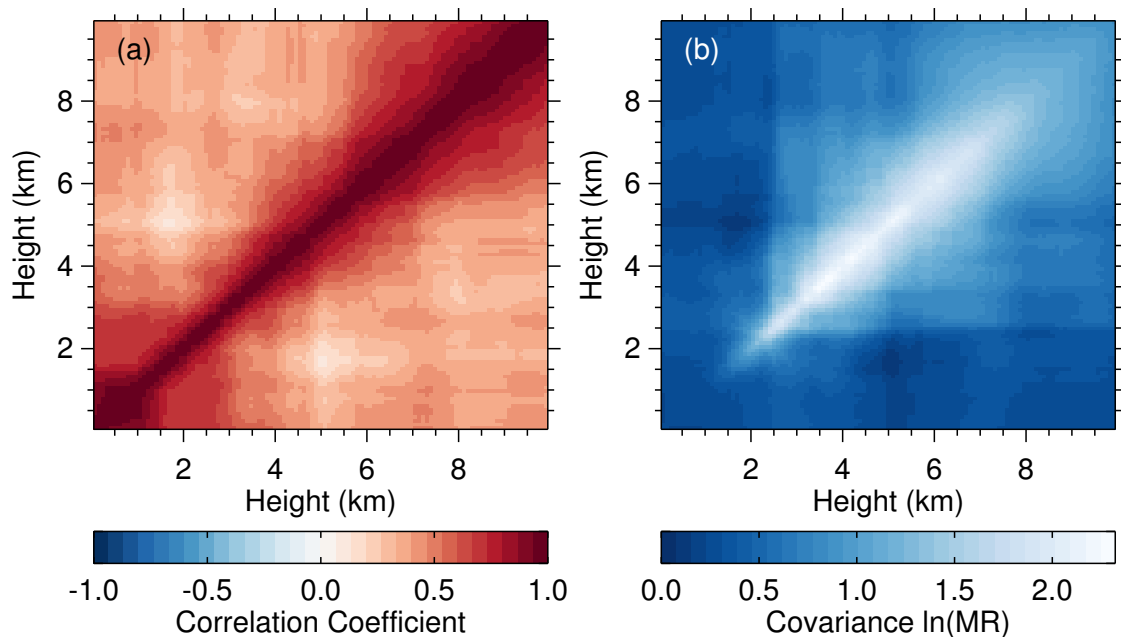


Figure 4.2: Correlation (a) and covariance matrix (b) derived from 211 radiosondes for HOPE. Both matrices are shown for the natural logarithm of the mixing ratio ($\ln(\text{MR})$) as function of height with a resolution of 90 m.

by a certain amount of RS. For the HOPE campaign 211 RS were used to calculate a mean profile that serves as first guess profile and is used after a long measurement disruption. Additionally, the correlation and covariance matrices are determined (Fig. 4.2). Here, the humidity variable is interpolated to the state grid space (lidar height grid) and is transformed to the natural logarithm before calculating the matrices. Both clearly illustrate the correlations between water vapour at different heights in the atmosphere. Naturally the correlation is close to one near the main diagonal and is smaller for off-diagonal terms. Due to well-mixed conditions the correlation in the lowest 1.5 km is higher. These matrices are similar to those from previous studies [Ebell *et al.*, 2013; Barrera-Verdejo *et al.*, 2016]. For RAO the RS data set is much larger with a total number of about 10 000. For that reason, the first guess covariance matrix is sometimes called RS climatology covariance in this work.

4.2 Kalman filter

In the presence of clouds, the lidar profile is truncated at the cloud base due the strong attenuation of the light pulses within the cloud. In this work the Kalman filter is used to expand the truncated lidar profile to the full height range using previous informations. The Kalman filter is based on the following two equations:

$$\mathbf{y}_k = \mathbf{H}_k \mathbf{x}_k + \epsilon_{y,k} \quad (4.4)$$

$$\mathbf{x}_{k+1} = \mathbf{M}_k \mathbf{x}_k + \epsilon_{t,k}. \quad (4.5)$$

The evolution operator (e.g. forward model) \mathbf{H}_k projects the state into measurement space (Eq. 4.4). Since \mathbf{x}_k and \mathbf{y}_k use the same humidity variable, the forward model matrix \mathbf{H}_k equals the unity matrix with dimension $m_y \times n$. Equation (4.5) describes the transition of

the state vector at time step k to time step $k + 1$. The transition matrix \mathbf{M}_k is assumed to be the unity matrix due to the lack of an atmospheric model. The transition error $\epsilon_{t,k}$ has the covariance matrix $\mathbf{S}_{t,k}$. For the calculation of $\mathbf{S}_{t,k}$ the Schneebeli method can be applied [Schneebeli, 2009]. He generated a time series of synthetic profiles from a combination of consecutive radiosondes and ground values. $\mathbf{S}_{t,k}$ is finally calculated from an ensemble of these consecutive profiles. A similar approach is described by Han *et al.* [1997]. After a large number of time steps, it might happen that the correlations between layers get lost. Another possibility is to start with RS climatology covariance as previous covariance matrix ($\hat{\mathbf{S}}_{k-1}$) at every consecutive time step. Using this approach the addition of the transition covariance matrix ($\mathbf{S}_{t,k}$) can be skipped. The error settings that are used for each application are specified in the according chapters 6 and 7.

Using Eq. (4.5) the last analysed state $\hat{\mathbf{x}}_{k-1}$ and its covariance matrix $\hat{\mathbf{S}}_{k-1}$ are propagated as follows:

$$\mathbf{x}_k^E = \mathbf{M}_k \hat{\mathbf{x}}_{k-1} \quad (4.6)$$

$$\mathbf{S}_k^E = \mathbf{M}_k \hat{\mathbf{S}}_{k-1} \mathbf{M}_k^T + \mathbf{S}_{t,k}. \quad (4.7)$$

\mathbf{x}_k^E and \mathbf{S}_k^E are the estimated state its covariance matrix, respectively. These are then combined with the lidar measurement at time step k to the filtered state:

$$\mathbf{x}_k^F = \mathbf{x}_k^E + \mathbf{G}_k^K [\mathbf{y}_k - \mathbf{H}_k \mathbf{x}_k^E] \quad (4.8)$$

with \mathbf{G}_k^K being the Kalman gain matrix, or contribution function matrix:

$$\mathbf{G}_k^K = \mathbf{S}_k^E \mathbf{H}_k^T [\mathbf{H}_k \mathbf{S}_k^E \mathbf{H}_k^T + \mathbf{S}_{y,k}]^{-1}. \quad (4.9)$$

The covariance matrix of the filtered state is determined by:

$$\mathbf{S}_k^F = \mathbf{S}_k^E - \mathbf{G}_k^K \mathbf{H}_k \mathbf{S}_k^E. \quad (4.10)$$

After a large measurement disruption the transition error is enhanced by multiplying the number of missing time steps since the last profile to account for the larger uncertainty of the last analysed state. The last profile and covariance matrix is replaced by the radiosonde climatology and its covariance matrix if the disruption lasts longer than 24 h. \mathbf{x}_k^F and \mathbf{S}_k^F serves as input to the optimal estimation.

The application of this technique for linear filtering and prediction problems was first described by [Kalman, 1960; Kalman and Bucy, 1961].

4.3 Forward model

In the optimal estimation microwave brightness temperatures (\mathbf{T}_B) at given frequencies (ν) and elevation angles (Θ) are modelled from the a priori atmospheric profiles (Fig. 4.3) and are compared to those that are measured. However, in this work only zenith observations are used. Based on Simmer [1994], $\mathbf{F}(\mathbf{x})$ models the non-scattering microwave radiative transfer using gas absorption by Rosenkranz and liquid water absorption by Liebe [Rosenkranz, 1998; Liebe *et al.*, 1993] for each height level of the retrieval grid (90 m). The Rosenkranz gas absorption model is corrected for the water vapour continuum absorption according to Turner *et al.* [2009]. The humidity information (\mathbf{q}) of the a priori profile originates from

the Kalman filtered state, whereas the temperature profiles (\mathbf{T}) are provided by statistical retrievals from MWR observations (Sec. 2.3). The pressure profiles (\mathbf{p}) are calculated by surface pressure observations from MWR and the barometric formula. Another influence is the already introduced cosmic background \mathbf{T}_{Bcos} (Sec. 3.2). Since the retrieval grid is limited to 10 km, the thermodynamic state between 10 and 30 km is taken from a RS climatology above Essen which is in the vicinity of the HOPE area. The restriction to the troposphere up to 10 km would lead to errors of around 1 K in the calculation of the brightness temperatures. Assumptions about the liquid water content (\mathbf{LWC}) and its determination are described in Sec. 4.4. The forward modelling of the surface mixing ratio is trivial. It is a 1 : 1 translation to the lowest level of the state vector \mathbf{x} . In conclusion $\mathbf{F}(\mathbf{x})$ is of the following form:

$$\mathbf{F}(\mathbf{x}) = \begin{pmatrix} \text{RTO}(\mathbf{T}, \mathbf{q}, \mathbf{p}, \mathbf{LWC}, \nu_1) \\ \vdots \\ \text{RTO}(\mathbf{T}, \mathbf{q}, \mathbf{p}, \mathbf{LWC}, \nu_{m\nu}) \\ q_1 \end{pmatrix} \quad (4.11)$$

with RTO being the radiative transfer operator.

The forward model error is calculated as covariance of the difference between brightness temperatures modelled by two different absorption codes, Rosenkranz and Liebe [*Rosenkranz, 1998; Liebe et al., 1991*] applied to a longterm data set of radiosondes from Lindenberg, Germany. The diagonal elements of its covariance matrix are shown in Tab. 4.1. One has to consider that there are significant off-diagonal terms. This error is part of the combined observation and forward model covariance \mathbf{S}_z . The uncertainties of the gas absorption models cause biased mixing ratio profiles (see Chapter 6.2).

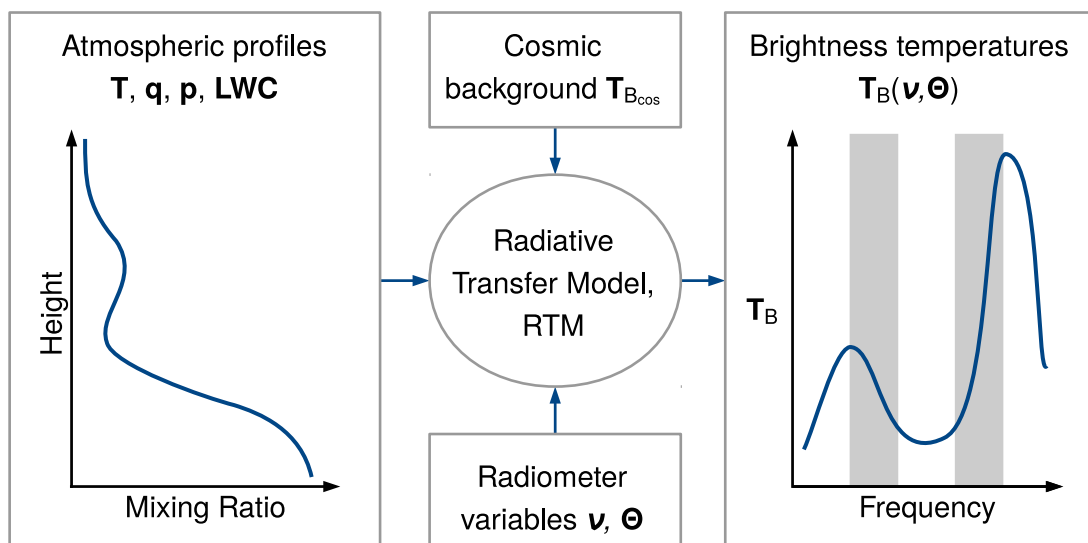


Figure 4.3: Illustration of the radiative transfer model. Details are given in the text.

Table 4.1: Forward model error for each frequency due to different absorption codes. Uncertainties are given as square root of the diagonal elements of the covariance matrix.

Frequency (GHz)	HATPRO	TP/WVP-3000
	Uncertainty (K)	Uncertainty (K)
22.24	0.07	0.07
23.04	0.2	0.2
23.84	0.42	0.42
25.44	0.56	—
26.24	0.55	0.55
27.84	0.53	—
30.00	—	0.51
31.40	0.51	—

4.4 Liquid water assumption

Since liquid water strongly affects the absorption in the microwave spectrum, its amount and height have to be known. However, from MWR only the integral value can be derived, and not its vertical distribution. For that reason the **LWC** profiles are determined as described in this section. The cloud base of a liquid water cloud is identified by the gradient method based on the 1064 nm channel from lidar [Baars *et al.*, 2008]. In this work, it has been shown that this method is more robust for the automatic detection of the cloud base than the wavelet covariance transform [Brooks, 2003; Baars *et al.*, 2008]. However, a threshold value has to be chosen carefully to distinguish between thin liquid water clouds and optically thick aerosol layers below liquid water clouds. Additionally, liquid water clouds are only detected if the LWP is larger than a narrow threshold of 5 g m^{-2} .

The **LWC** is calculated from the modified adiabatic assumption [Karstens *et al.*, 1994]:

$$\mathbf{LWC} = \mathbf{LWC}_{\text{ad}} [1.239 - 0.145 \ln(h)], \quad (4.12)$$

where h indicates the height above cloud base in m and h within the range of 1 and 5140 m. The adiabatic \mathbf{LWC}_{ad} is calculated using the temperature and pressure profiles explained in Sec. 4.3 and is corrected for effects of dry air entrainment, freezing drops or precipitation. The **LWC** is integrated over all layers until the calculated LWP equals the LWP measured with MWR. This height is finally defined as cloud top. However, any profile is treated as single layer cloud with this method.

Usual approaches to diagnose **LWC** profiles from radiosonde are based on a threshold method [Wang *et al.*, 1999]. Cloud bases or tops are identified when the relative humidity exceeds or falls below 95 %, respectively. Within the cloud the **LWC** is calculated using the modified adiabatic assumption [Löhnert and Crewell, 2003]. The uncertainty that results in the assumption of single layer clouds is estimated by comparing both mentioned methods. This is done for a long term data set of radiosondes from Lindenberg, Germany. For these radiosonde profiles brightness temperatures are modelled at the HATPRO frequencies using both **LWC** profile assumptions. The brightness temperature difference as function of LWP is illustrated in Fig. 4.4 (a). As can be seen, the means and standard deviations (coloured lines and error bars) increases with increasing LWP. In addition, the difference

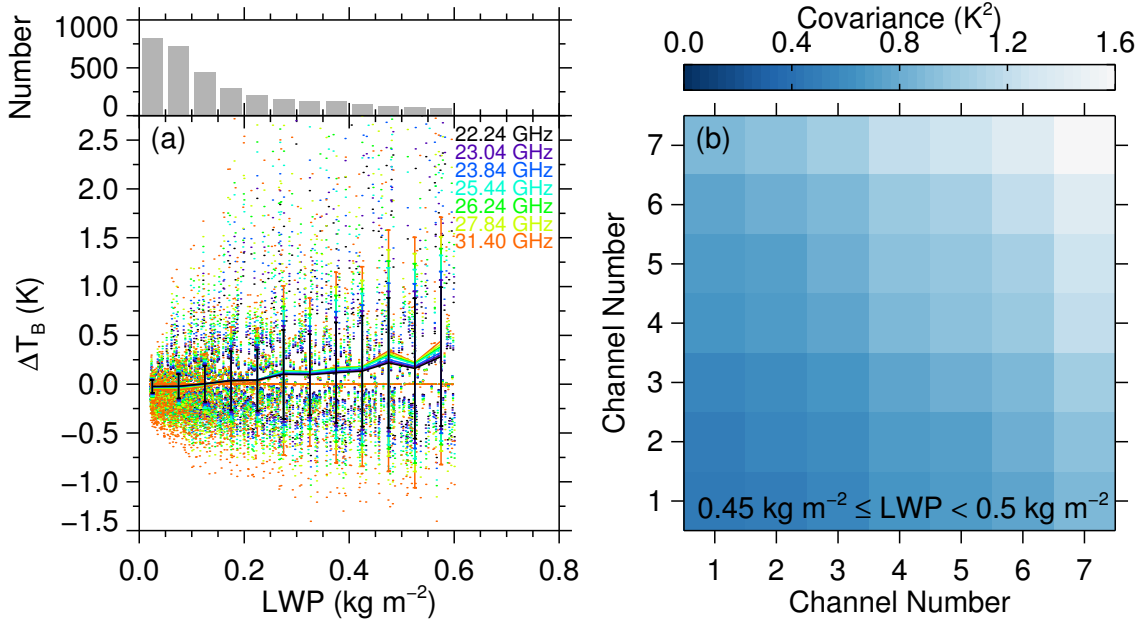


Figure 4.4: **(a)** Brightness temperature difference as function of LWP (dots) using two different **LWC** assumptions. The colours indicate the according frequencies (top right). The means and the standard deviations per bin size are indicated by coloured lines and error bars, respectively. The bin size amounts to 0.05 kg m^{-2} . The number of occurrences is given in grey bars at the top. **(b)** Exemplary covariance matrix for an LWP between 0.45 kg m^{-2} and 0.5 kg m^{-2} . The channel numbers correspond with the HATPRO frequencies given in **(a)** that means 1 refers to 22.24 etc.

increases from the 22.24 to 31.4 GHz. Naturally, there is no difference for single layer clouds indicated by the dots at 0 K. The number of occurrences decreases with increasing LWP (grey bars on the top). However, only clouds with an LWP larger than 0.02 kg m^{-2} are considered. Figure 4.4 (b) shows an exemplary covariance matrix for an LWP between 0.45 kg m^{-2} and 0.5 kg m^{-2} . These uncertainties contain significant off-diagonal terms and are larger for the channels that are more sensitive to liquid water (31.4 GHz). According to the observed LWP the corresponding covariance is added to the combined observation and forward model covariance matrix \mathbf{S}_z to account for the assumption of single layer liquid water clouds.

The according uncertainties at the TP/WVP-3000 frequencies are illustrated in the appendix (A.1).

4.5 Optimal estimation method (OEM)

A schematic overview over the optimal estimation is given in Fig. 4.5. In basic terms, for a given MWR observation and a forward model that simulates from a previous analysed profile what the MWR would observe given an arbitrary state. The problem is that several different states may produce the same measurement. This is a so-called ill-posed problem. To constrain the state space a priori informations as lidar profiles are needed. In the proposed retrieval the lidar profiles are Kalman filtered as mentioned above. Finally, the optimal estimation finds the most probable solution (mixing ratio profile) from a class of solutions.

The theory of inverse modelling based on optimal estimation methods is briefly introduced in this section.

The optimal estimation of an atmospheric state by a given observation vector \mathbf{z} and an a priori state $\mathbf{x}_a = \mathbf{x}^F$ can be found by minimising the cost function of the form [Rodgers, 2000]

$$J(\hat{\mathbf{x}}) = J_a(\hat{\mathbf{x}}) + J_z(\hat{\mathbf{x}}) + J_{\text{sup}}(\hat{\mathbf{x}}) \quad (4.13)$$

$J_a(\hat{\mathbf{x}})$ indicate the a priori costs, $J_z(\hat{\mathbf{x}})$ the observation costs and $J_{\text{sup}}(\hat{\mathbf{x}})$ is a penalty term to avoid supersaturation. Since both liquid and ice phase can occur in clouds at temperatures between -38 to -5 °C [Heymsfield and Sabin, 1989; Koop et al., 2000; Ansmann et al., 2009; Kanitz et al., 2011], the saturation mixing ratio is defined as follows:

$$q^{\text{sat}} = \begin{cases} q_{\text{liq}}^{\text{sat}} & : -5^\circ\text{C} < \vartheta \\ q_{\text{lin}}^{\text{sat}} & : -38^\circ\text{C} < \vartheta < -5^\circ\text{C} \\ q_{\text{ice}}^{\text{sat}} & : \vartheta < -38^\circ\text{C} \end{cases} \quad (4.14)$$

where $q_{\text{liq}}^{\text{sat}}$ and $q_{\text{ice}}^{\text{sat}}$ are the saturation mixing ratios above liquid water and ice, respectively. $q_{\text{lin}}^{\text{sat}}$ denotes a linear function that describes the transition from $q_{\text{liq}}^{\text{sat}}$ to $q_{\text{ice}}^{\text{sat}}$. The according uncertainty is defined as the difference between $q_{\text{liq}}^{\text{sat}}$ and $q_{\text{lin}}^{\text{sat}}$ and between $q_{\text{lin}}^{\text{sat}}$ and $q_{\text{ice}}^{\text{sat}}$, respectively. It amounts to a maximum of 0.23 g kg^{-1} at -8 °C and decreases with decreasing temperature that means increasing height.

$J_{\text{sup}}(\hat{\mathbf{x}})$ adds a penalty if the retrieval produces supersaturation all over the profile [Phalippou, 1996; Schneebeli, 2009]. This function is defined by

$$J_{\text{sup}}(\hat{\mathbf{x}}) = \sum_j^n \mathbf{J}_{\text{sup}}(x_j) \quad (4.15)$$

$$\mathbf{J}_{\text{sup}}(x_j) = \begin{cases} 0 & : q_j \leq q_j^{\text{sat}} \\ \zeta (q_j - q_j^{\text{sat}})^3 & : q_j > q_j^{\text{sat}}. \end{cases} \quad (4.16)$$

The constant $\zeta = 10^6$ drives the strictness of the constraint. The larger ζ , the more strict is the constraint. Here, a large value is set, to avoid supersaturation all over the profile. However supersaturation is not completely avoided due to the uncertainties in the temperature profiles from the MWR that are the basis of the saturation mixing ratio q^{sat} .

The implementation of a constraint that prohibits subsaturation within clouds is not beneficial in this application. The assumption of single layer liquid water clouds and the uncertainties in the temperature profile would result in uncertain saturation mixing ratio profiles and finally lead to wrong retrievals.

Written out Eq. (4.13) becomes to:

$$J(\hat{\mathbf{x}}) = [\hat{\mathbf{x}} - \mathbf{x}_a]^T \mathbf{S}_a^{-1} [\hat{\mathbf{x}} - \mathbf{x}_a] + [\mathbf{z} - \mathbf{F}(\hat{\mathbf{x}})]^T \mathbf{S}_z^{-1} [\mathbf{z} - \mathbf{F}(\hat{\mathbf{x}})] + J_{\text{sup}}(\hat{\mathbf{x}}). \quad (4.17)$$

For clarity the time index is omitted here. $\hat{\mathbf{x}}$ is the optimal estimate of the atmospheric state. \mathbf{S}_a and \mathbf{S}_z denote the covariance matrices of the a priori and the observation, respectively.

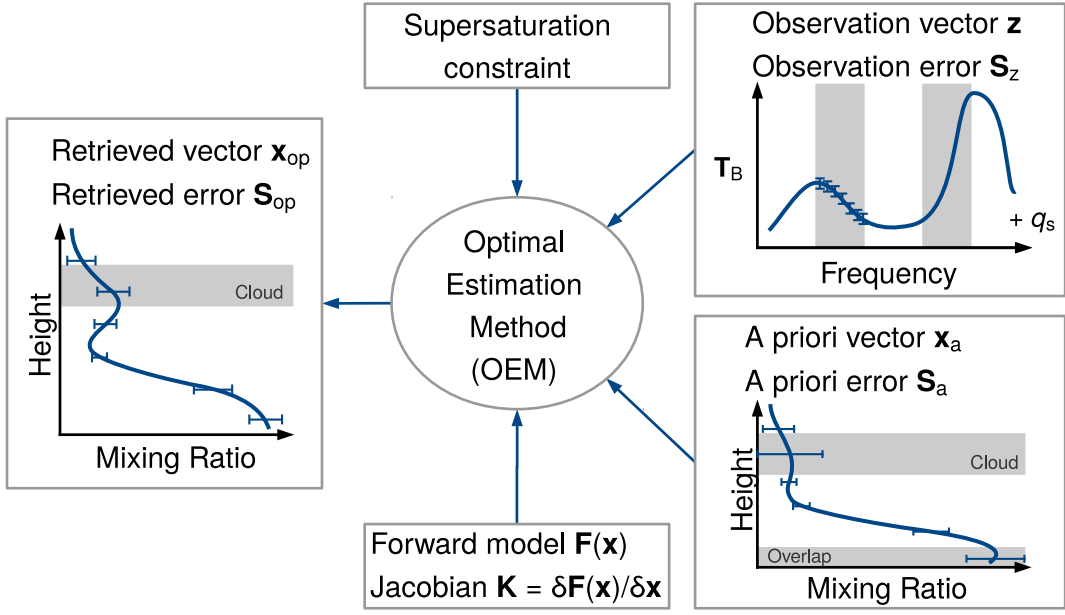


Figure 4.5: Illustration of the optimal estimation method. Details are given in the text.

The optimum solution can be found iteratively using the Levenberg-Marquardt method:

$$\begin{aligned} \mathbf{x}_{i+1} = & \mathbf{x}_i + \left[(1 + \gamma) \mathbf{S}_a^{-1} + \mathbf{K}_i^T \mathbf{S}_z^{-1} \mathbf{K}_i + \ddot{\mathbf{J}}_{\text{sup}} \right]^{-1} \\ & \times \left[\mathbf{K}_i^T \mathbf{S}_z^{-1} (\mathbf{z} - \mathbf{F}(\mathbf{x}_i)) + \mathbf{S}_a^{-1} (\mathbf{x}_i - \mathbf{x}_a) + \dot{\mathbf{J}}_{\text{sup}} \right] \end{aligned} \quad (4.18)$$

with i being the iteration index. The dots above \mathbf{J} indicate the first and the second derivative, respectively. The Levenberg-Marquardt parameter γ is increased by a factor of 10 if $J(\hat{\mathbf{x}}_{i+1}) \geq J(\hat{\mathbf{x}}_i)$ and reduced by a factor of 2 if $J(\hat{\mathbf{x}}_{i+1}) < J(\hat{\mathbf{x}}_i)$. In this work the initial value of $\gamma = 2$. It was found that the Levenberg-Marquardt method does not reach convergence faster but more reliably than the Gauss-Newton approach ($\gamma = 0$) [Rodgers, 2000; Schneebeli, 2009]. The Levenberg-Marquardt approach is illustrated in Fig. 4.6. If $\gamma \rightarrow \infty$, the step tends towards the steepest descent of the cost function, allowing to leave a local minimum towards a global minimum [Hewison and Gaffard, 2006]. \mathbf{K}_i denotes the weighting function matrix, also known as Jacobian or Kernel (hence \mathbf{K}), but from now on Jacobian. It is defined as:

$$\mathbf{K} = \frac{\partial \mathbf{F}(\hat{\mathbf{x}})}{\partial \hat{\mathbf{x}}} \quad (4.19)$$

and calculated by perturbing the state vector at each height level by $\ln(0.1 \text{ g kg}^{-1})$. Equation 4.18 is iterated until the following criterion is fulfilled:

$$[\mathbf{F}(\mathbf{x}_{i+1}) - \mathbf{F}(\mathbf{x}_i)] \mathbf{S}_{\delta z}^{-1} [\mathbf{F}(\mathbf{x}_{i+1}) - \mathbf{F}(\mathbf{x}_i)] \ll m, \quad (4.20)$$

with $\mathbf{S}_{\delta z}$ being the covariance matrix between the measurement and $\mathbf{F}(\hat{\mathbf{x}})$:

$$\mathbf{S}_{\delta z} = \mathbf{S}_z (\mathbf{K} \mathbf{S}_a \mathbf{K}^T + \mathbf{S}_z)^{-1} \mathbf{S}_z. \quad (4.21)$$

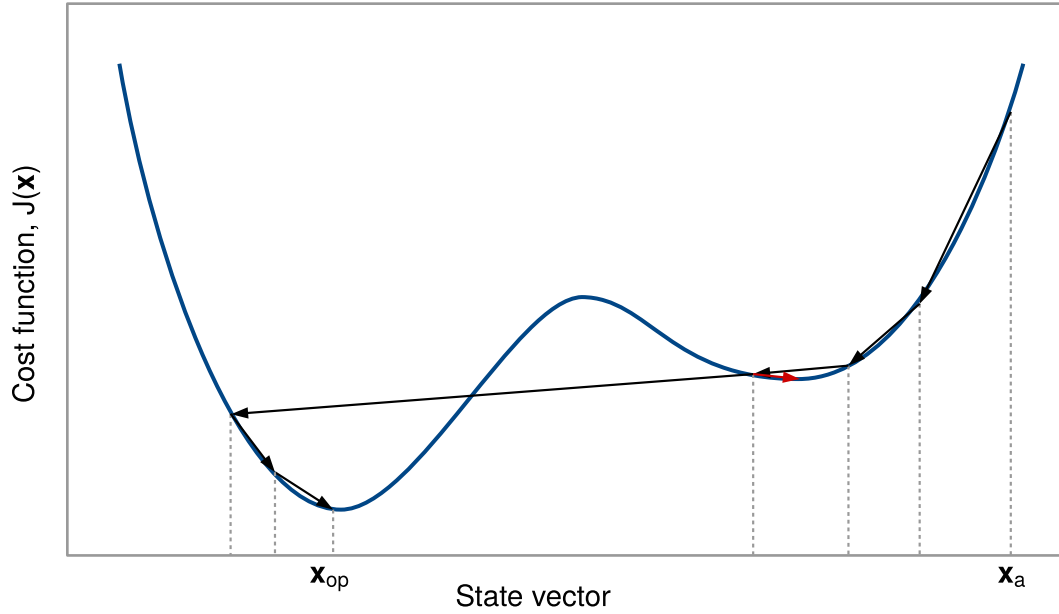


Figure 4.6: Schematic illustration of minimising the cost function using the Levenberg-Marquardt approach. Black arrows show the cost function at each iteration step from the a priori state \mathbf{x}_a to the optimal solution \mathbf{x}_{op} . The red arrow shows an iteration step that fails and finds a local minimum but not the optimal solution. This figure is adapted from [Hewison, 2006].

Finally, the covariance matrix of the resulting analysed state vector (a posteriori) is calculated as

$$\hat{\mathbf{S}} = (\mathbf{K}^T \mathbf{S}_z^{-1} \mathbf{K} + \mathbf{S}_a^{-1})^{-1}. \quad (4.22)$$

Since the retrieval might converge at a false minimum it is necessary to check the retrieval for correct convergence. Therefore, the χ^2 test for consistency of the optimal retrieval (\mathbf{x}_{op}) with the observation (\mathbf{z}_{obs}) is introduced:

$$\chi^2 = [\mathbf{F}(\mathbf{x}_{op}) - \mathbf{z}_{obs}]^T \mathbf{S}_{\delta_z}^{-1} [\mathbf{F}(\mathbf{x}_{op}) - \mathbf{z}_{obs}]. \quad (4.23)$$

Herein, the forward modelled state $\mathbf{F}(\mathbf{x}_{op})$ and the observation vector \mathbf{z}_{obs} are compared with the error covariance matrix \mathbf{S}_{δ_z} . The test is usually used to look for outliers, i.e. cases where the χ^2 value is larger than a threshold value (χ_{thr}). χ_{thr} is calculated for a probability of 5% that χ^2 is greater than the threshold for a theoretical χ^2 distribution with m_z degree of freedom. All retrieved profiles with a χ^2 value that exceeds the threshold are marked as untrustworthy. The χ^2 values of all retrieved profiles are analysed and discussed in Sec. 6.2.

The averaging kernel matrix \mathbf{A} gives the sensitivity of the retrieval to the true state:

$$\mathbf{A} = \frac{\partial \hat{\mathbf{x}}}{\partial \mathbf{x}} = (\mathbf{K}^T \mathbf{S}_z^{-1} \mathbf{K} + \mathbf{S}_a^{-1})^{-1} \mathbf{K}^T \mathbf{S}_z^{-1} \mathbf{K}. \quad (4.24)$$

The rows \mathbf{a}_i^T of \mathbf{A} are the averaging kernels. In an ideal inverse method, \mathbf{A} would be a unit matrix. Generally the averaging kernels are peaked functions which indicate the smearing of

information across multiple levels. In this work, the averaging kernels are no peaked functions, because the MWR observation does not provide enough vertical information. This issue is covered in detail in Sec. 6.1.1. The averaging kernel has an area which is a measure of fraction that comes from the observation, rather than the a priori. The area of \mathbf{a}_i is the sum of its elements and can be calculated as $\mathbf{A} \mathbf{u}$ where \mathbf{u} is a vector with unit elements.

The information content of a measurement can be expressed by the degree of freedom (d) which is the trace of \mathbf{A} . d is a measure of how many independent quantities are measured. One has to consider that the larger the a priori uncertainty, the larger d and the larger the retrieved a posteriori uncertainty [Ebell *et al.*, 2010].

In summary, the retrieval is strongly driven by the a priori uncertainty which constrains the subspace in which the retrieval must lie. The larger the off-diagonal elements of this covariance, that means the higher the correlations, the smaller is the subspace. For that reason the a priori covariance has to be estimated very carefully. In the proposed retrieval the a priori covariance is strongly decreased by the application of the Kalman filter that reduces the subspace of possible solutions.

In Chapter 6 the retrieval applied to the LACROS data from HOPE is evaluated based on RS launches. Afterwards, the retrieval application to other data sets is evaluated and is presented in Chapter 7.

5 Automatic Raman lidar calibration

For the application of the two-step algorithm for retrieving a continuous time series of water vapour profiles, the Raman lidar needs to be calibrated automatically. In this chapter, a method to derive water vapour profiles from Raman lidar measurements calibrated by the integrated water vapour (IWV) from a collocated microwave radiometer during the intense observation campaign HOPE is presented. The simultaneous observation of a microwave radiometer and a Raman lidar allowed an operational and continuous measurement of water vapour profiles. Based on the application of this approach, it is possible to retrieve water vapour profiles up to cloud base during all non-precipitating conditions.

Most of this chapter has already been described and presented in *Foth et al.* [2015].

5.1 Calibration methods

After considering the uncertainties explained in Sec. 3.1.3, the calibration factor:

$$C_{\text{H}_2\text{O}} = f \frac{M_{\text{H}_2\text{O}}}{M_{\text{air}}} \frac{E_{\lambda_{\text{N}_2}}}{E_{\lambda_{\text{H}_2\text{O}}}} \frac{\eta_{\lambda_{\text{N}_2}}(r)}{\eta_{\lambda_{\text{H}_2\text{O}}}(r)} \frac{\left[\frac{d\sigma_{\lambda_{\text{N}_2}}(\pi)}{d\Omega} \right]}{\left[\frac{d\sigma_{\lambda_{\text{H}_2\text{O}}}(\pi)}{d\Omega} \right]} \quad (5.1)$$

can be determined by comparison with simultaneous measurements from a reference instrument. In the following subsections three different methods with two instruments (MWR and RS) are presented in detail for a clear sky night from a Polly^{XT} measurement on 5 May 2013 (HOPE IOP 12). Afterwards, the stability of the IWV method during the two month period of HOPE is presented.

5.1.1 Regression method

The regression method can be used to calibrate the lidar profile with a RS [*England et al.*, 1992]. Therefore, a linear regression between the water vapour mixing ratio from the RS and the signal ratio $P_{\text{H}_2\text{O}}/P_{\text{N}_2}$ from the lidar is performed (see Fig. 5.1a). The calibration factor $C_{\text{H}_2\text{O}}$ is defined as the slope of the regression line. In our case, the calibration factor amounts to 12.32 g kg^{-1} . The standard error of the slope ($\sigma_{C_{\text{H}_2\text{O}}}$) is 0.17 g kg^{-1} and the correlation coefficient $R^2 = 0.98$ shows a good correlation between the lidar signal and the mixing ratio from the RS. This results in a relative error of 1.4%. The signal ratio is corrected for differential transmission and is averaged over 20 min from 23:00 to 23:20 UTC. The vertical smoothing amounts to 270 m. Only an altitude region from 2 up to 5 km is regarded for the regression to exclude boundary layer inhomogeneities in the water vapour structure and to avoid differences due to the RS drift in higher altitudes. Using this method, *Dionisi et al.* [2010] found a variability in the calibration factor of about 10%.

5.1.2 Profile method

Another method to calibrate the lidar with a RS is the profile method with an associated uncertainty of about 5% [*Mattis et al.*, 2002; *Reichardt et al.*, 2012]. $C_{\text{H}_2\text{O}}$ is calculated by

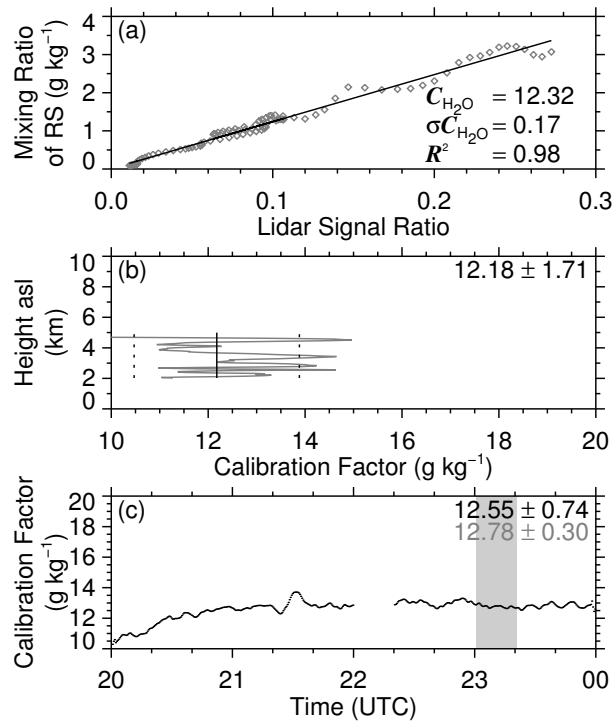


Figure 5.1: Calibration methods for a clear sky night from a Polly^{XT} measurement on 5 May 2013 (HOPE IOP 12): (a) regression method. Water vapour mixing ratio of the radiosonde (RS) as function of the signal ratio from the lidar averaged over 20 min from 23:00 to 23:20 UTC. $C_{\text{H}_2\text{O}}$ is the slope of the regression line, $\sigma_{C_{\text{H}_2\text{O}}}$ is the standard error of the slope and R^2 is the coefficient of determination. (b) Profile method. The calibration factor for each considered height bin. The numbers indicate the mean calibration factor and its standard deviation. (c) IWV method. Time series of the calculated calibration factor (black line). The black numbers denote the mean and the standard deviation of the whole time range, whereas the grey numbers correspond to the time range of the RS ascent (grey area).

the temporal mean of the water vapour mixing ratio measured with RS and the signal ratio from the lidar for each considered height bin. This ratio varies with altitude resulting in a mean calibration factor of 12.18 g kg^{-1} and a standard deviation of 1.71 g kg^{-1} (Fig. 5.1b). The relative error amounts to 14%. Here, the same time range, altitude region and vertical smoothing as for the regression method are applied.

5.1.3 IWV method

In previous experiments [Ferrare et al., 1995; Herold et al., 2011], radiosondes showed a significant sonde-to-sonde variability [Nash et al., 2005] as well as a dry bias [Turner et al., 2003]. For that reason, water vapour Raman lidars were often calibrated based on the IWV or integrated precipitable water retrieved from a MWR resulting in a relative uncertainty of 5% [Turner and Goldsmith, 1999], 7% [Madonna et al., 2011] and 3% [Adam et al., 2010], respectively.

Before using the MWR for the calibration of the lidar it is necessary to estimate the error of

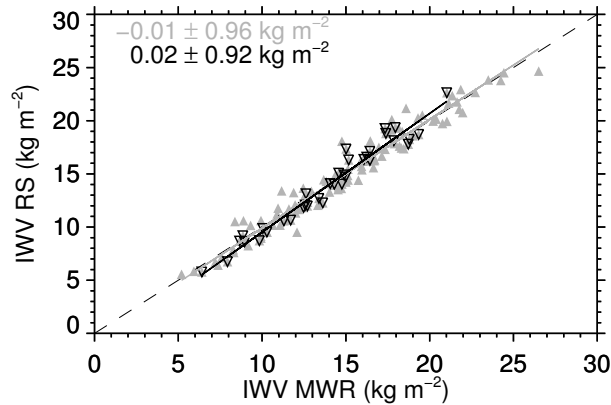


Figure 5.2: Comparison between IWV from MWR and RS. Grey and black triangles indicate all weather conditions and only clear sky conditions, respectively. The solid lines notify the according regression lines. The numbers in the upper left corners denote the bias and the standard deviation, respectively.

the IWV. Figure 5.2 displays the IWV comparison between MWR and RS. On average the bias during all weather conditions and clear sky is very low with values of -0.01 ± 0.96 and $0.02 \pm 0.92 \text{ kg m}^{-2}$ (mean \pm SD), respectively. However, during drier ($\text{IWV} < 7 \text{ kg m}^{-2}$) or more humid ($\text{IWV} > 20 \text{ kg m}^{-2}$) clear sky conditions the relative difference can amount up to 10%. These relative differences have to be considered when calibrating lidar profiles.

Using the IWV method, $C_{\text{H}_2\text{O}}$ is defined as the ratio of the IWV measured with the MWR and the integrated signal ratio from the lidar. For simultaneous measurements from MWR and lidar, $C_{\text{H}_2\text{O}}$ can be calculated from the mean of its time series during clear sky. To determine clear sky periods, two criteria have to be fulfilled. First, the standard-deviation of LWP from MWR within a 20 min interval should amount to less than a threshold of 1.5 kg m^{-2} . The second one is based on the detection of a potential cloud base with the lidar signal at 1064 nm. Profiles with cloud bases higher than 6 km are treated as clear sky profiles. For that reason, the integrated signal ratio of the lidar is calculated by integrating the profiles from ground to 6 km. Water vapour above this height is mostly negligible. In that way, the lidar can be calibrated in the presence of high clouds.

The time series of the calculated $C_{\text{H}_2\text{O}}$ is presented in Fig. 5.1c. The mean and the standard deviation are 12.77 and 0.36 g kg^{-1} , respectively. Regarding only the time range which is used for the calibration with the RS, the mean amounts to 12.78 g kg^{-1} and the standard deviation to 0.3 g kg^{-1} . The relative error does thus not exceed 3%.

To give an overview, the calibration factors and errors of all presented methods are summarized in Table 5.1. The relative difference between these methods amounts to less than 5%. The IWV method is well suited to avoid errors due to the RS drift.

5.2 Stability of the calibration factors

Having demonstrated that the calibration factors of all the three methods are in a good agreement, the stability of the IWV method is discussed here. Figure 5.3 presents the time series of the calibration factor of Polly^{XT} using the IWV method (black and blue lines). The

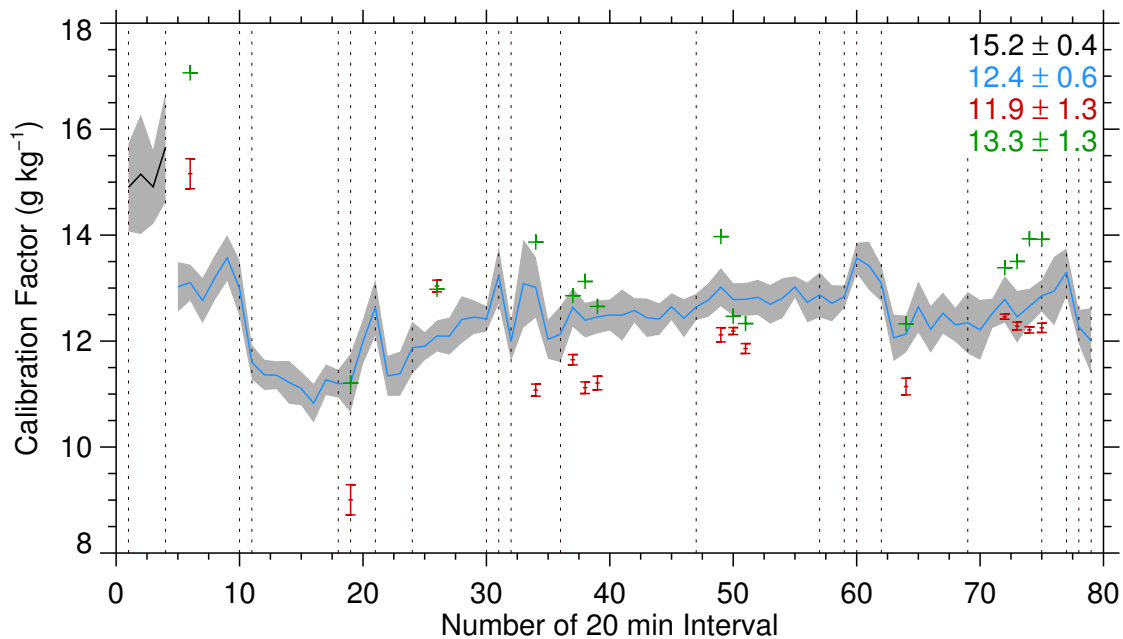


Figure 5.3: Calibration factor of Polly^{XT} using the IWV method as function of time given in number of 20 min interval. The black and the blue solid lines indicate the calibration factor before and after the major rearrangement of the optical setup on 15 April 2013, 10:06 UTC, respectively. The grey areas denote the standard deviation during each 20 min interval. The numbers represent the according means and standard deviations over the time. The grey dotted lines demonstrate rearrangements on Polly^{XT} especially adjustments of the overlap or cleanups of the quartz plate in the roof of the Polly^{XT} cabinet or they indicate leaps in the time of more than 4 h. The calibration factors of the regression and the profile method are indicated by red points with error bars and green plus signs, respectively.

grey areas denote the standard deviation during each 20 min interval. Rearrangements in the optical setup of Polly^{XT} specifically adjustments of the overlap or cleanups of the quartz plate in the roof of the Polly^{XT} cabinet can cause changes in the calibration factor. Such rearrangements or time leaps of more than 4 h are indicated by dotted lines. The means and standard deviations amount to $15.2 \pm 0.4 \text{ g kg}^{-1}$ and $12.4 \pm 0.6 \text{ g kg}^{-1}$ before and after the major rearrangement in the optical setup on 15 April 2013, 10:06 UTC, respectively. These values correspond to relative errors of 3 and 5 % and are comparable to studies of *Mona et al.* [2007] and *Sakai et al.* [2007]. Without any strong rearrangements in the optical setup, the calibration factor is very stable, enabling an operational applicability. This is particularly important during cloudy conditions when no calibration can be performed. In those cases, the calibration factor from the last 20 min clear sky interval can be applied. This is explained in more detail in Sec. 5.3.4.

Table 5.1: Calibration factors and errors of the regression, profile and IWV method.

Method	$C_{\text{H}_2\text{O}} \text{ (g kg}^{-1}\text{)}$	$\sigma C_{\text{H}_2\text{O}} \text{ (g kg}^{-1}\text{)}$
Regression	12.32	0.17
Profile	12.18	1.71
IWV	12.78	0.3

Furthermore, the calibration factors determined by the regression method (red points and error bars) and the profile method (green plus signs) are added to Fig. 5.3. Their uncertainties amount to $11.9 \pm 1.3 \text{ g kg}^{-1}$ (11 %) and $13.3 \pm 1.3 \text{ g kg}^{-1}$ (10 %), respectively. The error bars of the profile method are too large and are omitted for clarity.

5.3 Water vapour measurements

The availability of two Raman lidar systems as well as frequent RS launches allow a statistical analysis of the water vapour profile accuracy. This section starts with an overview over the Polly^{XT} water vapour observation during HOPE. Afterwards, a case study comparing water vapour measurements of Polly^{XT}, BASIL and RS is presented. This part is followed by an extensive statistical analysis showing the accuracy of the IWV method for the whole experimental period in Western Germany. Finally, this section ends with an example of a water vapour measurement in the presence of clouds.

5.3.1 Overview over Polly^{XT} water vapour observations during HOPE

Using the IWV method, it was possible to obtain calibrated water vapour profiles by Polly^{XT} during almost every night from 4 April to 29 May 2013 (Fig. 5.4). The water vapour content in the planetary boundary layer (PBL) is quite variable ranging from about 3 g kg^{-1} on 7 April up to about 8 g kg^{-1} on 8 May 2013. The PBL contains more water vapour than the layers above. However, the water vapour in the top layers was often not observed due to the presence of clouds (e.g. night from 11 to 12 April 2013). A method to derive water vapour also in cloudy cases is presented in Sec. 5.3.4.

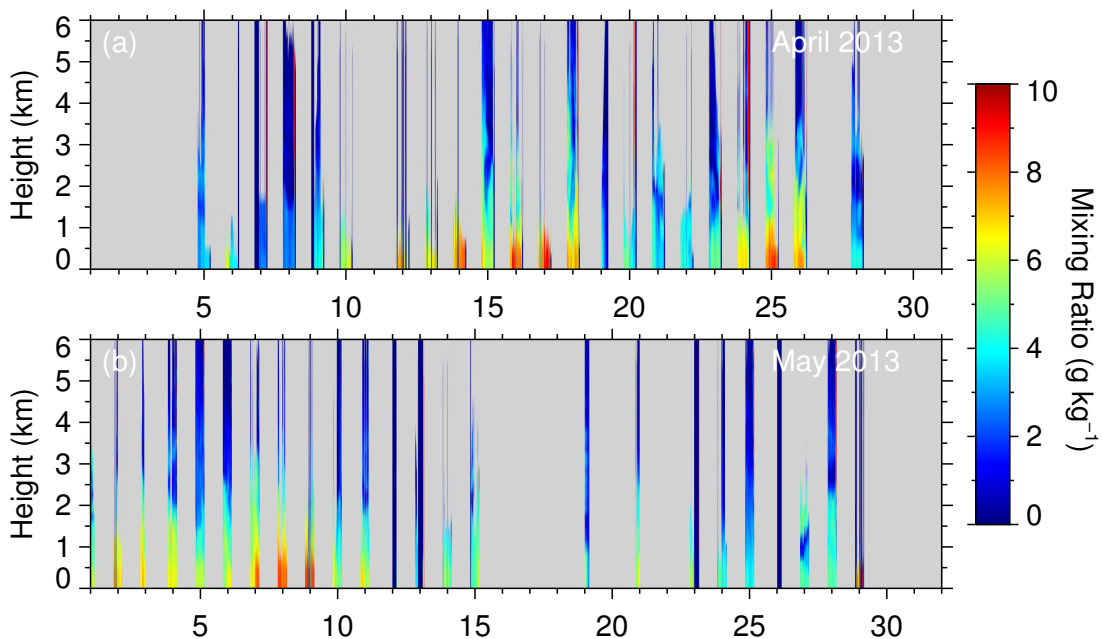


Figure 5.4: Overview over the water vapour profiles observed by Polly^{XT} during HOPE: (a) April and (b) May 2013.

5.3.2 Comparison of water vapour measurements on 4 May 2013

During a night of 4 to 5 May 2013, clear sky conditions were present over the area and all measurement systems were running. Figure 5.5 (a) shows a comparison of water vapour mixing ratio profiles from Polly^{XT}, BASIL and RS at 23:00 UTC. The lidar profiles are averaged over 20 min starting at 23:00 UTC. The vertical smoothing lengths are 90 and 22.5 m for Polly^{XT} and BASIL, respectively. Due to the different vertical resolution, the lidar profiles are interpolated to the RS height grid. All three curves show a similar behavior, except within the PBL up to 1.6 km. Above the PBL top a strong decrease in the water vapour mixing ratio could be observed. The differences between the RS as independent reference and the lidars are illustrated in Fig. 5.5 (b). It can be seen that the differences are quite large in the PBL. The mean difference and its standard deviation in the PBL amount to $-0.14 \pm 0.31 \text{ g kg}^{-1}$ (relative error $-3.2 \pm 8.2 \%$) and $-0.46 \pm 0.45 \text{ g kg}^{-1}$ ($-11.4 \pm 12 \%$) for Polly^{XT} (black) and BASIL (red), respectively. These differences are expected due to the normal water vapour variability in the PBL. Negative values indicate drier RS values.

The largest differences occur at the PBL top down to -1 g kg^{-1} (Polly^{XT}) and -1.37 g kg^{-1} (BASIL) which can be caused by small-scale variability of the PBL height. Above the PBL in the free troposphere (FT) between 2 and 5 km the differences are smaller with values of $0.17 \pm 0.17 \text{ g kg}^{-1}$ ($8.5 \pm 10.5 \%$) for Polly^{XT} and $0.08 \pm 0.17 \text{ g kg}^{-1}$ ($4.8 \pm 8.6 \%$) for BASIL.

5.3.3 Statistical analysis of calibrated profiles

For a statistical analysis of the absolute bias between RS and Polly^{XT}, between RS and Polly^{XT} calibrated with a constant calibration factor of 12.4 which is the average from the IWV method, and between RS and BASIL only clear sky nighttime measurements within

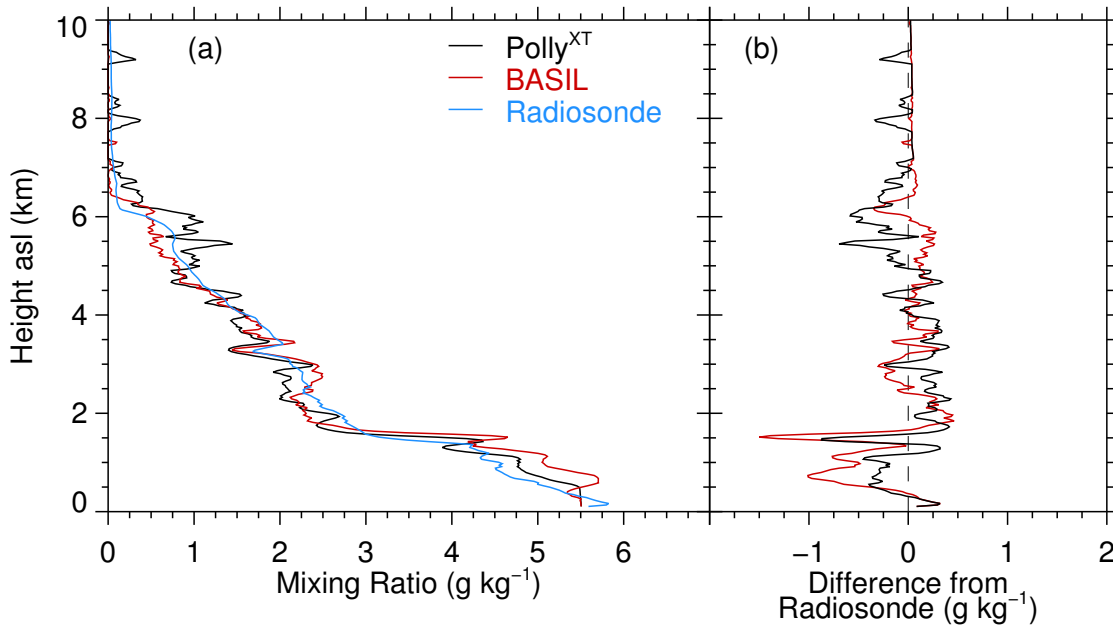


Figure 5.5: (a) Comparison of the mixing ratio profiles from Polly^{XT} (black), BASIL (red) and radiosonde (blue) on 4 May 2013, 23:00 UTC. The lidar profiles are averaged over 20 min. (b) Differences in mixing ratio between radiosonde and Polly^{XT} or BASIL, respectively.

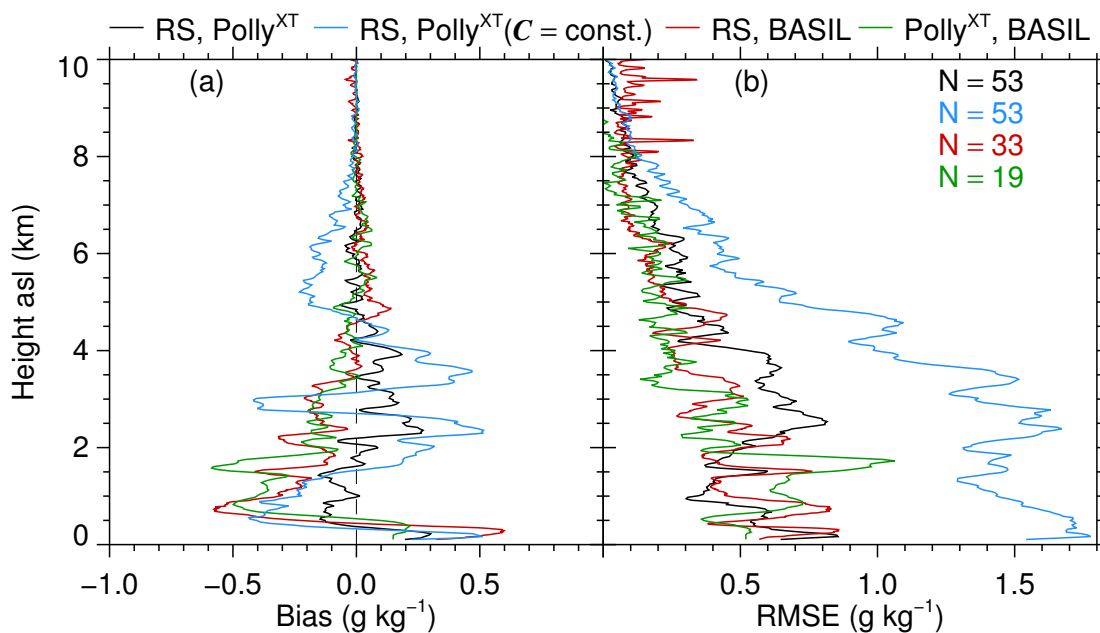


Figure 5.6: Statistical analysis of lidar profiles determined by the IWV method: **(a)** Absolute bias between the radiosonde (RS) and Polly^{XT} (black), RS and Polly^{XT} calibrated with a constant calibration factor of 12.4 (blue), between RS and BASIL (red) and between Polly^{XT} and BASIL (green). **(b)** Root-mean-square error (RMSE) of the water vapour mixing ratio. The numbers indicate the sample size.

less than 2 h before or after the RS launch time are considered. The sample size amounts to 53, 53 and 33 observations, respectively. The profiles are interpolated to the height grid of the lidar and are averaged over 20 min. For the comparison between both lidars only simultaneous 20 min averages are investigated (19 cases). One has to consider that several lidar profiles were compared to one RS profile (e.g. lidar profiles from 21:20, 21:40 and 22:00 UTC to the RS from 23:00 UTC). The Polly^{XT} and BASIL cases are compared to 15 and 6 radiosondes, respectively.

The absolute bias between RS and Polly^{XT}, as well as the absolute bias between RS and BASIL are largest in the lowermost layer from 0 to 0.5 km (Fig. 5.6 a). These biases are induced by the different measurement locations and the missing gluing in the BASIL data. This can have an impact on the mixing ratio of up to 1 g kg⁻¹ in the lowermost 500 m. In the PBL up to about 2 km, the absolute bias between RS and BASIL and between Polly^{XT} and BASIL shows negative values indicating that BASIL measures a higher amount of water vapour. These higher biases in the PBL can be explained by the higher variability of water vapour due to the different measurement locations, since the RS launch site (KIT) is directly situated at the open-cast mining.

The trajectories of the RS up to an altitude of 2 km are shown in Fig. 5.7 (a) split into the trajectories west and east. Figure 5.7 (b) depicts the biases between RS and Polly^{XT} distinguished by the direction of the RS trajectories. When the RS drifts to the east (red), the RS rises in an air mass which is not affected by the pit. In these cases, the bias is close to zero at altitudes from 0.5 to 1 km. During the weaker easterly wind conditions, the RS drifts in

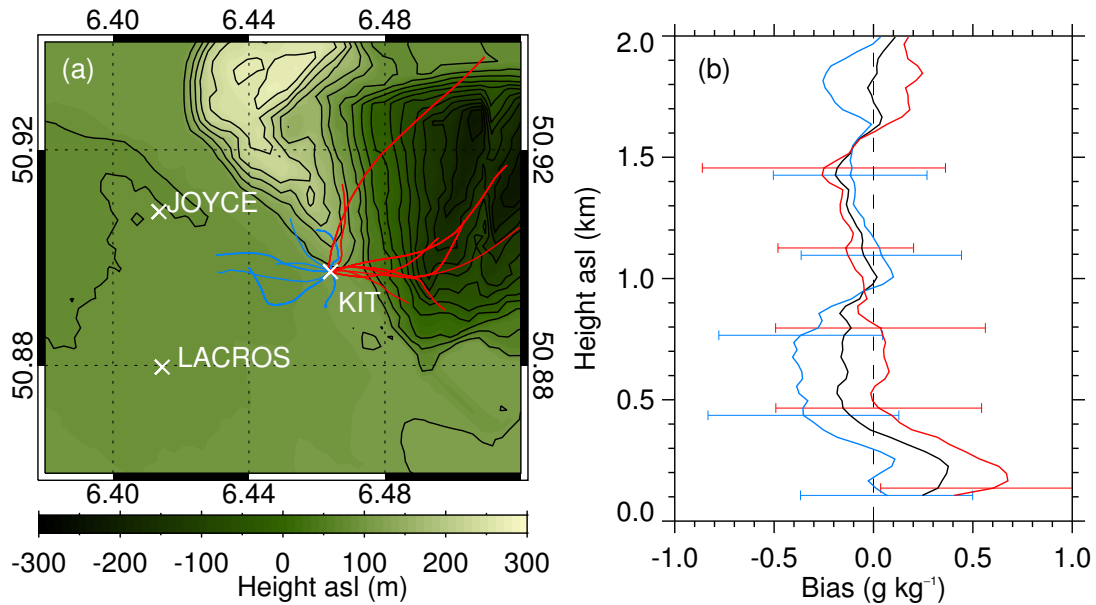


Figure 5.7: **(a)**: Map of the area around Jülich with westward (blue) and eastward (red) RS trajectories. The darker area in the east indicates the open-cast mining and the brighter area in the north indicates a hill named Sophienhöhe. **(b)** Absolute bias and standard deviation (error bars) between the RS and Polly^{XT} distinguished by different trajectories (westward and eastward). The black line indicates the bias considering all trajectories.

an air mass which is strongly affected by the pit, whereas the air sounded by the lidar passes the pit southwards and is therefore not disturbed. Here the lidar and the RS do not profile the same air masses resulting in a higher bias down to -0.4 g kg^{-1} . However, the differences between the biases are in the range of their standard deviations.

Above the PBL the biases converge to zero (Fig. 5.6 a). The bias between the RS and Polly^{XT} shows a small increase at about 2.5 km caused by 4 cases in which the atmosphere changes so fast that the lidar and the RS do not measure the same air mass. In high altitudes no significant biases are noticeable. Obviously, the water vapour amount decreases with altitude and therefore the RMSE also decreases with height (Fig. 5.6 b). The coefficient of variation (CV) also known as relative RMSE increases with height due to the decreasing water vapour amount. In high altitudes the CV is more noisy for all four comparisons.

Table 5.2: Absolute and relative bias for water vapour mixing ratio (mean \pm standard deviation). Values are represented for the layers from 0 to 2 km, from 2 to 4 km and from 4 to 10 km.

	0–2 km		2–4 km		4–10 km	
	Abs. bias (g kg^{-1})	Rel. bias (%)	Abs. bias (g kg^{-1})	Rel. bias (%)	Abs. bias (g kg^{-1})	Rel. bias (%)
RS-Polly ^{XT}	-0.03 ± 0.15	-0.6 ± 2.8	0.14 ± 0.1	7.5 ± 5.1	0.01 ± 0.04	0.6 ± 15.2
RS-Polly ^{XT} (const)	-0.09 ± 0.34	-1.0 ± 4.8	0.24 ± 0.36	8.3 ± 13.8	-0.06 ± 0.11	-15 ± 16
RS-BASIL	-0.2 ± 0.4	-5.3 ± 8.2	-0.15 ± 0.11	-7.2 ± 5.1	0.01 ± 0.04	0.9 ± 26.5
Polly ^{XT} -BASIL	-0.3 ± 0.3	-6.7 ± 6.6	-0.13 ± 0.08	-7.7 ± 2.9	-0.02 ± 0.04	15.4 ± 148.5

The bias of the previously described comparisons is summarised in Table 5.2. It can be seen that the absolute bias is larger in the lower layers up to 4 km than in the upper layer (4 to 10 km). However, large relative biases can occur in the upper layer due to the lower water vapour mixing ratio. In addition, the bias is larger using a constant calibration factor instead of calibration factors determined by IWV method. *Brocard et al.* [2013] found relative biases within 3% up to 3 km during the day, and within 5 to 10% up to 8 km during the night. Values of about $0.6 \pm 0.6 \text{ g kg}^{-1}$ in the altitude range 1.5 to 5.5 km were identified by *Navas-Guzmán et al.* [2014].

5.3.4 Water vapour measurements below clouds

After showing the stability and accuracy of the calibration factor from the IWV method we can calibrate the lidar profiles during all non-precipitating conditions. Figure 5.8 a shows the height-time display of the water vapour mixing ratio from a Polly^{XT} measurement on 16 April 2013, 00:40 UTC. The white area indicates regions inside or above clouds without any water vapour information. The cloud base was determined by the gradient method on the range-corrected signal at 1064 nm [*Baars et al.*, 2008]. The green marked profiles until 01:20 UTC are calibrated with the IWV method, whereas the red marked after 01:20 UTC indicate cloudy conditions. These profiles are calibrated using the averaged calibration factor of the last 20 min clear sky interval (01:00 to 01:20 UTC). Both profiles of the water vapour mixing ratio at 01:00 and 02:20 UTC are in a good agreement below the cloud base (Fig. 5.8 b). With this technique it is possible to provide continuous water vapour profiles

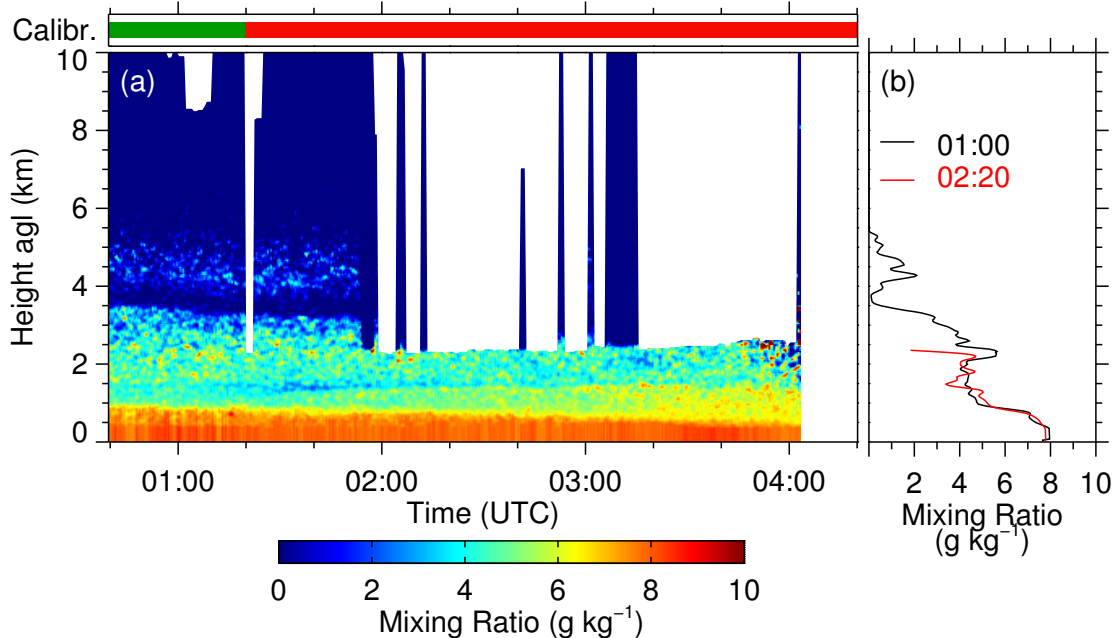


Figure 5.8: (a) Height-time display of the water vapour mixing ratio from a Polly^{XT} measurement on 16 April 2013, 00:40 UTC. White areas are regions in or above clouds without any water vapour information. The bars on the top indicate which profiles are calibrated (green) based on the current IWV from MWR. The red bars denote profiles which are calibrated with the averaged calibration factor from the last clear sky 20 min interval (red). (b) Profiles of the 20 min intervals at 01:00 UTC (black) and 02:20 UTC (red).

up to the cloud base in all non-precipitating night cases.

It could be shown that with a collocated MWR, a reasonable calibration of Raman lidar profiles is possible which will serve as input to the optimal estimation retrieval of water vapour profiles.

6 Retrieval application to LACROS platform during HOPE

The routine application of the algorithm on single profiles as well as time series of collocated Raman lidar and MWR measurements will be presented and compared to RS data. In the following chapter the retrieval application to the LACROS platform with Polly^{XT} and HATPRO during HOPE is presented in case studies and a statistical analysis. During the development of the retrieval, the temporal resolution was increased from 20 to 5 min. Therefore the integration time of the automated calibration module used in the following applications is also switched to 5 min. Nevertheless, the automated calibration of the Raman lidar profiles (Chapter 5) results in a time series of mixing ratio profiles from surface up to cloud base, if present. Such a dataset enables to routinely retrieve full height profiles also from within and above a cloud by applying the two-step algorithm presented in Chapter 4. The Raman lidar Polly^{XT} usually observes water vapour profiles only during night time. The gap during the day can be closed by the application of an optimal estimation technique as proposed in this work, given that a MWR is measuring collocated and simultaneously. The LACROS station provided an ideal opportunity to observe the atmosphere with a Raman lidar and MWR during the HOPE campaign. In this application the covariance from RS climatology (see Sec. 4.1) is used as covariance matrix of each previous profile. This approach results in more reliable profiles. In the last section the derivation of relative humidity profiles is shown.

6.1 Case Studies

6.1.1 Cloud free conditions

In this section the general functionality of the retrieval of water vapour profiles and basic parameters such as averaging kernels and degree of freedom are introduced using a straightforward cloud free case. Figure 6.1 gives an overview of a mostly cloud free day (5 May 2013). It shows the LWP, the height-time display of the mixing ratio measured by the Raman lidar Polly^{XT} and the height-time display of the retrieved profiles after applying the two-step algorithm. The vertical and temporal resolution of the Raman lidar mixing ratio profiles amount to 90 m and 5 min, respectively. In the early morning up to 03:00 UTC the mixing ratio could be measured very well by the lidar (Fig. 6.1 b). With the rising sun the profiles are more and more noisy such that even the lowermost values are disturbed. For that reason the lidar profiles can not be used at all anymore. At 05:00 UTC the water vapour channel is automatically switched off and usually switched on again at 18:00 UTC. The noise decreases after sunset allowing an undisturbed water vapour observation from 20:00 UTC on. An automated depolarization calibration produces a gap around 22:00 UTC. The cloud base height indicates the development of boundary layer clouds which can also be seen in the LWP values during daytime (Fig. 6.1 a). The lidar profiles serve as input to the OEM if they are available. Although there are no lidar profiles during the day, a complete time series of mixing ratio profiles can be retrieved (Fig. 6.1 c). In the following, the retrieval application

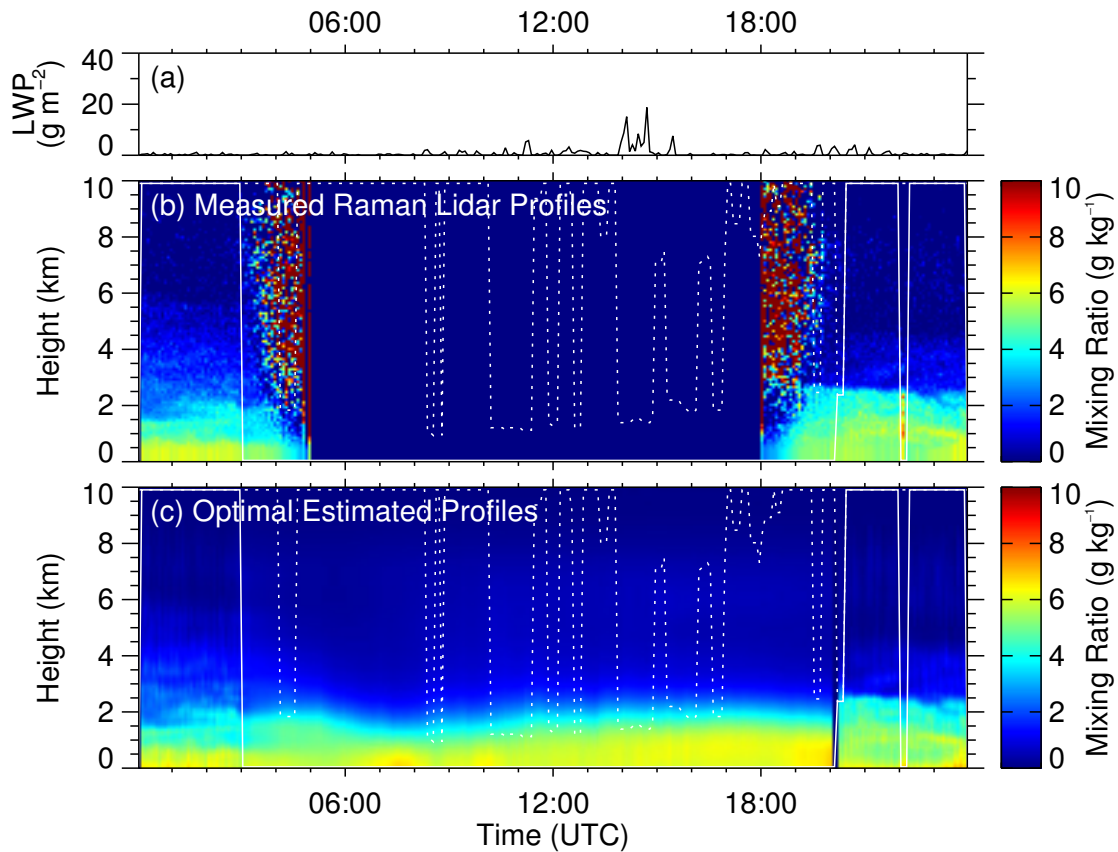


Figure 6.1: Overview of a mostly cloud free case on 5 May 2013. (a) liquid water path (LWP). (b) Height-time display of the mixing ratio measured by the Raman lidar. (c) Height-time display of the retrieved optimal estimated mixing ratio. The solid line indicates the truncation height where the Raman lidar profiles are truncated. The dotted line defines the cloud base height determined by the lidar.

of two different conditions, with full height and without mixing ratio profiles from lidar, are distinguished.

Figure 6.2 illustrates the algorithm processing in the presence of full height calibrated Raman lidar profiles on 5 May 2013, 23:02 UTC. The last analysed state (from 5 min ago) is propagated in time to the estimated state (Fig. 6.2 a). The propagation is an 1 : 1 translation. Its uncertainty is small because it originates in the last analysed state that was also driven by a lidar profile. The plotted uncertainties are the square roots of the diagonal elements of the according covariance matrix. The Kalman filter combines the current lidar measurement and the estimated state to the filtered state that is more driven by the estimated state than by the lidar measurement (Fig. 6.2 b). The filtered profile serves as input (a priori) to the optimal estimation (Fig. 6.2 c). The small uncertainties of the a priori forces the retrieval to resemble the filtered state with similar uncertainties. The precise vertical information from the lidar results in small differences to the RS that is used as reference. The comparison to RS is discussed in detail in the next paragraph. Figure 6.2 (d) shows the averaging kernels for a subset of ten levels. They demonstrate how the information in one retrieved bin is derived from an average of those around it. Ideally the averaging kernels are peaked functions. However, the vertical humidity information at the HATPRO frequencies is limited, which

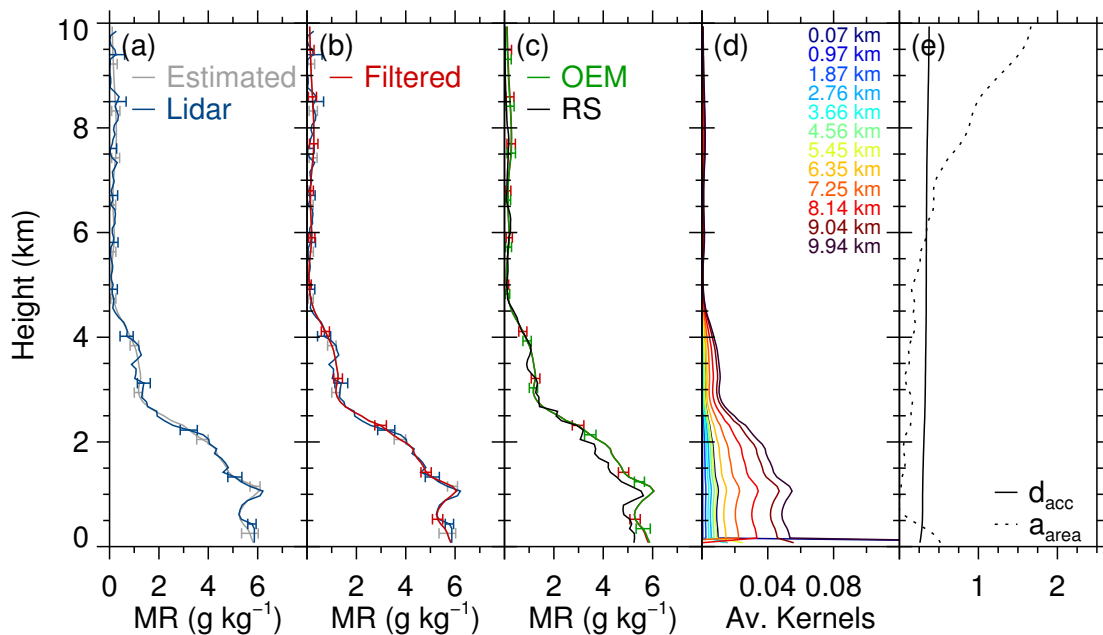


Figure 6.2: Overview of cloud free scene on 5 May 2013, 23:02 UTC. Mixing ratio (MR) profiles from the Raman lidar and the estimated (a), the Kalman filtered (b) and the optimally estimated state (c). Additionally, the mixing ratio of the radiosonde (RS) is shown (c). Error bars are added to the profiles at the different states of the processing. (d) Averaging kernel for a subset of ten levels indicated by the coloured numbers. (e) Accumulated degree of freedom d_{acc} (solid) and the area of the averaging kernel \mathbf{a}_{area} (dotted).

results in smooth functions that are similar to each other. The area of the averaging kernels \mathbf{a}_{area} describes the sensitivity to a unit perturbation. It gives an indication where the MWR observation is sensitive to the true state and where the final information originates. \mathbf{a}_{area} values around unity or differing from unity indicate that the information originates in the observation (\mathbf{z}) or in the a priori, respectively. In Figure 6.2 (e), \mathbf{a}_{area} is close to zero up to 6 km and increases to values around 1.8 in higher altitudes. This means that the MWR observation is not sensitive to the true state, caused by small a priori (Kalman filtered) uncertainty. In this case the retrieved profile is driven by the accurate a priori that originates in the lidar measurement. The information content that comes from the observation is given by the degree of freedom d . Figure 6.2 (e) represents the accumulated degree of freedom d_{acc} which maximally amounts to ~ 0.4 . That means that 0.4 independent pieces of information are added by the observation (MWR and surface value).

As mentioned above, the retrieved optimal profile (OEM) fits well with the RS profile. A more intense comparison is illustrated in Fig. 6.3 (a). Instead of feeding the retrieval with lidar data, one can only use the MWR as well. In this way, the improvement of applying Kalman filtered lidar profiles as a priori is emphasized. In such cases (OEM_{MWR}) the Kalman filter is completely skipped. The according profile with $d = 2$ is added to Fig. 6.3 (a). The uncertainties are larger over the whole profile in comparison to the OEM. Both, the OEM_{MWR} and the MWR profiles from the statistical retrieval (MWR_{stat}) are not able to distinguish vertical structures as indicated by the OEM and RS. For that reason, their absolute differences to the RS are larger than those from the OEM (Fig. 6.3 b). Fur-

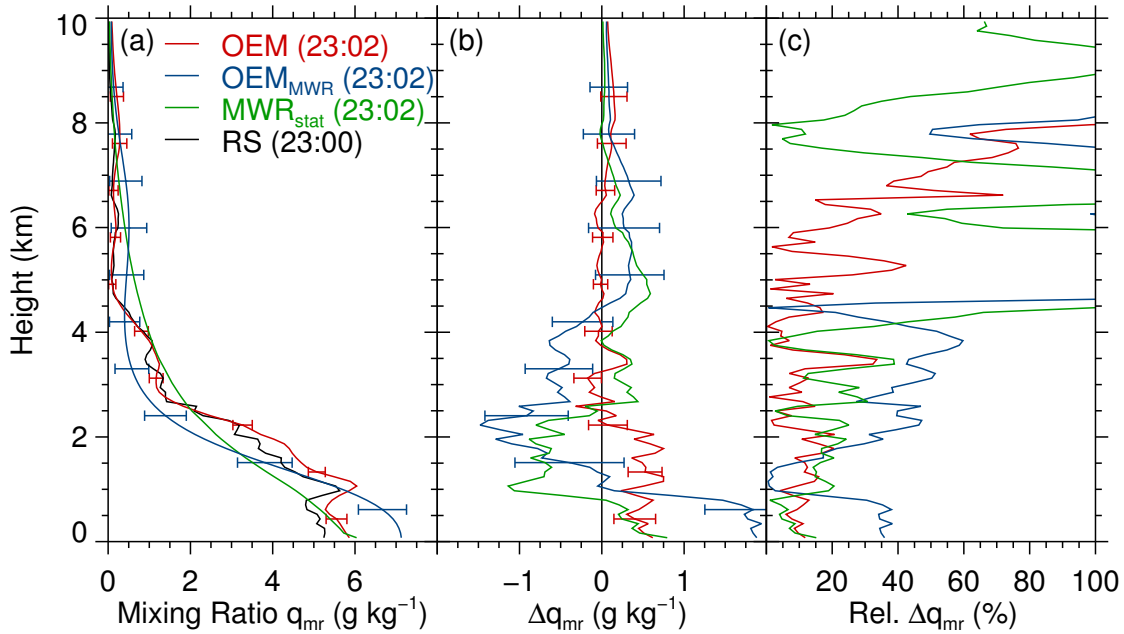


Figure 6.3: **(a)** Comparison of mixing ratio profiles on 5 May 2013 around 23:00 UTC: retrieved profile (OEM, red), retrieved profile with RS climatology as a priori (OEM_{MWR} , blue), profile from the MWR statistical retrieval (MWR_{stat} , green) and RS (black) as reference. Error bars are added to the optimally estimated profiles (red, blue). Absolute **(b)** and relative **(c)** difference from the reference RS.

thermore, in this application the OEM_{MWR} clearly overestimates the humidity below 1 km. The OEM profile fits best and the zero line (no difference) is within the error bars nearly over the whole profile. The relative differences (to RS) are smaller below 4 km and is large in altitudes where the mixing ratio from RS is small (Fig. 6.3 c). In summary, the OEM profile fits best with small uncertainties and differences referred to the RS. However, in cases with full height lidar profiles the optimal estimation is not necessary, because the Raman lidar profiles are already containing nearly all information, as shown in Chapter 5. But full height lidar profiles are only available 18% of the time during HOPE and by applying the OEM the dataset is extended to 60% coverage (see Sec. 6.2).

In contrast to 23:02 UTC there is no mixing ratio profile from lidar available at 07:02 UTC (Fig. 6.4 a). Due to the missing lidar profiles the estimated and the filtered profiles as well as their uncertainties are the same (Fig. 6.4 b). The difference between the filtered and the optimal estimated profile is very small since the atmospheric changes within a 5 min step are quite small. However, the uncertainty decreases near the ground. This is not only caused by the MWR but by the surface measurement which is also part the observation vector (\mathbf{z}). The optimally estimated profile is very smooth, since the HATPRO frequencies do not provide enough information to distinguish fine vertical structures. This can be seen in the difference between the optimal estimated profile and the RS profile which is used as reference. The according averaging kernels (Fig. 6.4 d) are smooth functions that are similar to each other, because the vertical humidity information at the HATPRO frequencies is limited. The area of the averaging kernels \mathbf{a}_{area} is around unity (Fig. 6.4 e). This means that the MWR observation is sensitive to the true state and most information (nearly all) originates in the

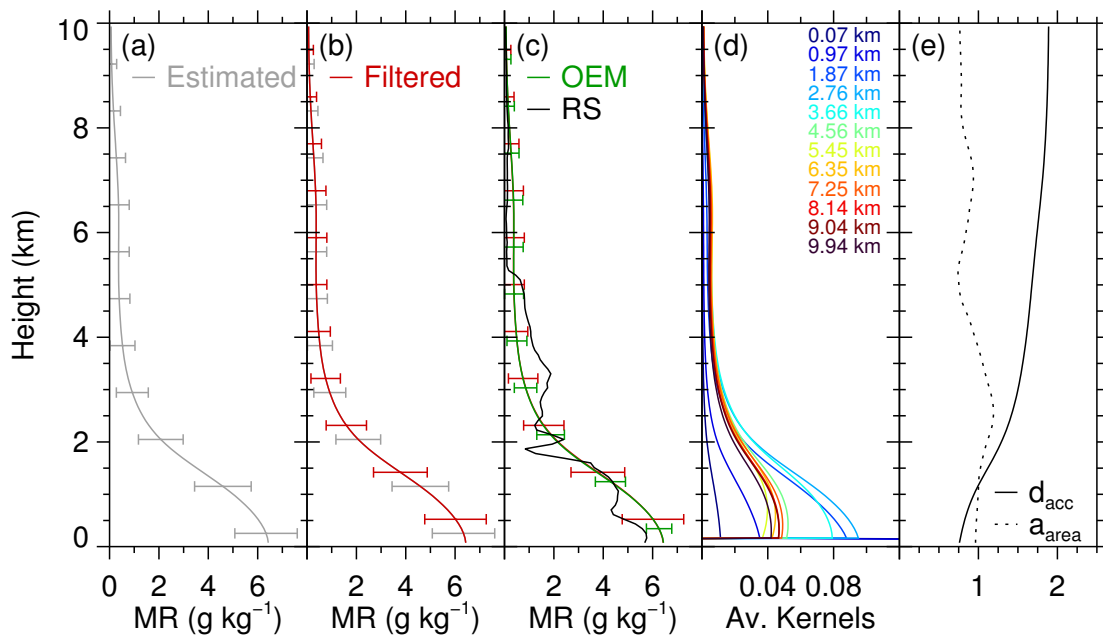


Figure 6.4: As Figure 6.2, but on 5 May 2013 07:02 UTC.

observation (\mathbf{z}). The accumulated degree of freedom d_{acc} maximally amounts to ~ 1.9 meaning that 1.9 independent pieces of information can be retrieved. *Löhnert et al. [2009]* used RS climatology as a priori for different locations and found d values around 2 for humidity profiling with HATPRO. In contrast, one has to consider that here the observation vector is supplemented by the surface humidity which also adds information. The difference might be explained by different a priori covariance matrices \mathbf{S}_a .

In summary, the presence of a lidar measurement results in more accurate retrievals compared to RS, whereas retrievals without water vapour profiles from lidar are mainly driven by the MWR observation for example during daytime. However, the two-step algorithm allows to retain structures from high vertically resolved lidar data to periods without lidar data.

6.1.2 Cloudy conditions

As introduced in section 4.4, liquid water strongly affects the absorption in the microwave region. Therefore, the operation of the retrieval in the presence of clouds containing liquid water has to be treated separately. Figure 6.5 shows an overview of a cloudy day, 21 April 2013. In the course of the day the LWP increases to a maximum of 600 g m^{-2} (Fig. 6.5 a). Between 00:00 and 03:30 UTC the measured lidar profiles reach from ground up to the cloud base between 2.5 and 3.5 km. Referring to the rather low LWP the cloud seems to be an ice cloud. During the day, the mixing ratio is determined on the basis of the MWR observation only disturbed by five short interruptions that are caused by missing cloud base detection by lidar. From 19:30 UTC on the lidar profiles are truncated at the cloud base at around 1.5 km. The LWP shows that these clouds contain liquid water. The possible content of ice water is not relevant for the radiative transfer in the considered spectrum. However, ice clouds as well as all other clouds disturb the precise determination of water vapour with Raman lidar. For that reason the profile is only considered up to cloud base. The problem of truncated

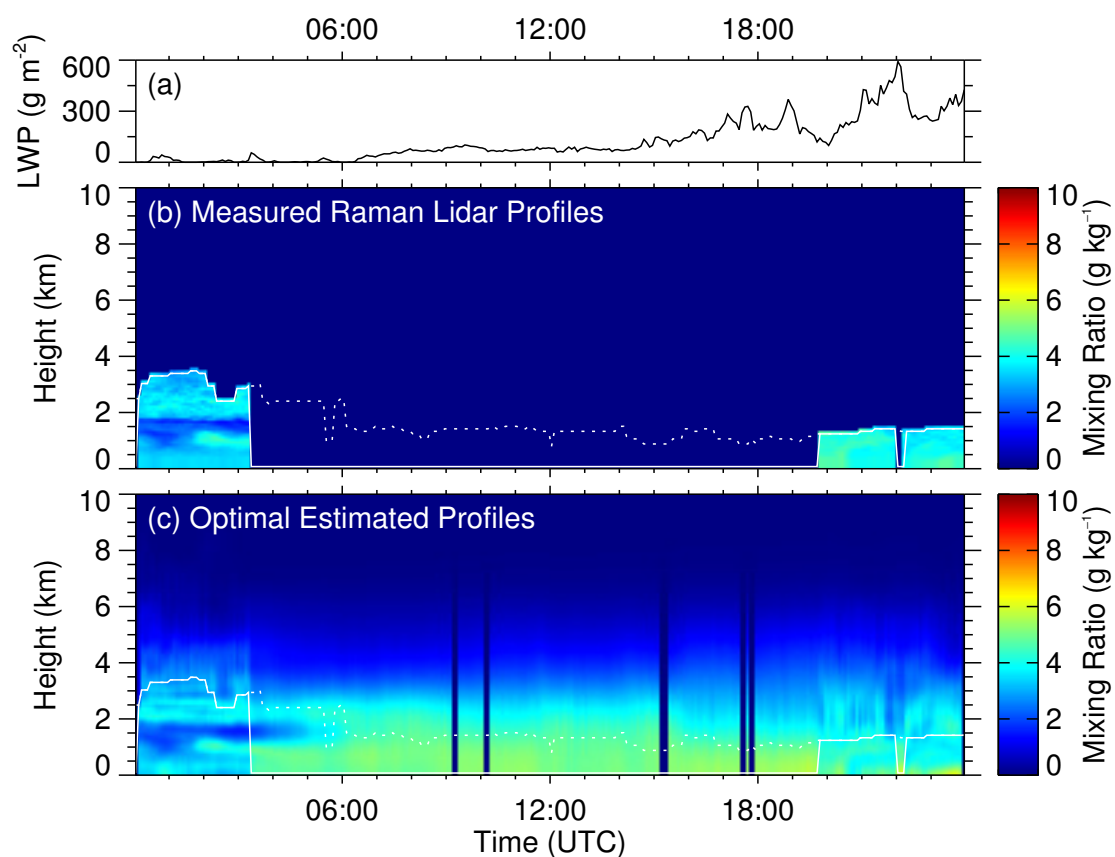


Figure 6.5: As Figure 6.1 but on 21 April 2013

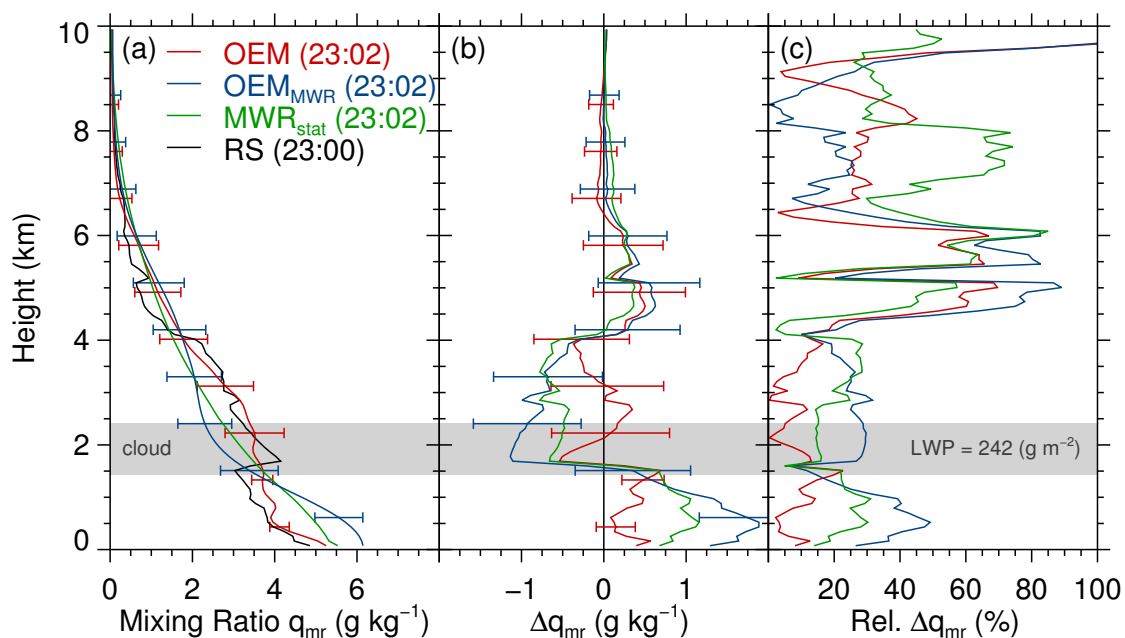


Figure 6.6: As Figure 6.3 but on 21 April 2013. The grey area indicates the cloud with an LWP of 242 g m^{-2} .

profiles is solved by the application of the Kalman Filter (Sec. 4.2). It enhances the profiles up to 10 km by the combination of previous information and the according truncated lidar profile such that a full height profile can serve as input to the optimal estimation.

A comparison between the retrieved profiles (OEM), the retrieved profiles based on climatology (OEM_{MWR}), the MWR profiles from the statistical retrieval (MWR_{stat}) and the RS is shown in Fig. 6.6 (a). There is a cloud with $\text{LWP} = 242 \text{ g m}^{-2}$ between 1.3 and 2.4 km. Both, OEM_{MWR} and MWR_{stat} , are not able to distinguish the vertical structure inside the cloud given by the RS. Furthermore, they show large differences to the RS profile below and slight above the cloud (Fig. 6.6 b). The OEM profile shows a good agreement with the RS profile below the cloud based on available lidar data. The associated uncertainties are small. Within the cloud the uncertainty increases. The profile approximates to the RS. Above the cloud, the OEM uncertainties are in the same range than the OEM_{MWR} profile, whereas the difference to the RS profile is smaller. Nearly over the whole range the RS profile is within the uncertainty range of the OEM profile. The according relative differences to the RS profile are plotted in Fig. 6.6 (c). Up to 4 km the relative difference of the OEM profile is less than 25%. Above this height the relative difference increases. The OEM_{MWR} and MWR_{stat} have larger relative differences to the RS. In summary, the OEM fits best the RS with lowest differences in and above the cloud.

6.2 Statistical analysis

In the previous section (Sec. 6.1) the functionality of the retrieval is introduced based on clear sky and cloudy cases during HOPE. A statistical analysis of the retrieved water vapour profiles during the whole HOPE campaign is presented in the following section. Herein also profiles from RS and the OEM_{MWR} (without lidar) are used as reference.

First, an overview over the calibrated water vapour profiles observed by Polly^{XT} during HOPE is given in Fig. 6.7 (a). The grey area indicates regions without lidar data (up to 6 km) due to cloud attenuation (17 %) and during the day (65 %). The well resolved vertical profiles enable the determination of distinct water vapour structures or inversions that can be seen e.g. at around 1 km in the night between 26 and 27 May 2013.

As introduced in the previous sections, one can use the covariance of the RS climatology as uncertainty from the previous state, instead of lidar data. However, the cloud base height determined by the lidar is necessary. This approach (OEM_{MWR}) is only based on the observation with MWR and surface humidity and is similar to that proposed by *Löhnert et al.* [2009]. The according height time display is illustrated in Fig. 6.7 (b). The gaps (40 %) are caused by rain, MWR breakdowns, flagged MWR data, mostly caused by rain, the absence of cloud base height from lidar or that no solution was found by the retrieval. Nevertheless, the profile availability amounts to 60 %. Though, the data coverage is larger than for lidar, but the vertical resolution is much coarser. This can be seen clearly by comparing to the lidar profiles (Fig. 6.7 a) in the night between 26 and 27 May 2013.

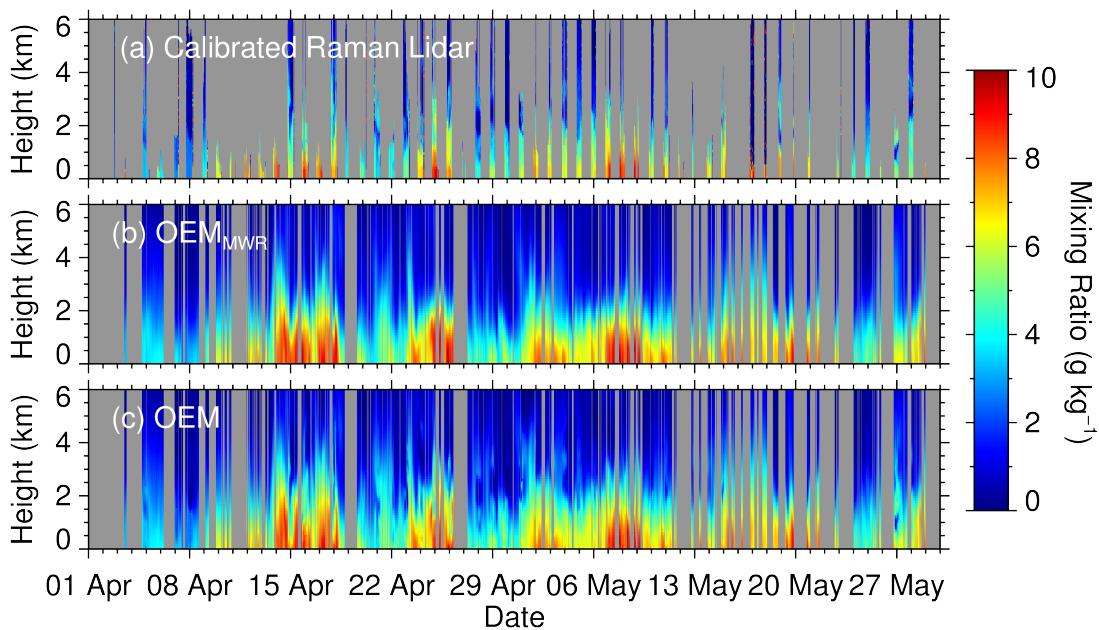


Figure 6.7: Three different Height-time displays of mixing ratio profiles during HOPE: (a) calibrated Raman lidar profiles, (b) optimal estimated profiles only based on MWR (and surface humidity) without any Raman lidar mixing ratio profile (OEM_{MWR}) and (c) optimal estimated profiles based on Kalman filtered Raman lidar mixing ratio a priori profiles (OEM).

Table 6.1: Overview over the different situations depending on Raman lidar mixing ratio (RL MR) profile availability and truncation height (h_{tr}) where the RL MR profile is truncated (due to clouds). The three columns on the right indicate the sample size used for the comparison with radiosonde (RS), to validate the retrieved profiles, and all cases. Furthermore, the profiles that are used for the comparison with RS are separated between those passing and failing the χ^2 test based on a threshold χ^2_{thr} .

	RL MR profiles	Truncation height	Sample size		
			Comparison RS		All
			$\chi^2 < \chi^2_{\text{thr}}$	All	
Full height	yes	$h_{\text{tr}} > 8$ km	102	131	665
Truncated	yes	$0 \text{ km} < h_{\text{tr}} \leq 8$ km	262	291	2010
No lidar	no	$h_{\text{tr}} = 0$ km	1033	1053	5732
OEM _{MWR}	no	—	1397	1475	8407

Figure 6.7(c) shows the retrieved mixing ratio profiles based on the proposed approach which uses Kalman filtered lidar profiles as a priori to the optimal estimation (OEM). The data coverage is nearly the same as for OEM_{MWR}. However, the OEM is able to retrieve fine water vapour structures by means of the lidar profiles. This figure provides an extensive overview over the water vapour conditions during HOPE. The OEM not only enables the distinction between dry (e.g. beginning of April) and more humid (e.g. middle of April) periods but also the vertical distribution of water vapour especially from within and above a cloud.

For a more comprehensive investigation of the quality of the profiles a differentiation between three situations based on certain initial conditions is helpful. These situations are in accordance with the case studies presented in the previous section (Sec. 6.1). The first situation includes cases where a full height lidar profile is available (minimum up to 8 km). Such a case is presented in Sec. 6.1.1 especially in Fig. 6.2. Referred to the statistical analysis these profiles are marked in blue unless stated otherwise. The second group includes cases with lidar profiles which are truncated between 0 and 8 km due to clouds. Such a case is already introduced in Sec. 6.1.2 in Fig. 6.6 and are marked in green from now on. The last group contains all cases without lidar profiles as introduced in Fig. 6.4. The classification into these situation on 6 May 2013 is illustrated in App. A.3. An overview is given in Tab. 6.1. The table also lists the sample size for all profiles and those that are used for comparisons with RS. These are also distinguished between profiles passing and failing the χ^2 test that is discussed later in this section. Additionally, the OEM_{MWR} is used as reference and is marked in grey.

For assessing the accuracy of a water vapour profile, reference profiles from RS and OEM_{MWR} profiles are used. In this work the bias and the root mean square error (RMSE) between the retrieved profiles and those from RS are applied to evaluate the quality of the retrieved profiles (see App. A.2). For this comparison retrieved profiles that are between RS launch time and one hour after launch time are used. This results in maximum 12 profiles for one sounding. Only cases which pass the χ^2 test are considered for the comparison. Figure 6.8(a) shows the bias for the specified situations and for the OEM_{MWR}. The blue line illustrates the retrieved profiles that are based on lidar profiles in minimum up to 8 km (clear sky). It has

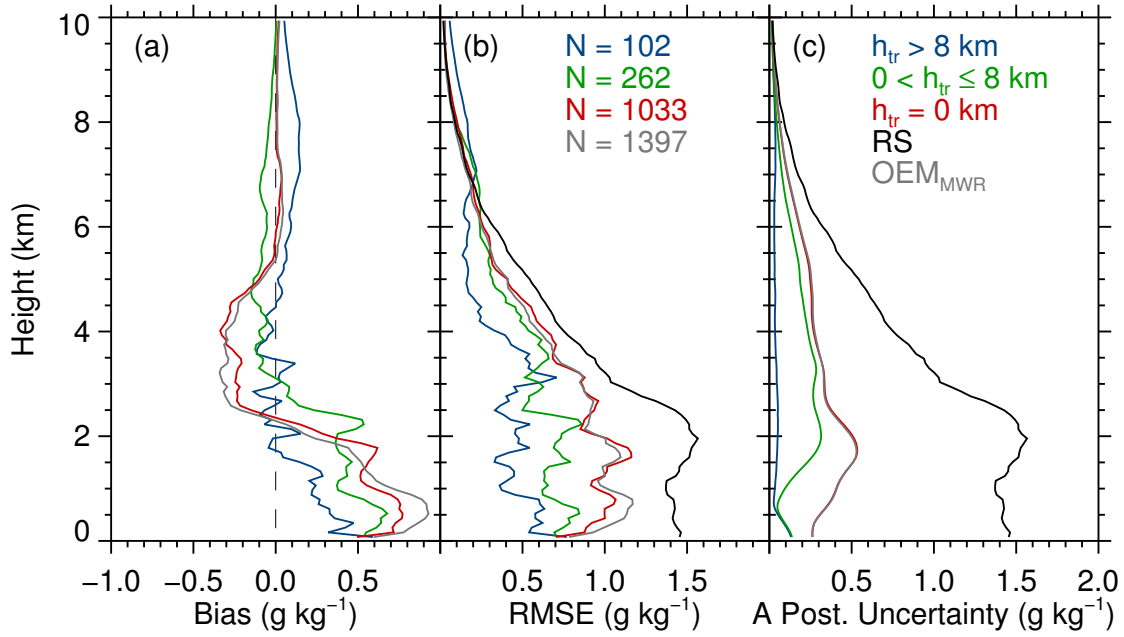


Figure 6.8: Statistical analysis of the synergy improvement: bias to RS (a), root mean square error (RMSE) to RS (b) and a posteriori uncertainty (c). It distinguishes four situations according to Tab. 6.1. The sample size is given by the numbers in the middle panel. Only profiles between RS launch time and one hour after launch time are considered.

a maximum value of 0.5 g kg^{-1} near the surface and it decreases close to zero above 1.5 km. The bias is slightly different in contrast to the calibrated Raman lidar profiles (see Fig. 5.6). This difference is caused by the different sample size (102 and 53). However, the bias is positive that means that the retrieved profiles have larger values than the RS profiles. In high altitudes (above 6 km) the retrieved profiles show higher values than the RS. This issue might be caused by slightly too small determined Raman lidar calibration factors resulting in too small lidar mixing ratios. In these cases, the modelled brightness temperatures for the lidar profiles differ from those measured by MWR. Basically, the uncertainty of Kalman filtered lidar profiles increases with height. This means that the retrieval prevents an increase of the mixing ratio in lower heights due to its small uncertainty. Hence the retrieval tends to overestimate the mixing ratio in larger heights to minimize the difference between both the modelled and the observed brightness temperatures.

The bias of the situations where the lidar profiles are truncated below 8 km is shown in green (Fig. 6.8 a). The values are in maximum around 0.6 g kg^{-1} and are largest in the PBL. Above 2.5 km the bias is around zero. The bias of the situations where no lidar profiles are available and of the OEM_{MWR} show a similar behaviour to each other. Both curves show an overestimation of the retrieved mixing ratio within the boundary layer up to 2 km. Between the 2 and 5 km the retrieval underestimates the mixing ratio by around -0.4 g kg^{-1} . Additionally, the small amount of vertical information that comes from the MWR observation might not be able to compensate this misbehaviour and to resemble the profile given by the reference. This effect can also be seen in the presented clear sky case study in Fig. 6.4. Nevertheless situations where no lidar profiles are available show a bias closer to zero than the OEM_{MWR} . These cases benefit from the night cases whose vertical structure is propagated

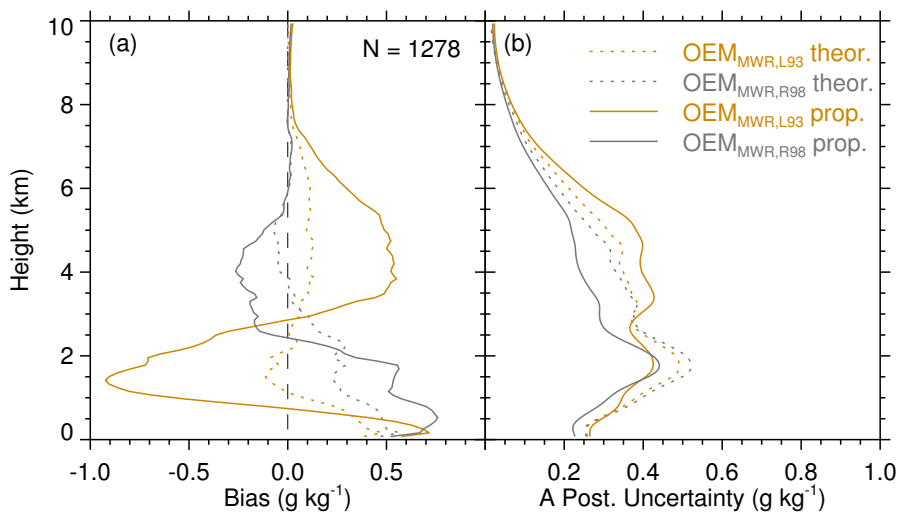


Figure 6.9: Comparison of different forward models, Rosenkranz, (R98, grey) and Liebe (L93, orange): bias to RS **(a)** and a posteriori uncertainty **(b)**. The shown retrievals are only based on MWR but with different a priori states. On the one hand, both a priori profile and a priori uncertainty are taken from the RS climatology (theor.) and on the other hand the a priori profile is propagated (prop.) from the previous step while the uncertainty is taken from the RS climatology. The sample size is given by the numbers. Only profiles between RS launch time and one hour after launch time are considered.

into the day cases. The positive biases of all four curves seem to have a systematic difference that might be explained by some sources of uncertainty in the RS profiles. The different locations of the platform in Krauthausen and the RS launch station and drifts of the balloon might result in the observation of different air masses (see Sec. 5.3.3). Additionally, RS can have a dry bias [Miloshevich *et al.*, 2001]. Naturally, the forward model itself is a source of uncertainty. The modelled brightness temperatures strongly depend on the assumed absorption line shapes [Turner *et al.*, 2009]. Figure 6.9 illustrates a comparison of forward models using two different gas absorption codes, Rosenkranz (1998, R98) and Liebe (1993, L93), [Rosenkranz, 1998; Liebe *et al.*, 1993]. Both models are corrected for water vapour continuum absorption according to Turner *et al.* [2009]. All other parameters, e.g. cloud absorption, are the same. Both forward models were performed under two different a priori states, both without lidar. The first uses the a priori profile and the a priori covariance from RS climatology. It simulates the theoretical uncertainty (theor.) only induced by the different absorption codes. In the other case the a priori profile is propagated (prop.) from the previous state as used in the original retrieval. Herein, the a priori uncertainty is also taken from the RS climatology. The bias to RS in the second case is larger since the theoretical uncertainty is propagated from each previous state resulting in an increase of uncertainty (Fig. 6.9 a). It can be seen that the L93 model has a smaller bias below 1 km. Above 2.5 km the R98 model simulations better fit the RS with a bias around -0.3 g kg^{-1} and a bias close to 0 g kg^{-1} above 5 km. The retrieved uncertainty, the so-called a posteriori uncertainty, of the R98 simulations are smaller than those from the L93. The uncertainty of the L93 runs is also largest in heights above 3 km. Finally, the R98 gas absorption code seems to be more suitable for the presented retrieval. Nevertheless, the forward model is a major source of uncertainty.

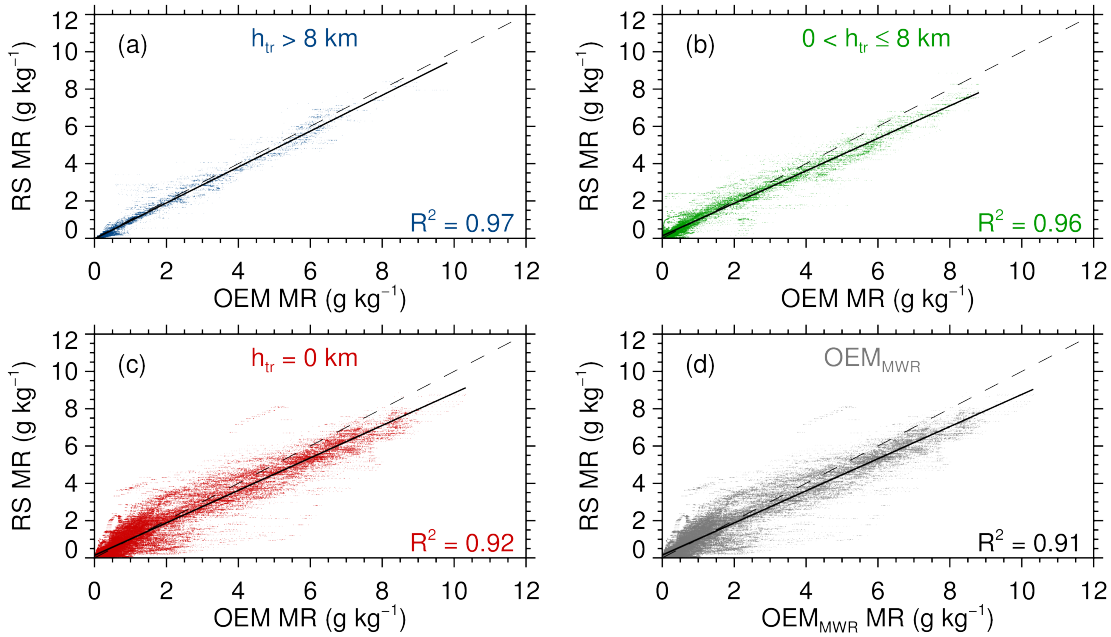


Figure 6.10: Comparison of optimal estimated (OEM) and radiosonde (RS) mixing ratio profiles for four situations given in Tab. 6.1. The black solid line indicates the regression line.

The RMSE between OEM and RS is illustrated in Fig. 6.8 (b). It gives an indication about the statistic error. The RMSE of all four curves decreases with height. In addition, the RMSE is smaller for cases with lidar profiles as a priori and larger for those without. The RMSE of the HOPE RS profiles is larger than any RMSE of the retrieved profiles.

Figure 6.8 (c) illustrates the a posteriori uncertainty of the mixing ratio profiles (see Eq. 4.22). The black line indicates the uncertainty of the RS climatology that is the square root of the diagonal elements of its covariance matrix. It can clearly be seen that the retrieved a posteriori uncertainty is smaller for all situations. The curves of the cases without lidar profiles and the OEM_{MWR} are nearly in agreement. In both cases the Kalman filter is skipped due to the absence of lidar profiles. Therefore both use the same a priori uncertainty and their retrievals are solely driven by the MWR and surface humidity observation. The presence of lidar data (full height or truncated) results in much lower uncertainties. Their small a posteriori uncertainties underline the synergy improvement.

In summary, Fig. 6.8 clearly shows that the application of Kalman filtered lidar profiles enormously improves the accuracy and quality of the retrieved mixing ratio profiles.

Another possibility to evaluate the accuracy of the retrieved profiles is to analyse the dependence between the bias and the mixing ratio. This can be seen in the scatterplot (Fig. 6.10). The slope of the regression line is smaller than the 1 : 1 line. This means that, larger differences occur rather for larger mixing ratios. Figure 6.10 also indicates the correlation between retrieved and RS mixing ratios. The squared coefficient of correlation R^2 is largest for those situations with full height lidar profiles and amounts to 0.97 (Fig. 6.10 a). The R^2 of the OEM based on truncated lidar profiles (b) is slightly smaller (0.96). The coefficients of corre-

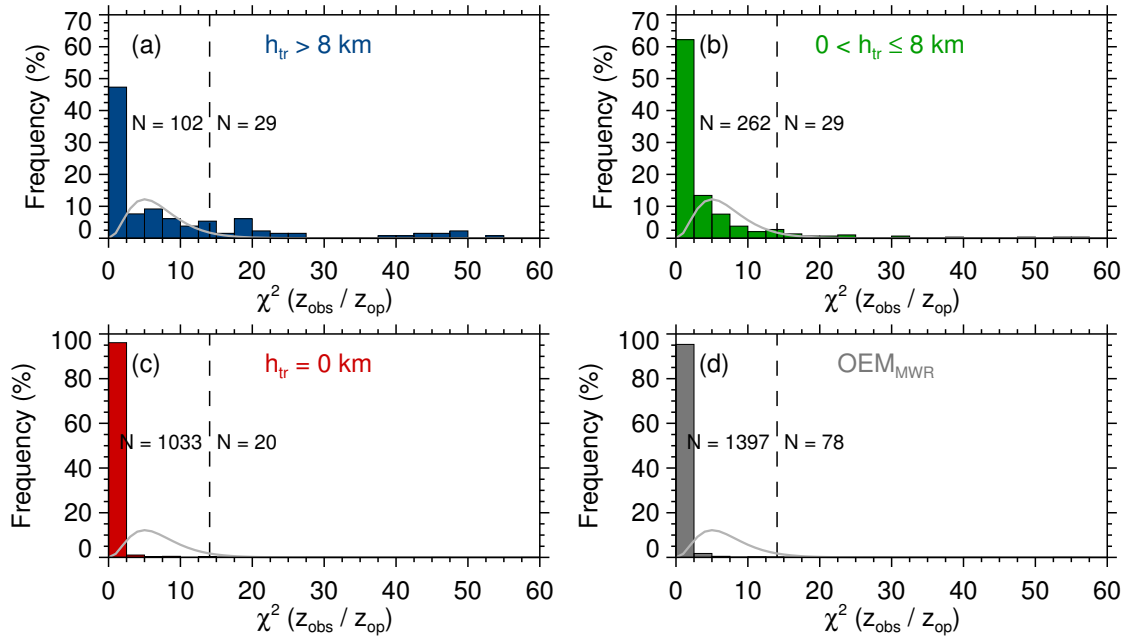


Figure 6.11: Histograms of the χ^2 test for four situation given in Tab. 6.1. The dotted lines indicate the theoretical χ^2 distribution with m_y degree of freedom. Dashed lines indicate the 5% threshold value of 14. The absolute number of cases below and above the threshold value is given to the left and to the right side of the dashed line, respectively.

lation of the situations without lidar data and the OEM_{MWR} have still smaller values of 0.92 and 0.91, respectively. Nevertheless, all cases show a better agreement with RS than the OEM_{MWR} . This illustration also demonstrate the synergy improvement by implementing the lidar data with a Kalman filter before applying the OEM.

To assess the quality of retrieved profiles a statistical test for correct convergence of the solution is applied. The modelled state $\mathbf{F}(\mathbf{x}_{\text{op}})$ and the observation vector \mathbf{z}_{obs} are compared with the error covariance matrix $\mathbf{S}_{\delta z}$ (see Eq. 4.21) to check if the retrieval is consistent with the observation. Figure 6.11 shows the χ^2 test statistics for all mentioned situations. The χ^2 test was introduced in Sec. 4.5. It can be seen that 29 profiles are rejected in the situations with full height lidar profiles because their χ^2 value exceeds the 5% threshold value of 14 (Fig. 6.11 a). The amount of untrustworthy profiles is similar to the situations with truncated lidar profiles. In both cases the smaller a priori uncertainty prevent an adjustment of the modelled brightness temperatures to those measured by MWR. For that reason, their difference is larger resulting in a larger χ^2 value. The χ^2 test relatively reject a smaller amount of profiles for the daytime cases (c) and at the OEM_{MWR} (d). Their larger a priori uncertainty enables a better match between the modelled and the measured brightness temperatures. However all situations show a peak at small values that originates in a very good agreement between the forward modelled optimal state and the observation vector. Admittedly the test is very strict and rejects all failing profiles although they might be realistic atmospheric states. Nevertheless, it enhances the confidence of the retrieved profiles.

A good measure to describe the proportion of information that comes from the observation is given by the degree of freedom. It describes the number of independent pieces of infor-

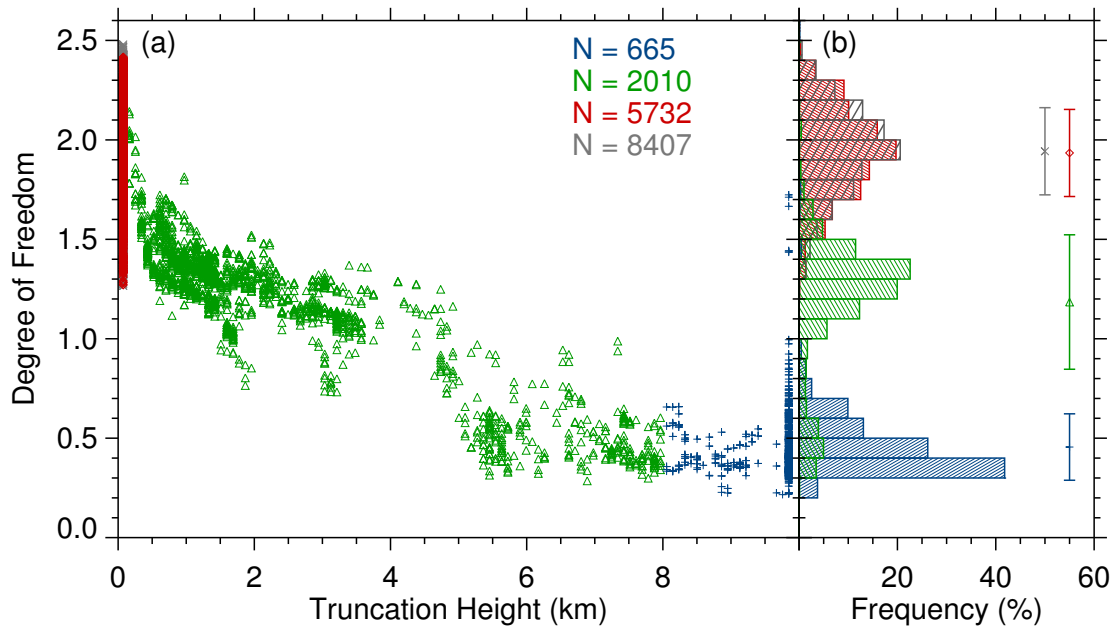


Figure 6.12: **(a)**: Degree of freedom as function of truncation height for different situations introduced in Tab. 6.1. **(b)**: Frequency distribution of the degree of freedom. The symbols and error bars correspond to the according mean and standard deviation, respectively. The numbers indicate the sample size of the considered profiles.

mation that is added by the retrieval and has already been introduced in Sec. 4.5 and 6.1. Figure 6.12 (a) illustrates the degree of freedom as function of truncation height. It clearly demonstrates that the lower the truncation height the higher the degree of freedom. This is caused by the larger a priori uncertainty in cases with truncated or without lidar mixing ratio profiles. The sample size is much higher than in the comparisons above because here all profiles can be used and not only those around the RS launch time. Most of the grey crosses are not visible because they are covered by the red diamonds. The according frequency distributions are shown in Fig. 6.12 (b). Both the OEM_{MWR} and the daytime cases are very similar to each other. Even their mean values and standard deviations are nearly identical with values of 1.9 ± 0.22 . These values are in good agreement with those found by *Löhnert et al.* [2009] for a similar approach. The situations with the truncated lidar profiles show a wide range of values from 0.3 to 2.1. The green distribution also has the largest standard deviation which amounts to 0.34. The situations with full height lidar profiles have the smallest mean and standard deviation with values of 0.45 ± 0.17 . These cases are mostly driven by the a priori information and not by the observation. The variation within each situation is caused by different atmospheric conditions. Figure 6.13 illustrates the degree of freedom as function of IWV. It shows an increase of d with increasing IWV caused by a stronger emission of water vapour. This results in an enhanced influence of the MWR observation with higher d values. Finally, the behaviour of the degree of freedom and especially its dependence on truncation height and hence a priori uncertainty agrees well with similar studies [*Löhnert et al.*, 2009; *Ebell et al.*, 2013].

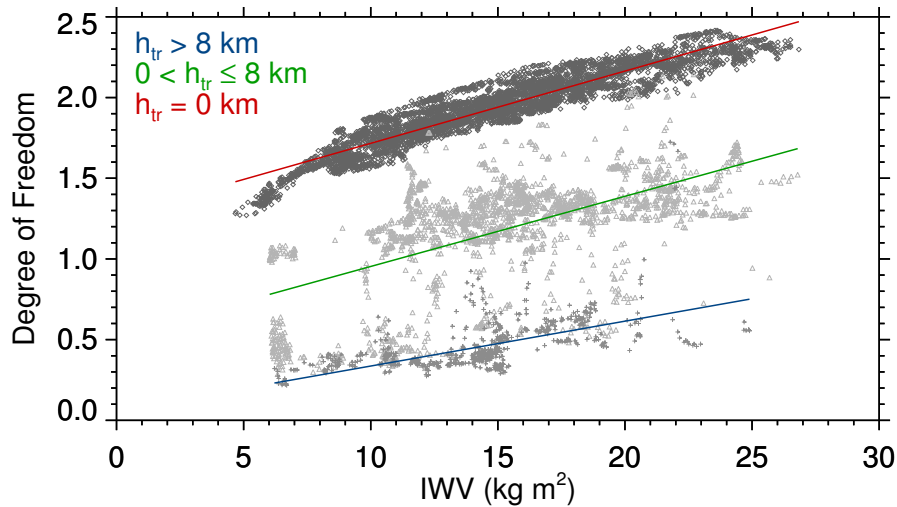


Figure 6.13: Degree of freedom as function of IWV for the situations introduced in Tab. 6.1. The lines indicate the according regression lines.

6.3 Estimation of the relative humidity

The relative humidity (U) is a useful thermodynamic measure for the investigation of cloud formation [van Heerwaarden and de Arellano, 2008] or aerosol hygroscopic growth [Hobbs *et al.*, 1997]. However, it is an effort to derive U with remote sensing methods on an operational basis with a sufficient accuracy and resolution. In the following section, U derived from different methods is described. On the one hand, the original U profiles from the global data and assimilation system (GDAS). On the other hand, U based on humidity retrieved by the OEM and temperature assumptions. These temperature profiles originate from MWR or GDAS. Before comparing the derived U , the accuracy of the temperature profiles from MWR and GDAS, respectively, has to be verified, because of the strong sensitivity of the temperature to U . During HOPE, the LACROS HATPRO was mainly used for zenith observations. Therefore, the derived temperature profiles, based on a statistical retrieval, do not provide the best possible accuracy in the boundary layer that could be improved by measuring at different elevation angles (see Sec. 2.3.1). Besides, temperature profiles from GDAS can be used to derive U based on retrieved OEM mixing ratio profiles. One has to consider that their accuracy is higher than expected because operational RS from the 80 km distant launch station in Essen are assimilated in the model twice a day at noon and midnight. This leads to smaller differences between the temperature profiles from GDAS and the HOPE RS, respectively. The bias and the RMSE to HOPE RS, respectively, are illustrated in Fig. 6.14. Due to the reasons mentioned above the GDAS profiles have smaller bias and RMSE values. It can be expected that the small differences between RS profile and GDAS profiles might be much higher in areas that are further away from operational RS launch stations. Unfortunately, there is no data set available that can be used to check this hypothesis.

The relative humidity (U) is calculated by the ratio of the vapour pressure (e) and the

saturation vapour pressure (E_s):

$$e = \frac{p q_{\text{mr}}}{0.622 + q_{\text{mr}}}, \quad (6.1)$$

$$E_{\text{s,liq}}(\vartheta) = 6.107 \times 10^{\left(\frac{7.5 \vartheta}{238 + \vartheta}\right)}, \quad (6.2)$$

$$E_{\text{s,ice}}(\vartheta) = 6.107 \times 10^{\left(\frac{9.5 \vartheta}{265 + \vartheta}\right)}, \quad (6.3)$$

$$U = \frac{e}{E_s(\vartheta)}. \quad (6.4)$$

Herein, the pressure p is calculated by surface pressure observation from MWR and the barometric formula. One has to differentiate between saturation above liquid water and ice, respectively, depending on the temperature. For the determination of U , temperature profiles (ϑ) from MWR or from the GDAS (Sec. 2.7), respectively, and by the retrieved mixing ratio q_{mr} . In the GDAS data processing, U is based on the saturation vapour pressure E_s that is defined as follows:

$$E_s = \begin{cases} E_{\text{s,liq}} & : 0^\circ\text{C} < \vartheta \\ E_{\text{s,lin}} & : -20^\circ\text{C} < \vartheta < 0^\circ\text{C} \\ E_{\text{s,ice}} & : \vartheta < -20^\circ\text{C}. \end{cases} \quad (6.5)$$

$E_{\text{s,lin}}$ denotes a term that describes a linear transition between saturation above liquid water and ice. U from RS is based on saturation above liquid water. For a consistent analysis, U based on temperature profiles from MWR and GDAS are also determined using the saturation vapour pressure above liquid water.

Figure 6.15 illustrates the bias and RMSE of the relative humidity to RS as reference. It can be seen that the original GDAS profiles show the lowest bias. The reasons are the assimilated RS from Essen and are explained above. Its mean absolute bias amounts to less than 3%. There are only small systematic differences below 1 km (up to 6%) and above 7 km (up to 7%). The bias of the relative humidity based on temperature profiles from MWR and GDAS resemble each other with mean absolute biases of 4.7% and 4.6%, respectively. The

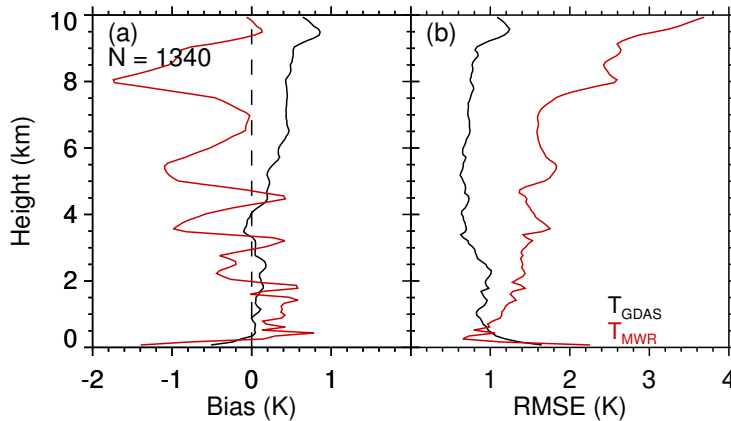


Figure 6.14: Statistical analysis: temperature bias to RS **(a)** and root mean square error (RMSE) to RS **(b)** for MWR and global data and assimilation system (GDAS) profiles. The sample size is given by the number. Only profiles between RS launch time and one hour after launch time are considered.

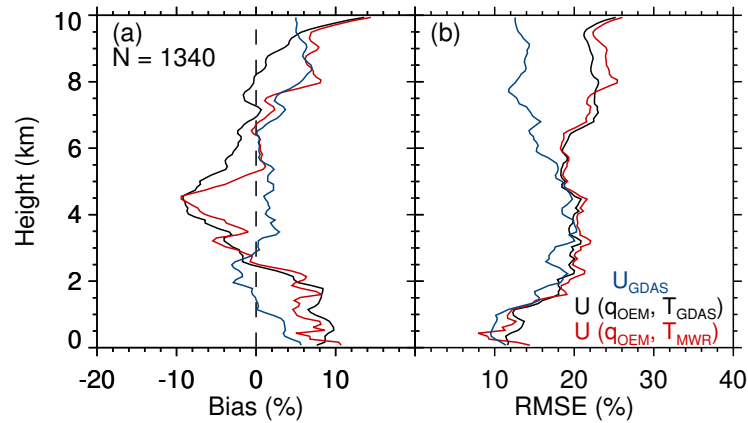


Figure 6.15: Statistical analysis: relative humidity bias to RS **(a)** and root mean square error (RMSE) to RS **(b)**. Temperature profiles are provided by MWR (red) and global data and assimilation system (GDAS, black). The humidity is taken from the OEM. Additionally, bias to RS from relative humidity profiles from GDAS is shown (blue). The sample size is given by the number. Only profiles between RS launch time and one hour after launch time are considered.

shape of the bias is mainly driven by the retrieved mixing ratio profiles from OEM. For that reason it is similar to the mixing ratio bias shown in Fig. 6.8. The RMSE of all three curves is in a good agreement up to 6 km with values around 20%. Above this height the GDAS profiles are less uncertain. Although, the results of the derived relative humidity profiles show larger bias than the GDAS profiles, they might be useful. It can be expected that areas which are not in the vicinity of operational RS launch stations show larger differences. There are around 20 stations in Germany which usually launch RS around noon and midnight. Additionally, the HOPE RS are mostly launched at the same time. For that reason, one could expect a larger uncertainty of the GDAS sounding with a larger time distance to the assimilated RS, especially around 6 or 18 UTC.

7 Retrieval application to other data sets

After evaluating the accuracy of the retrieved water vapour profiles during HOPE in Chapter 6 comprehensively, in this chapter the application on various platforms (JOYCE, RAO, OCEANET) with different instrument types, introduced in Sec. 2, is demonstrated. Additionally, the implementation of the algorithm into the Cloudnet processing is treated.

7.1 BASIL – HOPE

During HOPE, the Raman lidar BASIL (see Sec. 2.2.2) was conducted at the JOYCE site. A HATPRO was measuring collocated and simultaneously. Both, BASIL and HATPRO, can be used for synergistic profiling based on an optimal estimation method as proposed in this work. The advantage of the powerful lidar is the ability of daytime operation. However, BASIL only operated on specific days and was not operating on a routine basis as Polly^{XT}. This results in lower availability (16 %) of calibrated mixing ratio profiles during the two month of HOPE (Fig. 7.1 a). For this application already calibrated Raman lidar profiles which were provided by P. Di Girolamo (University of Basilicata, Potenza, Italy), were used. This also underlines the flexible application of the retrieval. It can be based on calibrated mixing ratio profiles or based on lidar raw data that is processed and calibrated as proposed in Chapter 5.

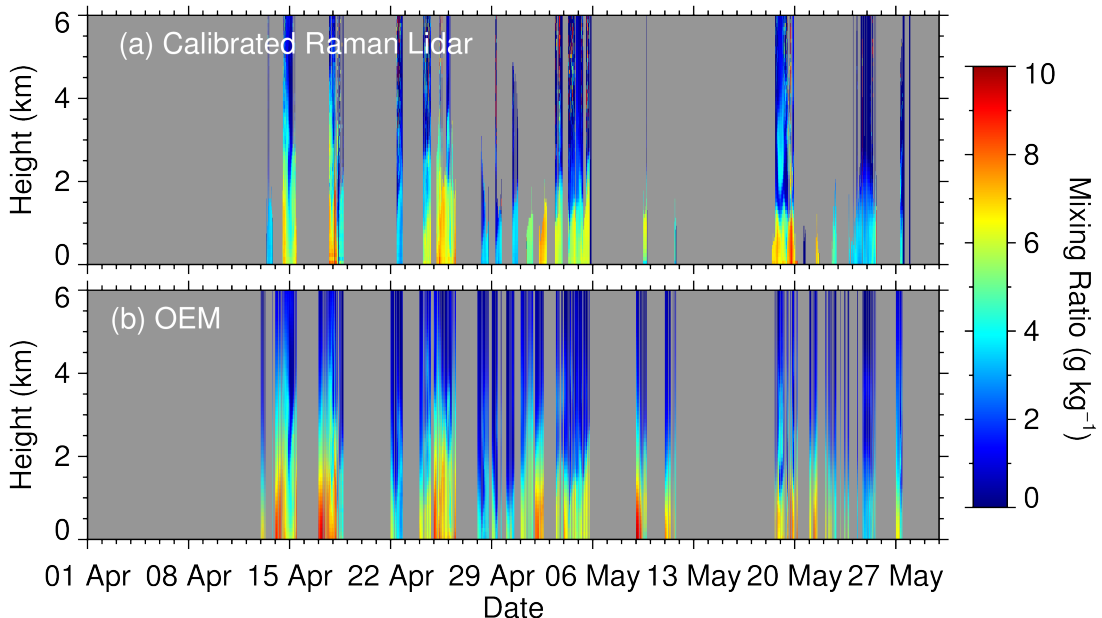


Figure 7.1: Height-time displays of mixing ratio profiles during HOPE: **(a)** calibrated Raman lidar profiles from BASIL and **(b)** optimal estimated profiles based on Kalman filtered Raman lidar mixing ratio a priori profiles (OEM).

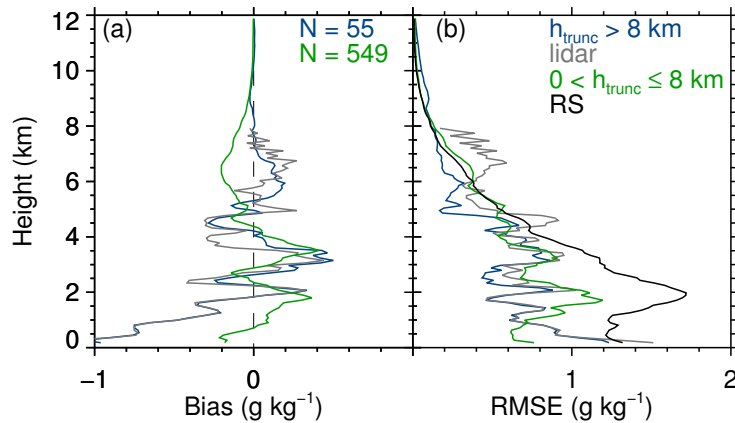


Figure 7.2: Statistical analysis: bias to RS (a) and root mean square error (RMSE) to RS (b) for situations with full height and truncated lidar profiles, respectively. The grey line refers to the calibrated Raman lidar mixing ratio profiles. The sample size is given by the numbers. Only profiles between RS launch time and one hour after launch time are considered.

Figure 7.1 (b) shows the height-time display of the retrieved mixing ratio profiles (OEM). It can be seen that the retrieved profiles are less noisy especially above 3 km compared to the calibrated mixing ratio profiles (Fig. 7.1 a) for example on 4 May 2013. In this application the retrieval was only operated when BASIL was performing. The grey gaps can not be filled due to the lack of cloud base height informations from BASIL. Therefore, the evaluation of the accuracy by comparing to RS is not based on the same differentiation that was introduced in Sec. 6.2. Here, the cases without lidar data are omitted. Another difference to the LACROS application with Polly^{XT} is the presence of lidar profiles during the day which are truncated at around 3 km. Figure 7.2 illustrates the bias and the RMSE to RS, respectively. It is only differentiated between cases based on full height or truncated lidar profiles. Additionally, the bias and RMSE between the calibrated lidar profiles and RS is illustrated. The bias of the retrieved profiles based on the full height lidar cases shows a distorted behaviour. It illustrates a systematic deviation in the lowermost 1 km with values of -1 g kg^{-1} . However, the bias of the calibrated Raman lidar profiles resembles the pattern with similar values. For that reason, this issue is not induced by the optimal estimation method. It seems to be caused by the distance between the RS launch station and JOYCE which amount to 4 km. The bias of the retrieved profiles based on truncated lidar cases shows the same behaviour than the LACROS application between 5 and 8 km. This is induced by the forward model (see Fig. 6.9). The RMSE for the full height cases is slightly smaller than for the truncated cases and it decreases with height. Additionally, the RMSEs are smaller than the uncertainty of the RS climatology.

In summary, the bias and RMSE profiles are as good as for the LACROS application. The BASIL application clearly demonstrates that the accuracy during the day can be increased by the presence of Raman lidar mixing ratio profiles even though they are truncated at around 3 km.

7.2 Polly^{XT} aboard of RV Polarstern – OCEANET

The OCEANET container (see Sec. 2.1.2) equipped with the Polly^{XT} and HATPRO was aboard the research vessel Polarstern during its meridional transatlantic cruise from Cape Town (South Africa) to Bremerhaven (Germany) in Spring 2014. During the 5-weeks trip Polarstern passed several different climate zones, the tropics, subtropics and midlatitudes of both hemispheres. The synergistic use of both, Polly^{XT} and HATPRO, on a ship-based platform, can provide a detailed investigation of the vertical humidity distribution over more than 75° latitude. The cruise track is illustrated in Fig. 7.3. It can be split into 7 legs depending on the IWV observed by HATPRO. The IWV increased with latitude until Polarstern reached the maximum in the tropics (leg III). After leaving the tropics to the north (IV) the IWV rapidly decreased from values around 60 down to 20 kg m⁻². Leg V is indicated by quite constant values in the trade wind zone followed by leg VI which was more variable due to changing meteorological conditions in the extratropics. The last leg shows the lowest IWV values below 20 kg m⁻².

Figure 7.4 gives an overview over the meteorological conditions during the cruise. In the upper panels the IWV and LWP distribution over latitude and time are illustrated (a,b). The IWV is explained in detail in the previous paragraph. The LWP values are highest in the first part of the cruise (leg I to III) with top values up to 1.5 kg m⁻² in the Intertropical Convergence Zone (ITCZ). Lower values are reached in the trade wind zone with shallow stratocumuli clouds under strong temperature inversions [Zoll, 2012]. Leg VI and VII are mainly indicated by periods with higher and lower LWP. However, the IWV is just an integrated measure and does not provide any information about the vertical distribution of

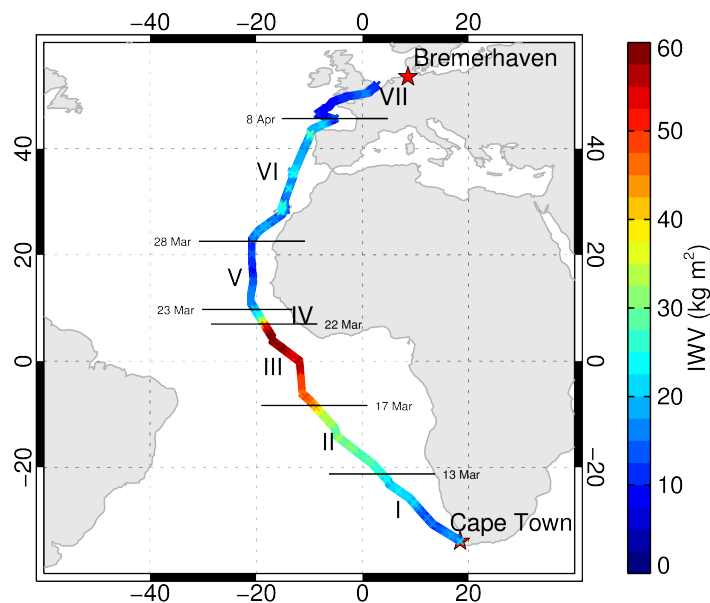


Figure 7.3: Map of the meridional transatlantic cruise of Polarstern (ANT-XXIX/29) from Cape Town to Bremerhaven (stars) during spring 2014. The colour indicates the integrated water vapour (IWV). The cruise is split into 7 legs (Roman numerals) depending on the IWV.

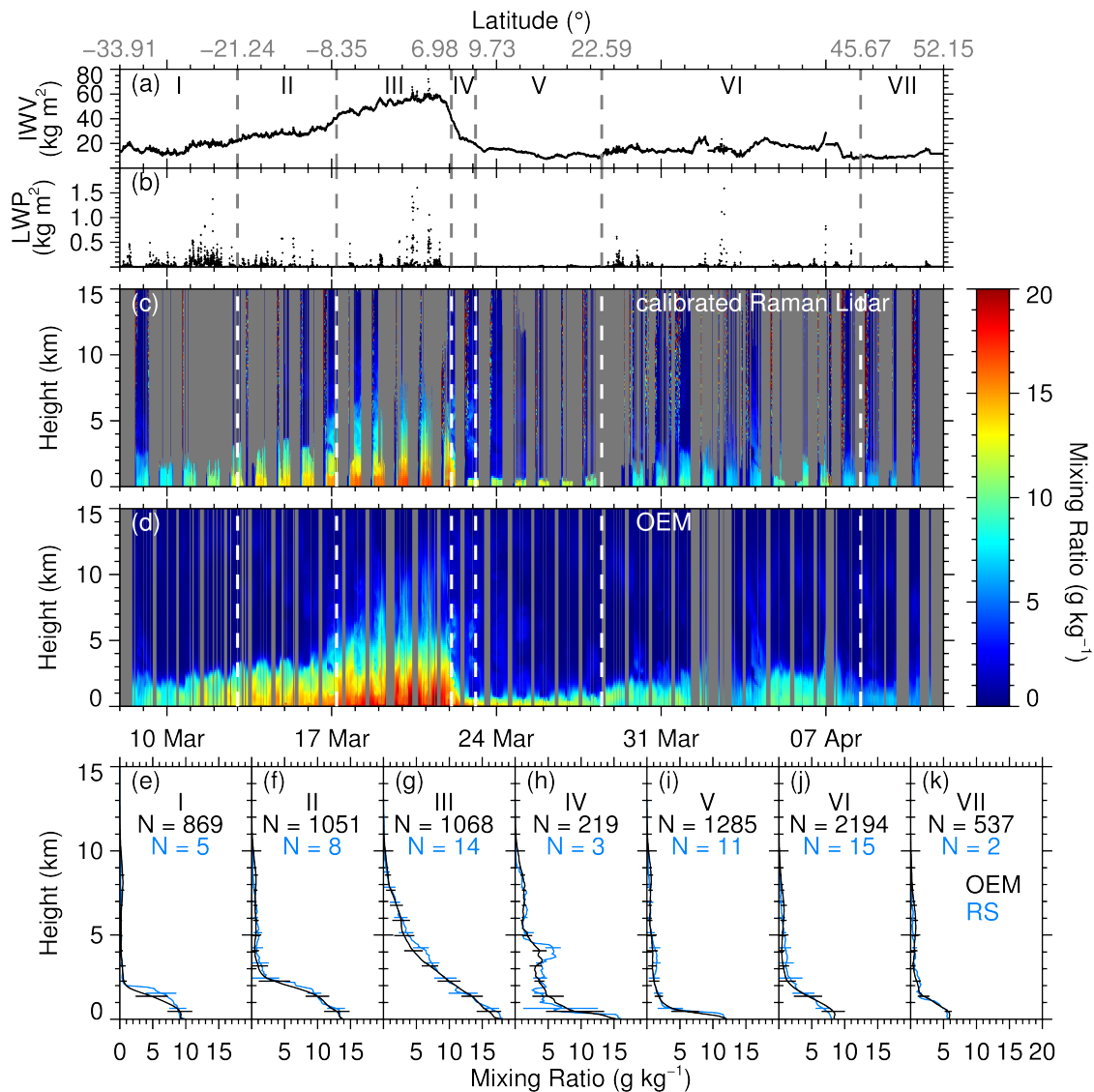


Figure 7.4: Overview of the water vapour distribution above the Atlantic: integrated water vapour (a), liquid water path (b), calibrated Raman lidar mixing ratio (c) and retrieved (OEM) mixing ratio (d). The dashed lines separate seven legs indicated by Roman numbers. The averaged mixing ratio profiles of the OEM (black) and of RS (blue) for the seven legs are illustrated in the lowest panel (e–k). The error bars indicate the standard deviation. The numbers denote the sample size.

water vapour. In contrast, the Raman lidar Polly^{XT} enables height-resolved observations of the water vapour structure. The calibrated mixing ratio profiles are processed according to the approach proposed in Chapter 5 and are illustrated in Fig. 7.4 (c). The water vapour channel of Polly^{XT} is usually switched off during the day due to the strong solar background. Additionally, there is no information from inside and above a cloud which can be seen by truncated profiles, e.g. in leg I. Nevertheless, the vertical distribution of water vapour was observed from surface up to cloud base, if present, or even up to the tropopause during cloud free conditions (e.g. beginning of leg V).

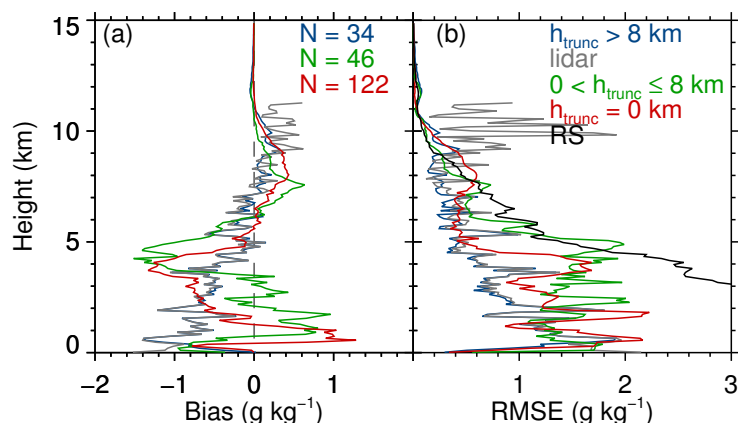


Figure 7.5: Statistical analysis: bias to RS (a) and root mean square error (RMSE) to RS (b). Three situations depending on the truncation height of the lidar profiles are presented. The sample size is given by the numbers in the middle panel. Only profiles between RS launch time and one hour after launch time are considered.

Figure 7.4(d) shows the optimal estimated profiles. Here, the mixing ratio information from within and above a cloud can be retrieved. The coverage with mixing ratio profiles is apparently larger. However, around noon the lidar observation was interrupted due to the low solar zenith angle. In the beginning of April a two day period without retrieved profiles is caused by the rain flag of the MWR. In this time, the rough sea produced sea spray. The sea salt accumulated at the rain sensor of the MWR. This led to rain-flagged MWR data. Unfortunately, the presence of seawater drops which disturb the measurement can not be excluded.

The lowest panel (diagram e to k) illustrates the mean profiles of both, the OEM and RS, for each of the 7 legs. Although, the sample size of the RS is not large enough for a statistical analysis, there is a good agreement between both curves. The OEM is even able to resolve strong gradients in the trade wind zone (leg IV). In addition, the OEM captures the high amount of water vapour in higher altitudes in the tropics (leg III).

A statistical analysis of the accuracy based on the bias and RMSE to RS is given in Fig. 7.5. Here, the same classification depending on truncation height is used as in the previous comparisons. However, the sample size is lower due to the lower amount of RS launches. Generally, the bias and the RMSE are larger than for the previous application caused by several reasons. First, another approach is used as uncertainty of the previous step. The RS data set consists of around 26 000 RS launches above the Atlantic. In case of ship-based measurements the data set reduces since only RS profiles within a spatial range of $\pm 10^\circ$ latitude and within a time range of ± 1 month are used. Additionally, the RS data set is not consistently distributed over the whole Atlantic and over the whole year. For that reason, the RS climatology covariance matrix might exclude typical conditions e.g. strong gradients. Due to the poor RS data set, the retrieved uncertainty of the previous step is propagated in time by adding a transition error which is a fraction (5 %) of the RS climatology covariance matrix (introduced in Sec. 4.1). A poor assumption of the uncertainty of the previous step can cause uncertain or improbable results. Second, due to the ship motions the observation itself is more noisy. Third, a poor temperature profile may lead to uncertainties in the modelled brightness temperatures. The applied temperature profiles are based on a statis-

tical retrieval from HATPRO [Löhnert and Crewell, 2003]. These statistical retrievals are latitude-dependent and strongly depend on the availability of a representative RS data set that means a consistent temporal and spatial distribution and a certain amount of launches to capture various atmospheric structures within the different climate zones. Hence, an uncertain temperature profile is also a source of uncertainty. All the mentioned uncertainties result in a larger bias and RMSE.

The application of the OEM in combination with ship-based observations aboard Polarstern provide a nearly complete cross section of the water vapour distribution and its uncertainty over the Atlantic. The results could be improved by enhancing the amount of RS launches over the Atlantic making the according covariance matrix more representative. Based on a more representative RS data set, statistical retrievals for each climate zone can be generated. This might improve the accuracy of the temperature profiles and finally decrease the OEM source of error.

7.3 RAMSES at RAO

At the Richard Aßmann Observatory (RAO) of DWD in Lindenberg, south east of Berlin, Germany, both Raman lidar and MWR are measuring simultaneously and collocated. In contrast to the applications described above, here MWR from another manufacturer (TP/WVP-3000) is used, based on in principle the same measurement method. The retrieval application is based on already calibrated mixing ratio profiles from the RAMSES lidar, provided by the German weather service in Lindenberg. The calibration is based on RS profiles as introduced in Sec. 5.1. RS are usually launched 4 times a day at RAO. Therefore, RAO provides an ideal opportunity to evaluate the OEM. RAMSES performs water vapour observations also during daytime usually up to around 2 or 3 km. However, the height of incomplete overlap can amount to 1 km during the day. The gap below the overlap height is filled using an interpolation with surface humidity. Additionally, the mixing ratio uncertainty from lidar is manually increased to account for the uncertainties caused by the linear interpolation. In this application, the RS climatology covariance matrix is used as uncertainty from the previous step.

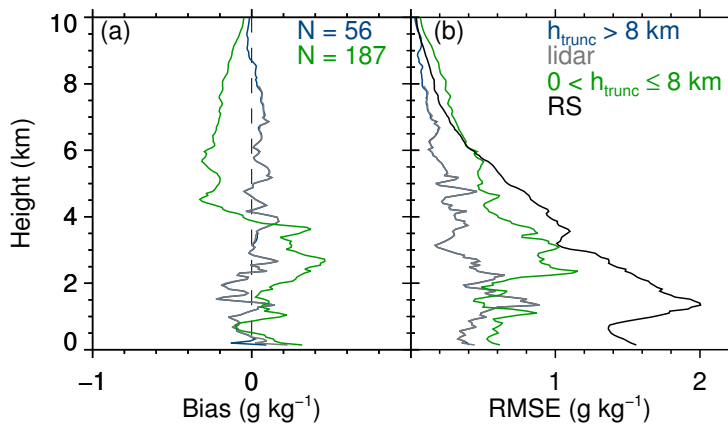


Figure 7.6: Same as in Fig. 7.2, but based on RAMSES lidar and the Radiometrics MP profiler at RAO.

For the evaluation of the accuracy of the retrieved profiles a period from 21 September 2015 to 13 October 2015 is used. Bias and RMSE between OEM and RS are illustrated in Fig. 7.6. Both bias and RMSE are separated into retrieved profiles based on full height or truncated lidar profiles. Additionally, the calibrated full height mixing ratio profiles are plotted. As can be seen, the biases are within a range of -0.4 to 0.4 g kg^{-1} . The bias of the full height cases is close to 0 nearly over the whole profile. Since the calibration is based on RS the bias between the full height lidar cases and RS as well as between the truncated cases and RS is rather low. During the day, the bias of the truncated cases shows the same behaviour than the LACROS application with Polly^{XT} and the JOYCE application with BASIL above the typical truncation height at around 2 km. This is most probably caused by the forward model as discussed in Sec. 6.2. The RMSE of the truncated cases increases above 2 km from around 0.6 to 1 g kg^{-1} . On the one hand, this is caused by the atmospheric variability close to the boundary layer top. On the other hand, 2 km is also close to the truncation height during the day. The small uncertainties (from lidar) below this height drive the retrieval to modify the profile above this height where the uncertainties are naturally higher. Nevertheless, this retrieval application provides amazing results with small mixing ratio uncertainties from within and above clouds and during the day.

7.4 Retrieval implementation to Cloudnet

LACROS comprises a MWR, a cloud radar and a Raman lidar. Based on these instruments the Cloudnet processing can be applied [Illingworth *A. J. et al.*, 2007] providing amongst others cloud categorisation and classification as well as profiles of LWC. In the framework of the thesis the water vapour profiling based on an optimal estimation is implemented in the Cloudnet scheme to be operated on a routine basis. The accuracy and the uncertainty of the retrieval compared to RS is investigated by means of the data collected during HOPE.

Indeed, there are some differences between the retrieval developed in this work and the adopted version to Cloudnet. At first, the water vapour Raman lidar calibration scheme was adjusted and improved to make it applicable to the Cloudnet lidar data format. This results in slightly different calibrated Raman lidar profiles as for the LACROS application (see Chapter 6). Additionally, cloud boundaries (base and top), LWP, **LWC**, **p**, **T** and surface humidity are taken from the Cloudnet data set whereas the brightness temperatures and IWV are externally processed and imported from the MWR data. This step is not yet implemented in the Cloudnet processing.

The presence of a cloud radar enables a much more realistic assumption of the cloud liquid water in contrast to the modified adiabatic single layer assumption used in the LACROS application (Sec. 4.4). A better knowledge about the cloud boundaries improves the radiative transfer (Sec. 4.3) and hence results in more accurate calculated brightness temperatures. However, the Cloudnet data set does not provide temperature profiles from MWR. Instead, Cloudnet is using modelled temperature profiles from the GDAS or COSMO-DE model. The temperature profiles from a MWR usually have a good accuracy in the boundary layer and are more uncertain in the free troposphere [Löhnert *et al.*, 2009; Löhnert and Maier, 2012]. Different temperature profile assumptions influence the radiative transfer and might produce different results. Nevertheless, the temperature profiles from the model are used in the retrieval to retain a consistent data set. Additionally, the Cloudnet instrumentation excludes surface meteorology from a standard weather station. This should be added to the Cloudnet

code. To obtain a value for surface humidity, the retrieval uses the surface values from the model. It is to be expected that the modelled surface values significantly differ from those measured at the Jülich tower. Therefore, the surface mixing ratio error is set to 0.3 g kg^{-1} in the retrieval to account for an uncertain surface humidity assumption.

The proposed OEM contains a supersaturation constraint that adds a penalty to the cost function (see Eq. 4.13) if the retrieval produces unrealistic supersaturation in any height (Sec. 4.5). Due to the absence of information about cloud boundaries a similar constraint dealing with subsaturation within clouds was not implemented. Since Cloudnet provides cloud boundaries the idea became promising again. In theory, the constraint prohibits subsaturation within clouds. But saturation strongly depends on temperature. An uncertain temperature profile also means uncertainty in saturation mixing ratio. At temperature inversions above the observation location that are not resolved by COSMO-DE a temperature error of several Kelvin can be induced, for example. This would lead to an unrealistic saturation mixing ratio and hence to completely unrealistic mixing ratio profiles. The uncertain temperature assumption prevents the benefit of the constraint. For that reason, the subsaturation constraint is not applied.

For an assessment of the accuracy and uncertainties the OEM was implemented in the Cloudnet processing and was applied to the Cloudnet data set at the LACROS site during HOPE. Figure 7.7 shows bias, RMSE and the a posteriori uncertainty of the OEM compared to RS. The sample size is lower than for the LACROS application since there was one more instrument that had to be running simultaneously with the cloud radar. Both bias and RMSE are in a similar range as the LACROS application. In cases with lidar data (full height or truncated) the Cloudnet application is slightly better whereas the cases without lidar data are more uncertain than the LACROS application (see also Fig. 6.8). The increased bias and RMSE of the cases without lidar data might be caused by the higher uncertainty for

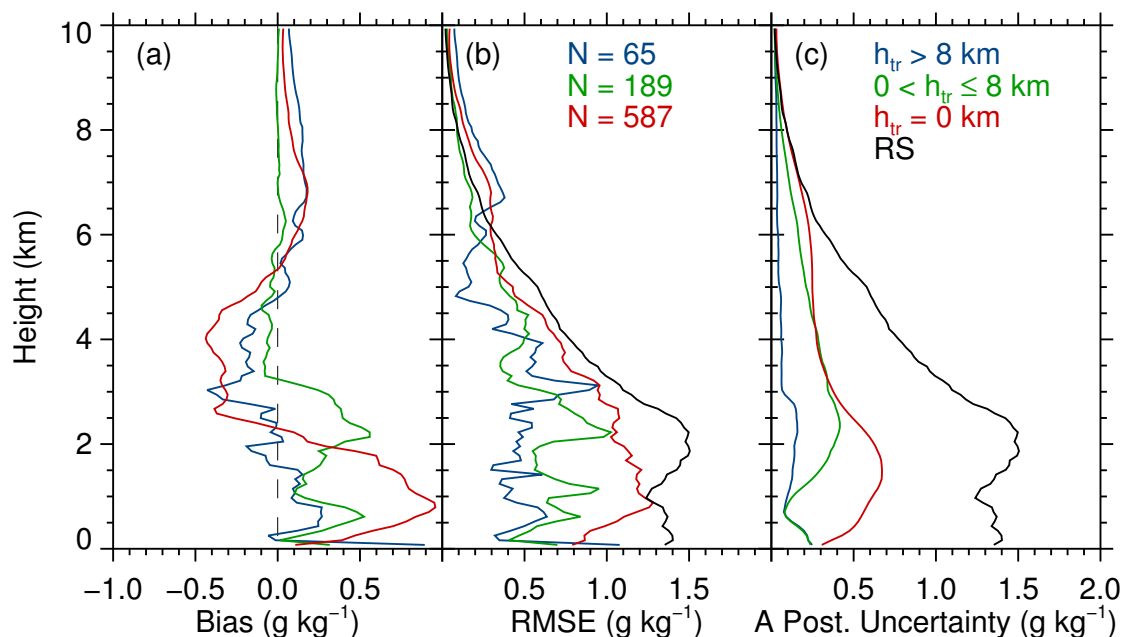


Figure 7.7: Same as in Fig. 6.8, but based on Cloudnet application

temperature profiles which is discussed above. A major drawback is also the missing surface humidity observation that affects the distribution in the PBL due to the correlations between adjacent layers (see Fig. 4.2 a). The a posteriori uncertainty (Fig. 7.7 c) of the Cloudnet application is slightly larger since the a priori uncertainty is increased. This can be seen in the a posteriori uncertainty for the full height lidar cases. The revised calibration scheme uses a height dependent temporal averaging. The lowest layers are not averaged over time. The layers between 3 and 5 km are averaged over 3 profiles and the layers above over 5 profiles. Since the Raman lidar uncertainty decreases by smoothing the uncertainty decreases with height. This preserves small scale structures in the PBL and leads to more accurate profiles below 3 km as can be seen in the bias compared to the LACROS application.

Finally, the optimal estimation was successfully implemented into the Cloudnet processing. A better knowledge of the water vapour distribution consistent with other cloud variables might improve the understanding of cloud formation, evaporation, precipitation and entrainment rates.

Cloudnet can be enhanced by adding new modules such as an aerosol module that is developed by Tropos within HD(CP)².

8 ICON model evaluation

The accuracy and uncertainty assessment of the mixing ratio profiles from the OEM, showed that the retrieval has high potential to be used for model evaluation. In the presented work the OEM profiles are applied to evaluate the ICON-LEM that is the high resolution version of ICON (see Sec. 2.6). Until the completion of this thesis the ICON model runs provide data for six specific days during HOPE. The humidity profiles from ICON are extracted for both LACROS and JOYCE site. This section gives a brief insight in the model evaluation possibilities when a continuous time series of water vapour profiles from OEM based on Raman lidar is available.

8.1 ICON evaluation using OEM based on Polly^{XT} at LACROS

Figure 8.1 illustrates a comparison of profiles between OEM and ICON on 25 April 2013. The upper panel (a) shows the time series of mixing ratio profiles from OEM based on Polly^{XT}. Missing MWR data produces gaps in the morning and during the day. Nevertheless, there is sufficient data to compare the OEM to ICON (b). The difference between OEM and ICON time series is illustrated in Fig. 8.1(c). Although the OEM profiles during the night are mainly driven by the accurate full height lidar information, there are differences of about 2 g kg^{-1} between OEM and ICON. These differences might be caused by ICON which is here much more uncertain than the lidar. ICON does not reproduce the strong gradient at around 4 km and there is a difference at the PBL top. In larger heights both OEM and ICON are in a good agreement with small deviations.

The vertical humidity distribution within the PBL shows differences during the day. The absence of water vapour information from lidar during the day results in more uncertain OEM profiles (see Sec. 6). Hence, larger uncertainties of the OEM during the day hinder a conclusive statement. This underlines the demand of daytime operation of water vapour Raman lidars even though the profiles would be truncated at around 3 km.

8.2 ICON-LEM evaluation using OEM based on BASIL at JOYCE

In addition to night time profiles, the Raman lidar BASIL (Sec. 2.2.2 and 7.1) is able to provide mixing ratio profiles up to about 3 km also during daytime. This capability improves the accuracy of the OEM profiles. Hence, the OEM application on BASIL data at JOYCE enables a more comprehensive evaluation of the ICON humidity profiles.

An overview over the time series of OEM, ICON and its difference, respectively, on 25 April 2013 (same day as in Sec. 8.1) is given in Fig. 8.2. Although the BASIL profiles are more reliable during the day compared to Polly^{XT}, there are differences between OEM and ICON. ICON overestimates the water vapour amount within the PBL. Above the cloud layer the OEM uncertainties increase due to the absence of lidar information. Here the retrieval is not able to resolve fine structures or strong gradients. Hence the dry layer at 4 km modelled by

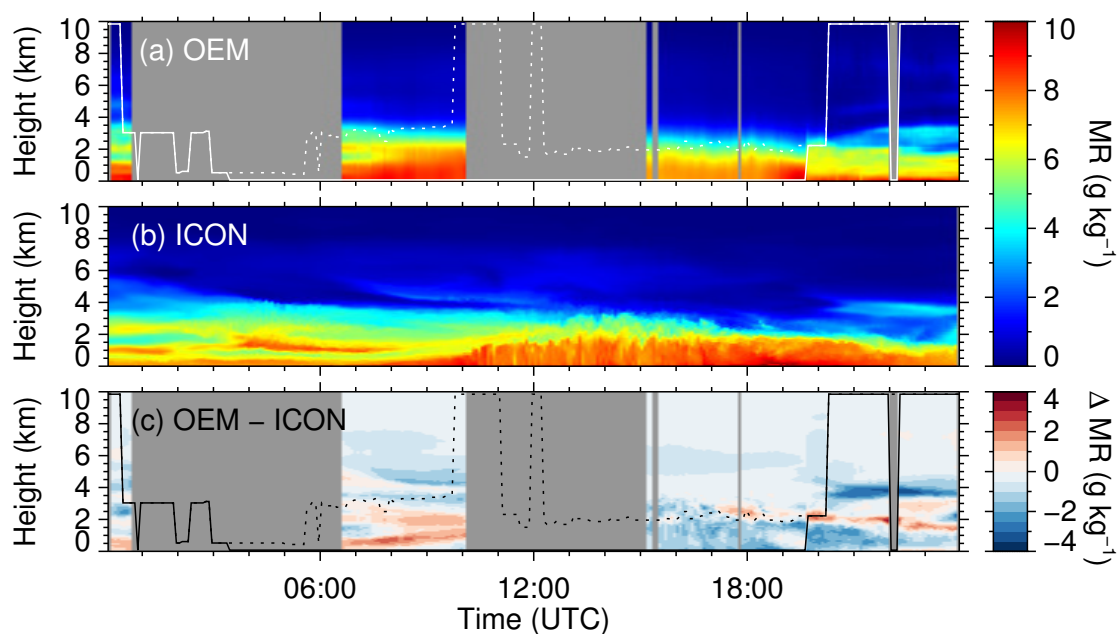


Figure 8.1: Height-time display of the mixing ratio profiles derived by the OEM (a) based on Polly^{XT}, from the ICON model (b) and their difference (c) on 25 April 2016. Solid and dashed lines indicate the truncation height and the cloud base height in (a) and (c), respectively. Both OEM and ICON are shown for the LACROS site in Krauthausen during HOPE.

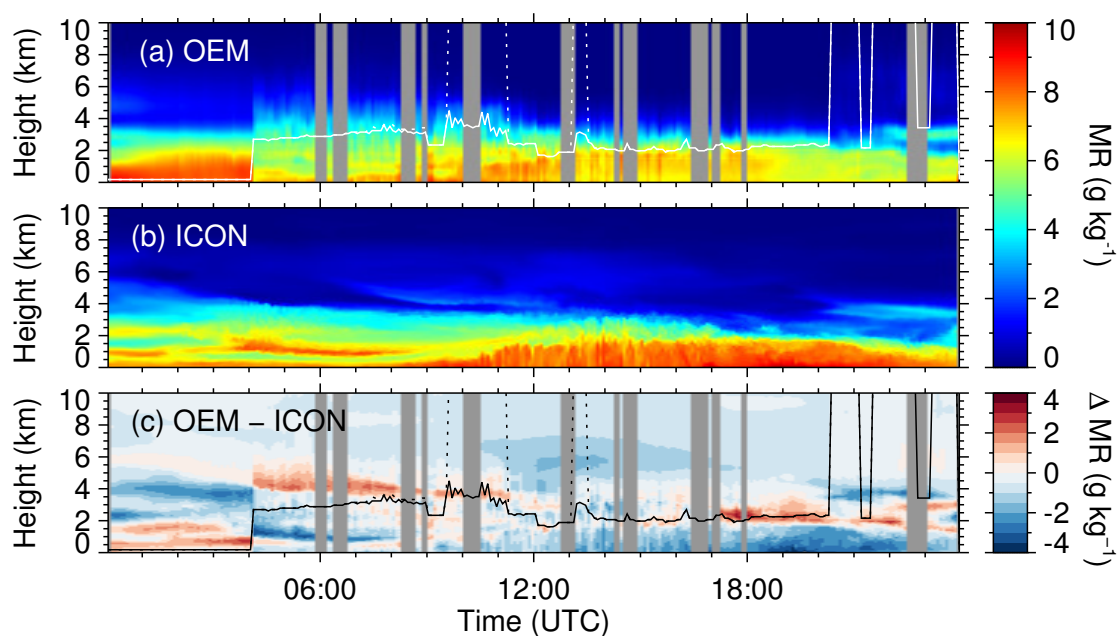


Figure 8.2: Same as Fig. 8.1 but for JOYCE on 25 April 2016.

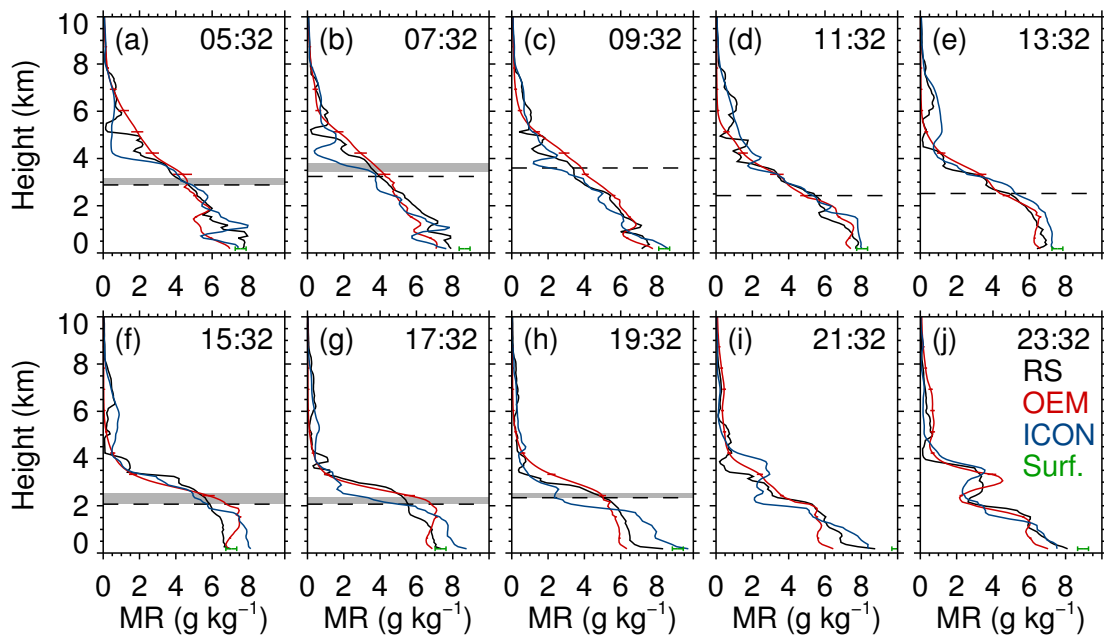


Figure 8.3: Comparison of the mixing ratio profiles of OEM (red), ICON (blue) and radiosonde (RS, black) at ten RS launches on 25 April 2013 during HOPE. The OEM is based on BASIL data at JOYCE. The Icon profiles were extracted for the JOYCE site. Additionally, the OEM error bars as well as surface humidity with error bars are shown. The grey area indicates liquid water clouds as used in the OEM. The dashed line marks the truncation height of the lidar profiles. The time of each comparison is 30 min after RS launch time to account for the RS ascent time through the atmosphere.

ICON between 04:00 and 09:00 UTC can not be evaluated but might be correct. For that reason radiosonde launches are taken into account to verify the water vapour distribution with an independent reference instrument.

The 25 April 2013 is a so-called intensive observation period (IOP 7) during HOPE where 10 RS were launched. The profiles of the OEM, ICON and RS are contrasted in Fig. 8.3. It can be seen that above the lidar truncation height (mostly between 2 and 3 km) the OEM is not able to resolve strong gradients as in 5 km height (a). However, ICON strongly overestimates this dry layer in its vertical extent. There are also larger differences between the three profiles within the PBL. Additionally, the ground values are in a disagreement with the surface humidity from the Jülich tower, especially for the morning and evening cases (b),(i) and (j). This might be induced by near-surface inversions. An investigation of the bias and the RMSE between both OEM and ICON to RS for the 10 RS launches is beneficial to quantitatively assess the agreement with RS as reference on 25 April 2013 (Fig. 8.4). It can be seen that both OEM and ICON have a significant bias in the PBL, but with different signs and magnitude. The surface humidity is moister than RS ($\sim 0.6 \text{ g kg}^{-1}$). This is similar to that from ICON. Above the PBL between 1.5 and 3 km the bias of the OEM is closer to zero than ICON. Additionally, the OEM has smaller RMSE (b). From 3 to 10 km the ICON bias is very close to zero with decreasing RMSE.

In summary, the brief investigation of the discrepancies between OEM, ICON and RS in-

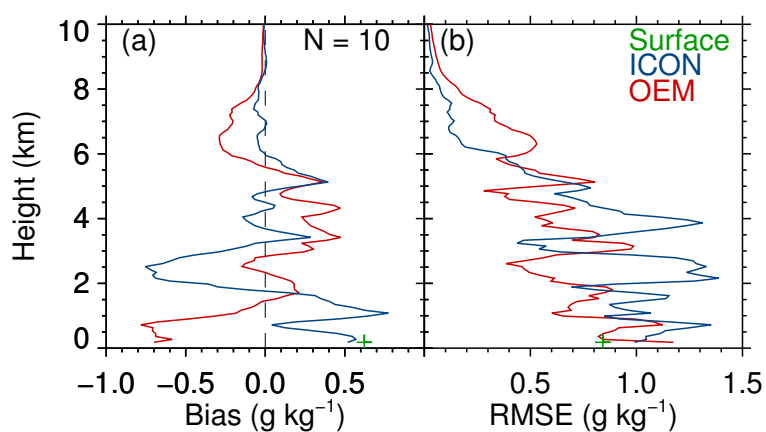


Figure 8.4: Statistical analysis: bias (a) and root mean square error (RMSE) to RS (b), respectively, for both OEM (red) and ICON (blue) based on the 10 RS on 25 April 2013. Additionally, the bias of the surface humidity to RS is marked by a green plus symbol. The sample size is given by the number.

indicates that the OEM has a high potential in evaluating climate and forecast models. An evaluation offers the possibilities to improve the parametrisations of physical processes with water vapour participation. Nevertheless, the sample size is too small to provide a robust assessment of the model uncertainties in this work.

9 Summary, conclusion and outlook

In the frame of this work, a retrieval method has been developed to obtain a continuous time series of water vapour profiles from a combination of Raman lidar and microwave radiometer (MWR). Within the German research project High Definition Clouds and Precipitation for advancing Climate Prediction (HD(CP)²), the HD(CP)² Observational Prototype Experiment (HOPE) was conducted around Jülich. During HOPE, different remote sensing systems to measure water vapour, both active and passive, were deployed. A synergy between Raman lidar and MWR is beneficial because both instruments provide complementary water vapour information. Raman lidars usually have a very good vertical resolution of 30 m or even less. However, the lidar signal is strongly attenuated in liquid water clouds, disturbed by sun light and the lidar needs to be calibrated. In contrast, the MWR is not affected by liquid water clouds which are semi transparent in the microwave spectrum. The information of the vertical humidity distribution provided by the MWR is rather low. Hence, fine structures can not be observed. However, the integrated water vapour (IWV) from MWR can be observed with high accuracy and used to calibrate the Raman lidar. This work presents a calibration method providing results which are in good agreement with conventional methods based on radiosonde (RS) launches. The determined calibration factors are very stable with a relative error of 5 %. This enables the determination of water vapour profiles during all weather conditions except for precipitation. During clear sky cases, the Raman lidar can be calibrated simultaneously with the IWV from the collocated MWR, whereas during cloudy conditions the calibration factor from the last clear sky interval is used. Therefore, the lidar set-up should only be modified during clear sky conditions.

After calibrating the Raman lidar by means of the IWV from the collocated MWR, the two-step retrieval to derive water vapour profiles can be applied. In the first step, the Kalman filter combines the current lidar measurement with previous information that originates from the last analysed state. In case of cloudy conditions, the lidar profile is truncated at the cloud base. The Kalman filter enhances the truncated profile to the full height range (10 km). Additionally, the Kalman filter decreases the uncertainties within the overlap region of the lidar (surface up to 500 m). The complete water vapour profile serves as input (a priori) to the one-dimensional variational approach, also known as optimal estimation. A forward model simulates the brightness temperatures which would be observed by the MWR for the given atmosphere. The profile is iteratively modified according to its error bars until the modelled and the actually measured brightness temperatures sufficiently converge. In addition to the water vapour profile, its uncertainty is retrieved.

The functionality of the retrieval is explained based on case studies representing cloud free and cloudy conditions at the Leipzig Aerosol and Cloud Remote Observations System (LACROS) site in Krauthausen near Jülich during HOPE. Since the Raman lidar Polly^{XT} does not provide water vapour observations during the day, it is also separated between the presence and the absence of Raman lidar profiles. It is shown that the presence of lidar results in more accurate retrievals compared to RS, whereas retrievals without water vapour profiles from lidar are mainly driven by the MWR observation for example during daytime.

However, the two-step algorithm allows to retain structures from high vertically resolved lidar data to periods without lidar data.

A statistical analysis was conducted to assess the accuracy of the retrieval. Therefore, more than 200 RS launches during the HOPE campaign are used as reference profiles. During HOPE, the availability of full height water vapour profiles from lidar amounts to 17%. By applying the retrieval, the availability of water vapour profiles can be enhanced to 60%. However, in the presence of full height lidar profiles, the application of the optimal estimation method (OEM) is actually not necessary. The differentiation between situations with full height, truncated or no Raman lidar profile, respectively, presents the enormous improvement of the instrument synergy. A comparison to RS profiles indicates a positive bias below 2 km and a negative bias above 2 km. This bias can be explained by several sources of uncertainties. First, the distance of ~ 4 km between LACROS and the RS launch station as well as RS drift can result in the observation of different air masses. Second, RS may have dry biases [Miloshevich *et al.*, 2001]. And, finally, the forward model is a major contributing factor. Turner *et al.* [2009] presented that the modelled brightness temperatures strongly depend on the assumed absorption line shapes. The presented work illustrates the uncertainty that is introduced by using two different gas absorption codes, Rosenkranz (1998) and Liebe (1993). The Rosenkranz model is more suitable for the proposed retrieval resulting in smaller bias to RS and a smaller a posteriori uncertainty. The bias with respect to RS and the retrieved a posteriori uncertainty of the retrieved profiles clearly show that the application of the Kalman filter enormously improves the accuracy and quality of the retrieved mixing ratio profiles.

The retrieval can be applied by using lidar raw data (photon counts, Polly^{XT}) or calibrated profiles (BASIL, RAMSES). This enables manifold applications to different Raman lidars and facilitates the implementation into processing schemes for instrument synergy.

The amount of independent pieces of information that can be obtained by the OEM retrieval is given by the degree of freedom. In the presence of Raman lidar profiles, the a priori information has very small uncertainties. These cases are mostly driven by the a priori state resulting in a small degree of freedom for the retrieval (~ 0.3). In contrast, the absence of Raman lidar profiles represents a more uncertain a priori information. Therefore, the MWR observation dominates the retrieval with a larger degree of freedom (~ 2). In cases of truncated lidar profiles, the retrieved profile below the truncation is dominated by the a priori (lidar) and above by the MWR observation. It is demonstrated that the lower the truncation height of the lidar profiles the higher the degree of freedom.

Since the relative humidity is a useful quantity for the description of cloud formation and aerosol growth, the relative humidity has been determined from the derived profiles assuming different temperature profiles. For a routine retrieval of relative humidity, the retrieved mixing ratio profiles by OEM and temperature profiles from the collocated MWR are used. The bias to HOPE RS varies between -10 and 10% with a mean absolute bias of 4.7% . The RMSE amounts to around 10% below 1.5 km and increases to around 20% above 1.5 km.

The manifold application of the retrieval to various platforms using different instruments are demonstrated. The powerful lidar BASIL at the Jülich Observatory for Cloud Evolution (JOYCE) additionally enables the daytime observation of water vapour profiles up to around 3 km. The BASIL application clearly demonstrates that the accuracy during the day

can be increased by the presence of Raman lidar mixing ratio profiles even though they are truncated at around 3 km.

The application of the OEM in combination with ship-based observations aboard RV Polarstern provides a nearly complete cross section of the water vapour distribution. However, the results are more uncertain than for the LACROS application for several reasons. The results could be improved by enhancing the amount of RS launches over the Atlantic. Based on a more representative RS data set, statistical retrievals for each climate zone can be generated. This might improve the accuracy of the temperature profiles and finally decrease the OEM uncertainty.

The Richard Aßmann Observatory in Lindenberg provides a good opportunity for evaluating the retrieval based on the 24/7 Raman lidar observations with RAMSES. At RAO RS are operationally launched four times a day. Since RAMSES water vapour measurements are calibrated using the RS, a very small bias between retrieved profiles and RS was determined. This retrieval application provides very good results with small uncertainties also under cloudy conditions.

However, the application of the retrieval at LACROS, JOYCE and RAO results in the same bias shape forced by the forward model. This issue needs to be further investigated.

A further application of the retrieval is possible in the frame of Cloudnet, where continuous profiles of cloud parameters are derived from a combination of MWR, cloud radar and lidar. If a Raman lidar is available, also consistent water vapour profiles can be added to this framework. These instruments observed the atmosphere collocated and simultaneously at LACROS in Krauthausen during HOPE. Due to the presence of a Raman lidar, the vertical water vapour distribution can be implemented to the Cloudnet data set. Some differences between both Cloudnet and the usual LACROS application of the retrieval result in slight discrepancies which can be explained by different temperature profile assumptions and more uncertain surface humidity values. Nevertheless, the deliverables show the potential of the OEM for the routine observation of the cloudy troposphere.

Instrument synergy usually has limitations and drawbacks. The proposed retrieval could be significantly enhanced by adding a standard weather station to the supersite and by implementing its data to the Cloudnet data base. Another improvement could be achieved by applying a standardised MWR processing that provides consistent temperature profiles. Hence, this step would simplify the application of the OEM due the presence of MWR variables in the Cloudnet data set as brightness temperatures and IWV. In the near future, the OEM will be adapted to produce Cloudnet consistent data flags, illustrations and data in Cloudnet data product standard. Afterwards, the retrieval can be operated at more operational Cloudnet station with Raman lidar.

A MWR provides vertical temperature and water vapour information. *Barrera-Verdejo [2016]* combined a MWR with Raman lidar and made use of these information to provide temperature and relative humidity profiles. This approach offers the possibility of more accurate temperature information and could enable a more realistic saturation mixing ratio profile. Hence, a subsaturation constraint could significantly improve the accuracy of thermodynamic profiling.

After assessing the accuracy of the mixing ratio profiles from the OEM, the retrieval shows high potential to be used for model evaluation. Despite the low amount of ICON-LEM data until the completion of this work, a brief model evaluation based on OEM and RS is conducted. Although night time OEM profiles are mainly driven by the accurate full height lidar information, there is a difference of about 2 g kg^{-1} between ICON-LEM and OEM. These differences might be caused by ICON. However, the larger uncertainties of the OEM during the day hinder a comprehensive daytime analysis of discrepancies between model and OEM. The brief investigation of the discrepancies between OEM, ICON-LEM and RS indicates that the OEM has a high potential in evaluating climate and forecast models. Nevertheless, the sample size is too small to provide a robust assessment of the model uncertainties.

In future steps, the precipitation evaporation can be assessed by means of observed or retrieved temperature and humidity profiles. Those information can be used to improve the model parametrisations of physical processes with water vapour participation and finally to improve weather and climate predictions. Such studies are a major part of the HD(CP)² initiative¹.

Finally, all the possible and planned improvements as well as the produced algorithms enable the observation of a continuous time series of water vapour profiles with known uncertainties. Hence, a better knowledge of the water vapour distribution and the collocated and simultaneous monitoring of cloud microphysics within Cloudnet might improve the understanding of cloud formation, precipitation, evaporation and entrainment rates. In conclusion, one of the major uncertainties of the latest IPCC report [*Boucher et al., 2013*], cloud and precipitation formation as well as cloud dissipation, might be decreased.

¹<http://hdcp2.eu>

A Appendix

A.1 Forward model error induced by liquid water

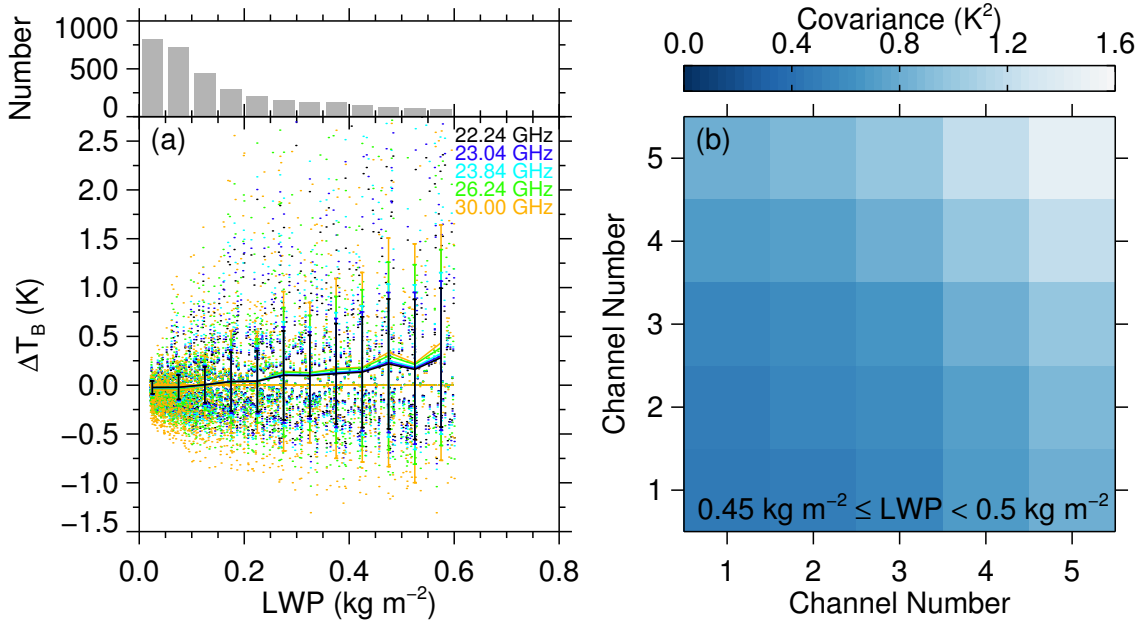


Figure A.1: **(a)** Brightness temperature difference as function of LWP (dots) using two different **LWC** assumptions. The colours indicate the according frequencies (top right). The means and the standard deviations per bin size are indicated by coloured lines and error bars, respectively. The bin size amounts to 0.05 kg m^{-2} . The number of occurrences is given in grey bars at the top. **(b)** Exemplary covariance matrix for an LWP between 0.45 kg m^{-2} and 0.5 kg m^{-2} . The channel numbers correspond with the TP/WVP-3000 frequencies given in **(a)** that means 1 refers to 22.24 etc. This analysis is based on a long term data set of RS from Lindenberg, Germany.

A.2 Additional formulas

Bias and root mean square error (*RMSE*) are calculated as follows:

$$Bias(i) = \frac{1}{N} \sum [q(i) - q_{\text{ref}}(i)] \quad (\text{A.1})$$

$$RMSE(i) = \frac{1}{N+1} \sum [q(i) - q_{\text{ref}}(i)]^2, \quad (\text{A.2})$$

with N being the number of profiles, i the according height and q the retrieved and the reference (ref) mixing ratio (in g kg^{-1}).

A.3 Statistical analysis: differentiation between three initial conditions

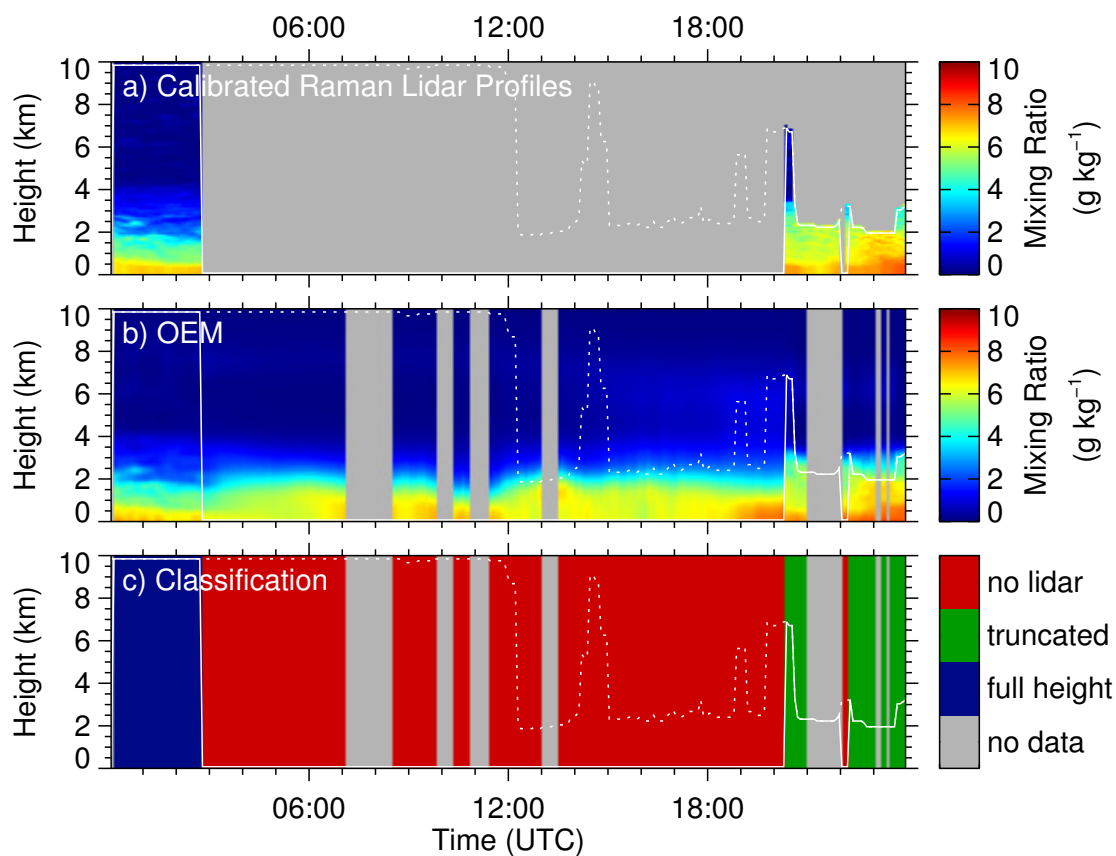


Figure A.2: Height-time display of mixing ratio profiles on 6 May 2013 during HOPE: (a) calibrated Raman lidar profiles (Polly^{XT}) and (b) optimal estimated profiles. (c) Classification according to the initial conditions depending on Raman lidar data availability. The solid and the dotted line indicate the truncation and the cloud base height, respectively.

List of Figures

2.1	HOPE 3D instruments map	6
2.2	Optical set-up of Polly ^{XT}	7
2.3	Polly ^{XT} cabinet with open doors	8
2.4	Absolute humidity weighting function for the HATPRO frequencies for a cloud free model atmosphere.	11
3.1	Contributions to the differential transmission	19
3.2	Modelled atmospheric extinction in the microwave spectrum	20
4.1	Sketch of the retrieval scheme	24
4.2	Correlation and covariance matrix for HOPE	25
4.3	Illustration of the radiative transfer model	27
4.4	Illustration of forward model error	29
4.5	Illustration of the optimal estimation method	31
4.6	Sketch of Levenberg-Marquardt approach	32
5.1	Overview of water vapour lidar calibration methods	36
5.2	Comparison between IWV from MWR and RS	37
5.3	Time series of Polly ^{XT} calibration factors during HOPE	38
5.4	Overview of Polly ^{XT} water vapour profiles during HOPE	39
5.5	Case study of calibrated profile on 5 May 2013	40
5.6	Statistical analysis of calibrated lidar profiles	41
5.7	HOPE map and bias between RS and Polly ^{XT} distinguished by different trajectories	42
5.8	Cloudy case study of calibrated lidar profiles on 16 April 2013	43
6.1	Cloud free case overview on 5 May 2013	46
6.2	Cloud free case without lidar data on 5 May 2013, 23:02 UTC	47
6.3	Comparison on a cloud free case on 5 May 2013	48
6.4	Cloud free case with lidar data on 5 May 2013, 07:02 UTC	49
6.5	Cloudy case overview on 21 April 2013	50
6.6	Comparison of a cloudy case on 21 April 2013	50
6.7	Height-time display of mixing ratio profiles during HOPE based on Polly ^{XT}	52
6.8	Synergy improvement LACROS	54
6.9	Comparison of different forward models	55
6.10	Regression analysis based on Polly ^{XT} at LACROS during HOPE	56
6.11	Histograms of the χ^2 test	57
6.12	Distribution of the degree of freedom depending on the truncation height	58
6.13	Degree of freedom as function of IWV	59
6.14	Temperature bias and RMSE	60
6.15	Relative humidity bias and RMSE	61

7.1	Height-time display of mixing ratio profiles during HOPE based on BASIL . . .	63
7.2	OEM bias and RMSE to RS based on BASIL at JOYCE during HOPE . . .	64
7.3	Map of the meridional transatlantic cruise of Polarstern	65
7.4	Overview of the water vapour distribution above the Atlantic	66
7.5	OEM bias and RMSE to RS based on Polly ^{XT} aboard of Polarstern	67
7.6	OEM bias and RMSE to RS based on RAMSES at RAO	68
7.7	Bias, RMSE and a posteriori uncertainty for the Cloudnet application	70
8.1	Height-time display of the mixing ratio profiles from OEM and ICON as well as their difference at LACROS on 25 April 2013.	74
8.2	Height-time display of the mixing ratio profiles from OEM and ICON as well as their difference at JOYCE on 25 April 2013.	74
8.3	OEM and ICON comparison to RS at JOYCE on 25 April 2013.	75
8.4	Bias and RMSE of both OEM and ICON to RS at JOYCE during HOPE . . .	76
A.1	Illustration of forward model error	81
A.2	Classification according to the initial conditions	82

List of Tables

2.1	Overview over the instrumentation at various experiments	5
4.1	Forward model errors	28
5.1	Summary of water vapour lidar calibration factors	38
5.2	Mixing ratio bias from calibrated profiles	42
6.1	Overview over the sample size during different conditions	53

Bibliography

- Ångström, A.: The parameters of atmospheric turbidity, *Tellus*, 16, 64–75, 1964.
- Abreu, P. et al.: Description of atmospheric conditions at the Pierre Auger Observatory using the Global Data Assimilation System (GDAS), *Astropart. Phys.*, 35, 591–607, doi:[10.1016/j.astropartphys.2011.12.002](https://doi.org/10.1016/j.astropartphys.2011.12.002), 2012.
- Adam, M. and Venable, D. D.: Systematic distortions in water vapor mixing ratio and aerosol scattering ratio from a Raman lidar, in: *Society of Photo-Optical Instrumentation Engineers (SPIE) Conference Series*, vol. 6750, p. 0, doi:[10.1117/12.738205](https://doi.org/10.1117/12.738205), 2007.
- Adam, M., Demoz, B. B., Whiteman, D. N., Venable, D. D., Joseph, E., Gambacorta, A., Wei, J., Shephard, M. W., Miloshevich, L. M., Barnet, C. D., Herman, R. L., Fitzgibbon, J., and Connell, R.: Water Vapor Measurements by Howard University Raman Lidar during the WAVES 2006 Campaign, *J. Atmos. Oceanic Technol.*, 27, 42, doi:[10.1175/2009JTECHA1331.1](https://doi.org/10.1175/2009JTECHA1331.1), 2010.
- Aires, F., Bernardo, F., and Prigent, C.: Atmospheric water-vapour profiling from passive microwave sounders over ocean and land. Part I: Methodology for the Megha-Tropiques mission, *Q. J. R. Meteorol. Soc.*, 139, 852–864, doi:[10.1002/qj.1888](https://doi.org/10.1002/qj.1888), 2013.
- Alexandrov, M. D., Schmid, B., Turner, D. D., Cairns, B., Oinas, V., Lacis, A. A., Gutman, S. I., Westwater, E. R., Smirnov, A., and Eilers, J.: Columnar water vapor retrievals from multifilter rotating shadowband radiometer data, *J. Geophys. Res. Atmos.*, 114, doi:[10.1029/2008JD010543](https://doi.org/10.1029/2008JD010543), d02306, 2009.
- Althausen, D., Engelmann, R., Baars, H., Heese, B., Ansmann, A., Müller, D., and Komppula, M.: Portable Raman lidar PollyXT for automated profiling of aerosol backscatter, extinction, and depolarization, *J. Atmos. Oceanic Technol.*, 26, 2366–2378, doi:[10.1175/2009JTECHA1304.1](https://doi.org/10.1175/2009JTECHA1304.1), 2009.
- Ansmann, A. and Müller, D.: Lidar and Atmospheric Aerosol Particles, in: *Lidar – Range Resolved Optical Remote Sensing of the Atmosphere*, edited by Weitkamp, C., vol. 102 of *Springer Series in Optical Sciences*, pp. 105–138, Springer Berlin/Heidelberg, 2005.
- Ansmann, A., Riebesell, M., and Weitkamp, C.: Measurement of atmospheric aerosol extinction profiles with a Raman lidar, *Opt. Lett.*, 15, 746–748, doi:[10.1364/OL.15.000746](https://doi.org/10.1364/OL.15.000746), 1990.
- Ansmann, A., Wandinger, U., Riebesell, M., Weitkamp, C., and Michaelis, W.: Independent measurement of extinction and backscatter profiles in cirrus clouds by using a combined Raman elastic-backscatter lidar, *Appl. Opt.*, 31, 7113–7131, doi:[10.1364/AO.31.007113](https://doi.org/10.1364/AO.31.007113), 1992.
- Ansmann, A., Tesche, M., Knippertz, P., Bierwirth, E., Althausen, D., Müller, D., and Schulz, O.: Vertical profiling of convective dust plumes in southern Morocco during SA-MUM, *Tellus*, 61B, 340–353, doi:[10.1111/j.1600-0889.2008.00384.x](https://doi.org/10.1111/j.1600-0889.2008.00384.x), 2009.

- Baars, H.: Aerosol profiling with lidar in the Amazon Basin during the wet and dry season 2008, Ph.D. thesis, Faculty of Physics and Geoscience, University of Leipzig, 2012.
- Baars, H., Ansmann, A., Engelmann, R., and Althausen, D.: Continuous monitoring of the boundary-layer top with lidar, *Atmos. Chem. Phys.*, 8, 7281–7296, doi:[10.5194/acp-8-7281-2008](https://doi.org/10.5194/acp-8-7281-2008), 2008.
- Baars, H., Kanitz, T., Engelmann, R., Althausen, D., Heese, B., Komppula, M., Preißler, J., Tesche, M., Ansmann, A., Wandinger, U., Lim, J.-H., Ahn, J. Y., Stachlewska, I. S., Amiridis, V., Marinou, E., Seifert, P., Hofer, J., Skupin, A., Schneider, F., Bohlmann, S., Foth, A., Bley, S., Pfüller, A., Giannakaki, E., Lihavainen, H., Viisanen, Y., Hooda, R. K., Pereira, S. N., Bortoli, D., Wagner, F., Mattis, I., Janicka, L., Markowicz, K. M., Achtert, P., Artaxo, P., Pauliquevis, T., Souza, R. A. F., Sharma, V. P., van Zyl, P. G., Beukes, J. P., Sun, J., Rohwer, E. G., Deng, R., Mamouri, R.-E., and Zamorano, F.: An overview of the first decade of PollyNET: an emerging network of automated Raman-polarization lidars for continuous aerosol profiling, *Atmos. Chem. Phys.*, 16, 5111–5137, doi:[10.5194/acp-16-5111-2016](https://doi.org/10.5194/acp-16-5111-2016), 2016.
- Baldauf, M., Seifert, A., Förstner, J., Majewski, D., Raschendorfer, M., and Reinhardt, T.: Operational Convective-Scale Numerical Weather Prediction with the COSMO Model: Description and Sensitivities, *Mon. Weather Rev.*, 139, 3887–3905, doi:[10.1175/MWR-D-10-05013.1](https://doi.org/10.1175/MWR-D-10-05013.1), 2011.
- Barrera-Verdejo, .: Ground Based Lidar and Microwave Radiometry Synergy for High Vertical Resolution Thermodynamic Profiling., Ph.D. thesis, Faculty of Mathematics and Natural Sciences, University of Cologne, 2016.
- Barrera-Verdejo, M., Crewell, S., Löhnert, U., Orlandi, E., and Di Girolamo, P.: Ground-based lidar and microwave radiometry synergy for high vertical resolution absolute humidity profiling, *Atmos. Meas. Tech.*, 9, 4013–4028, doi:[10.5194/amt-9-4013-2016](https://doi.org/10.5194/amt-9-4013-2016), 2016.
- Bernardo, F., Aires, F., and Prigent, C.: Atmospheric water-vapour profiling from passive microwave sounders over ocean and land. Part II: Validation using existing instruments, *Q. J. R. Meteorol. Soc.*, 139, 865–878, doi:[10.1002/qj.1946](https://doi.org/10.1002/qj.1946), 2013.
- Beyrich, F. and Engelbart, D. A. M.: Ten years of operational boundary-layer measurements at the Richard - Aßmann Observatory Lindenberg: The role of remote sensing, *IOP Conf. Ser.: Earth Environ. Sci.*, 1, 012 026, 2008.
- Bhavar, R., Di Girolamo, P., Summa, D., Flamant, C., Althausen, D., Behrendt, A., Kiemle, C., Bossler, P., Cacciani, M., Champollion, C., di Iorio, T., Engelmann, R., Herold, C., Müller, D., Pal, S., Wirth, M., and Wulfmeyer, V.: The water vapour intercomparison effort in the framework of the Convective and Orographically-induced Precipitation Study: airborne-to-ground-based and airborne-to-airborne lidar systems, *Q. J. R. Meteorol. Soc.*, 137, 325–348, doi:[10.1002/qj.697](https://doi.org/10.1002/qj.697), 2011.
- Bianco, L., Cimini, D., Marzano, F. S., and Ware, R.: Combining Microwave Radiometer and Wind Profiler Radar Measurements for High-Resolution Atmospheric Humidity Profiling, *J. Atmos. Oceanic Technol.*, 22, 949–965, doi:[10.1175/JTECH1771.1](https://doi.org/10.1175/JTECH1771.1), 2005.
- Bohren, C. F. and Clothiaux, E. E.: *Fundamentals of atmospheric radiation: an introduction with 400 problems*, John Wiley & Sons, doi:[10.1002/9783527618620](https://doi.org/10.1002/9783527618620), 2006.

- Bösenberg, J.: Differential-Absorption Lidar for Water Vapor and Temperature Profiling, in: Lidar – Range-Resolved Optical Remote Sensing of the Atmosphere, edited by Weitkamp, C., vol. 102 of *Springer Series in Optical Sciences*, pp. 241–271, Springer Berlin/Heidelberg, 2005.
- Bösenberg, J. and Linné, H.: Laser remote sensing of the planetary boundary layer, *Meteorol. Z.*, 11, 233–240, doi:[10.1127/0941-2948/2002/0011-0233](https://doi.org/10.1127/0941-2948/2002/0011-0233), 2002.
- Boucher, O., Randall, D., Artaxo, P., Bretherton, C., Feingold, G., Forster, P., Kerminen, V. M., Kondo, Y., Liao, H., Lohmann, U., Rasch, P., Satheesh, S. K., Sherwood, S., Stevens, B., and Zhang, X. Y.: Clouds and Aerosols, in: *Climate Change 2013: The Physical Science Basis. Contribution of Working Group I to the Fifth Assessment Report of the Intergovernmental Panel on Climate Change*, edited by Stocker, T., Qin, D., Plattner, G., Tignor, M., Allen, S., Boschung, J., Nauels, A., Xia, Y., Bex, V., and Midgley, P., Cambridge University Press, Cambridge, United Kingdom and New York, NY, USA, 2013.
- Bouniol, D., Protat, A., Delanoë, J., Pelon, J., Piriou, J. M., Bouyssel, F., Tompkins, A. M., Wilson, D. R., Morille, Y., Haefelin, M., O'Connor, E. J., Hogan, R. J., Illingworth, A. J., Donovan, D. P., and Baltink, H. K.: Using Continuous Ground-Based Radar and Lidar Measurements for Evaluating the Representation of Clouds in Four Operational Models, *J. Appl. Meteorol. and Clim.*, 49, 1971–1991, doi:[10.1175/2010JAMC2333.1](https://doi.org/10.1175/2010JAMC2333.1), 2010.
- Brocard, E., Philipona, R., Haefele, A., Romanens, G., Mueller, A., Ruffieux, D., Simeonov, V., and Calpini, B.: Raman Lidar for Meteorological Observations, RALMO - Part 2: Validation of water vapor measurements, *Atmos. Meas. Tech.*, 6, 1347–1358, doi:[10.5194/amt-6-1347-2013](https://doi.org/10.5194/amt-6-1347-2013), 2013.
- Brooks, I. M.: Finding Boundary Layer Top: Application of a Wavelet Covariance Transform to Lidar Backscatter Profiles, *J. Atmos. Oceanic Technol.*, 20, 1092–1105, doi:[10.1175/1520-0426\(2003\)020<1092:FBLTAO>2.0.CO;2](https://doi.org/10.1175/1520-0426(2003)020<1092:FBLTAO>2.0.CO;2), 2003.
- Browell, E. V., Wilkerson, T. D., and McIlrath, T. J.: Water vapor differential absorption lidar development and evaluation, *Appl. Opt.*, 18, 3474–3483, doi:[10.1364/AO.18.003474](https://doi.org/10.1364/AO.18.003474), 1979.
- Brückner, M., Pospichal, B., Macke, A., and Wendisch, M.: A new multispectral cloud retrieval method for ship-based solar transmissivity measurements, *J. Geophys. Res. Atmos.*, 119, 11,338–11,354, doi:[10.1002/2014JD021775](https://doi.org/10.1002/2014JD021775), 2014.
- Bruneau, D., Quaglia, P., Flamant, C., Meissonnier, M., and Pelon, J.: Airborne lidar LEANDRE II for water-vapor profiling in the troposphere. I. System description, *Appl. Opt.*, 40, 3450–3461, doi:[10.1364/AO.40.003450](https://doi.org/10.1364/AO.40.003450), 2001a.
- Bruneau, D., Quaglia, P., Flamant, C., and Pelon, J.: Airborne lidar LEANDRE II for water-vapor profiling in the troposphere. II. First results, *Appl. Opt.*, 40, 3462–3475, doi:[10.1364/AO.40.003462](https://doi.org/10.1364/AO.40.003462), 2001b.
- Bucholtz, A.: Rayleigh-scattering calculations for the terrestrial atmosphere, *Appl. Opt.*, 34, 2765–2773, doi:[10.1364/AO.34.002765](https://doi.org/10.1364/AO.34.002765), 1995.
- Bühl, J., Seifert, P., Wandinger, U., Baars, H., Kanitz, T., Schmidt, J., Myagkov, A., Engelmann, R., Skupin, A., Heese, B., Klepel, A., Althausen, D., and Ansmann, A.: LACROS: the Leipzig Aerosol and Cloud Remote Observations System, in: *Remote Sensing of Clouds*

- and the Atmosphere XVIII; and Optics in Atmospheric Propagation and Adaptive Systems XVI, vol. 8890 of *Proc. SPIE*, p. 889002, doi:[10.1117/12.2030911](https://doi.org/10.1117/12.2030911), 2013.
- Cimini, C., E. R., W., and A. J., G.: Temperature and Humidity Profiling in the Arctic Using Ground-Based Millimeter-Wave Radiometry and 1DVAR, *IEEE Trans. Geosci. Remote Sens.*, 48, 1381–1388, doi:[10.1109/TGRS.2009.2030500](https://doi.org/10.1109/TGRS.2009.2030500), 2010.
- Collis, R. T. H. and Russell, P. B.: Lidar measurement of particles and gases by elastic backscattering and differential absorption, in: *Laser Monitoring of the Atmosphere*, edited by Hinkley, E. D., pp. 71–151, doi:[10.1007/3-540-07743-X_18](https://doi.org/10.1007/3-540-07743-X_18), 1976.
- Cooney, J.: Remote Measurements of Atmospheric Water Vapor Profiles Using the Raman Component of Laser Backscatter, *J. Appl. Meteorol.*, 9, 182–184, doi:[10.1175/1520-0450\(1970\)009<0182:RMOAWV>2.0.CO;2](https://doi.org/10.1175/1520-0450(1970)009<0182:RMOAWV>2.0.CO;2), 1970.
- Crewell, S. and Löhnert, U.: Accuracy of boundary layer temperature profiles retrieved with multifrequency multiangle microwave radiometry., *IEEE Trans. Geosci. Remote Sens.*, 45, 2195–2201, doi:[10.1109/TGRS.2006.888434](https://doi.org/10.1109/TGRS.2006.888434), 2007.
- Delanoë, J. and Hogan, R. J.: A variational scheme for retrieving ice cloud properties from combined radar, lidar, and infrared radiometer, *J. Geophys. Res. Atmos.*, 113, doi:[10.1029/2007JD009000](https://doi.org/10.1029/2007JD009000), d07204, 2008.
- Di Girolamo, P., Summa, D., and Ferretti, R.: Multiparameter Raman lidar measurements for the characterization of a dry stratospheric intrusion event, *J. Atmos. Oceanic Technol.*, 26, 1742–1762, doi:[10.1175/2009JTECHA1253.1](https://doi.org/10.1175/2009JTECHA1253.1), 2009.
- Di Girolamo, P., Cacciani, M., Summa, D., Scoccione, A., De Rosa, B., Behrendt, A., and Wulfmeyer, V.: Characterization of Boundary Layer Turbulent Processes by the Raman Lidar BASIL in the frame of HD(CP)² Observational Prototype Experiment, *Atmos. Chem. Phys. Discuss.*, 2016, 1–50, doi:[10.5194/acp-2016-549](https://doi.org/10.5194/acp-2016-549), 2016.
- Dick, G., Gendt, G., and Reigber, C.: First experience with near real-time water vapor estimation in a German {GPS} network, *J. Atmos. Sol.-Ter. Phys.*, 63, 1295–1304, doi:[10.1016/S1364-6826\(00\)00248-0](https://doi.org/10.1016/S1364-6826(00)00248-0), 2001.
- Dionisi, D., Congeduti, F., Liberti, G. L., and Cardillo, F.: Calibration of a Multichannel Water Vapor Raman Lidar through Noncollocated Operational Soundings: Optimization and Characterization of Accuracy and Variability, *J. Atmos. Oceanic Technol.*, 27, 108–121, doi:[10.1175/2009JTECHA1327.1](https://doi.org/10.1175/2009JTECHA1327.1), 2010.
- Dirksen, R. J., Sommer, M., Immler, F. J., Hurst, D. F., Kivi, R., and Vömel, H.: Reference quality upper-air measurements: GRUAN data processing for the Vaisala RS92 radiosonde, *Atmos. Meas. Tech.*, 7, 4463–4490, doi:[10.5194/amt-7-4463-2014](https://doi.org/10.5194/amt-7-4463-2014), 2014.
- Ebell, K., Löhnert, U., Crewell, S., and Turner, D. D.: On characterizing the error in a remotely sensed liquid water content profile, *Atmos. Res.*, 98, 57–68, doi:[10.1016/j.atmosres.2010.06.002](https://doi.org/10.1016/j.atmosres.2010.06.002), 2010.
- Ebell, K., Crewell, S., Löhnert, U., Turner, D. D., and O’Connor, E. J.: Cloud statistics and cloud radiative effect for a low-mountain site, *Q. J. R. Meteorol. Soc.*, 137, 306–324, doi:[10.1002/qj.748](https://doi.org/10.1002/qj.748), 2011.

- Ebell, K., Orlandi, E., Hünerbein, A., Löhnert, U., and Crewell, S.: Combining ground-based with satellite-based measurements in the atmospheric state retrieval: Assessment of the information content, *J. Geophys. Res. Atmos.*, 118, 6940–6956, doi:[10.1002/jgrd.50548](https://doi.org/10.1002/jgrd.50548), 2013.
- Engelmann, R., Kanitz, T., Baars, H., Heese, B., Althausen, D., Skupin, A., Wandinger, U., Komppula, M., Stachlewska, I. S., Amiridis, V., Marinou, E., Mattis, I., Linné, H., and Ansmann, A.: The automated multiwavelength Raman polarization and water-vapor lidar PollyXT: the neXT generation, *Atmos. Meas. Tech.*, 9, 1767–1784, doi:[10.5194/amt-9-1767-2016](https://doi.org/10.5194/amt-9-1767-2016), 2016.
- England, M. N., Ferrare, R. A., Melfi, S. H., Whiteman, D. N., and Clark, T. A.: Atmospheric water vapor measurements: Comparison of microwave radiometry and lidar, *J. Geophys. Res.*, 97, 899–916, doi:[10.1029/91JD02384](https://doi.org/10.1029/91JD02384), 1992.
- Fernald, F. G.: Analysis of atmospheric lidar observations: some comments, *Appl. Opt.*, 23, 652–653, doi:[10.1364/AO.23.000652](https://doi.org/10.1364/AO.23.000652), 1984.
- Ferrare, R., Turner, D., Clayton, M., Schmid, B., Redemann, J., Covert, D., Elleman, R., Ogren, J., Andrews, E., Goldsmith, J. E. M., and Jonsson, H.: Evaluation of daytime measurements of aerosols and water vapor made by an operational Raman lidar over the Southern Great Plains, *J. Geophys. Res. Atmos.*, 111, doi:[10.1029/2005JD005836](https://doi.org/10.1029/2005JD005836), d05S08, 2006.
- Ferrare, R. A., Melfi, S. H., Whiteman, D. N., Evans, K. D., Schmidlin, F. J., and Starr, D. O.: A Comparison of Water Vapor Measurements Made by Raman Lidar and Radiosondes, *J. Atmos. Oceanic Technol.*, 12, 1177–1195, doi:[10.1175/1520-0426\(1995\)012<1177:ACOWVM>2.0.CO;2](https://doi.org/10.1175/1520-0426(1995)012<1177:ACOWVM>2.0.CO;2), 1995.
- Foth, A., Baars, H., Di Girolamo, P., and Pospichal, B.: Water vapour profiles from Raman lidar automatically calibrated by microwave radiometer data during HOPE, *Atmos. Chem. Phys.*, 15, 7753–7763, doi:[10.5194/acp-15-7753-2015](https://doi.org/10.5194/acp-15-7753-2015), 2015.
- Frisch, A. S., Feingold, G., Fairall, C. W., Uttal, T., and Snider, J. B.: On cloud radar and microwave radiometer measurements of stratus cloud liquid water profiles, *J. Geophys. Res.*, 103, 23 195, doi:[10.1029/98JD01827](https://doi.org/10.1029/98JD01827), 1998.
- Furumoto, J., Kurimoto, K., and Tsuda, T.: Continuous Observations of Humidity Profiles with the MU Radar–RASS Combined with GPS and Radiosonde Measurements, *J. Atmos. Oceanic Technol.*, 20, 23–41, doi:[10.1175/1520-0426\(2003\)020<0023:COOHPW>2.0.CO;2](https://doi.org/10.1175/1520-0426(2003)020<0023:COOHPW>2.0.CO;2), 2003.
- Gao, B.-C. and Kaufman, Y. J.: Water vapor retrievals using Moderate Resolution Imaging Spectroradiometer (MODIS) near-infrared channels, *J. Geophys. Res. Atmos.*, 108, doi:[10.1029/2002JD003023](https://doi.org/10.1029/2002JD003023), 4389, 2003.
- Gendt, G., Dick, G., Reibger, C., Tomassini, M., Liu, Y., and Ramatschi, M.: Near Real Time GPS Water Vapor Monitoring for Numerical Weather Prediction in Germany, *J. Meteorol. Soc. Jpn.*, 82, 361–370, doi:[10.2151/jmsj.2004.361](https://doi.org/10.2151/jmsj.2004.361), 2004.
- Goldsmith, J. E. M., Blair, F. H., Bisson, S. E., and Turner, D. D.: Turn-key Raman lidar for profiling atmospheric water vapor, clouds, and aerosols, *Appl. Opt.*, 37, 4979–4990, doi:[10.1364/AO.37.004979](https://doi.org/10.1364/AO.37.004979), 1998.

- Güldner, J. and Spänkuch, D.: Results of year-round remotely sensed integrated water vapor by ground-based microwave radiometry, *J. Appl. Meteorol.*, 38, 981–988, doi:10.1175/1520-0450(1999)038<0981:ROYRRS>2.0.CO;2, 1999.
- Han, Y. and Westwater, E. R.: Remote Sensing of Tropospheric Water Vapor and Cloud Liquid Water by Integrated Ground-Based Sensors, *Journal of Atmospheric and Oceanic Technology*, 12, 1050–1059, doi:10.1175/1520-0426(1995)012<1050:RSOTWV>2.0.CO;2, 1995.
- Han, Y., Westwater, E. R., and Ferrare, R. A.: Applications of Kalman Filtering to Derive Water Vapor Profiles from Raman Lidar and Microwave Radiometers, *J. Atmos. Oceanic Technol.*, 14, 480–487, doi:10.1175/1520-0426(1997)014<0480:AOKFTD>2.0.CO;2, 1997.
- Hartmann, D., Klein Tank, A., Rusticucci, M., Alexander, L., Brönnimann, S., Charabi, Y., Dentener, F., Dlugokencky, E., Easterling, D., Kaplan, A., Soden, B., Thorne, P., Wild, M., and Zhai, P.: Observations: Atmosphere and Surface, in: *Climate Change 2013: The Physical Science Basis. Contribution of Working Group I to the Fifth Assessment Report of the Intergovernmental Panel on Climate Change*, edited by Stocker, T., Qin, D., Plattner, G., Tignor, M., Allen, S., Boschung, J., Nauels, A., Xia, Y., Bex, V., and Midgley, P., Cambridge University Press, Cambridge, United Kingdom and New York, NY, USA, 2013.
- Heinze, R., Dipankar, A., Carbajal Henken, C., Moseley, C., Sourdeval, O., Trömel, S., Xie, X., et al.: Large-eddy simulations over Germany using ICON: A comprehensive evaluation, in press, 2016.
- Held, I. and Soden, B.: Water vapor Feedback and Global Warming, *Annu. Rev. Energy Environ.*, 25, 441–475, doi:10.1146/annurev.energy.25.1.441, 2000.
- Herold, C., Althausen, D., Müller, D., Tesche, M., Seifert, P., Engelmann, R., Flamant, C., Bhawar, R., and di Girolamo, P.: Comparison of Raman Lidar Observations of Water Vapor with COSMO-DE Forecasts during COPS 2007, *Weather Forecast.*, 26, 1056–1066, doi:10.1175/2011WAF2222448.1, 2011.
- Hewison, T. J.: Profiling Temperature and Humidity by Ground-based Microwave Radiometers, Ph.D. thesis, Department of Meteorology, University of Reading, 2006.
- Hewison, T. J. and Gaffard, C.: 1D-VAR Retrieval of Temperature and Humidity Profiles from Ground-based Microwave Radiometers, in: *IEEE MicroRad*, 2006, pp. 235–240, doi:10.1109/MICRAD.2006.1677095, 2006.
- Heymsfield, A. J. and Sabin, R. M.: Cirrus crystal nucleation by homogeneous freezing of solution droplets, *J. Atmos. Sci.*, 46, 2252–2264, doi:10.1175/1520-0469(1989)046<2252:CCNBHF>2.0.CO;2, 1989.
- Hobbs, P. V., Reid, J. S., Kotchenruther, R. A., Ferek, R. J., and Weiss, R.: Direct Radiative Forcing by Smoke from Biomass Burning, *Science*, 275, 1777–1778, doi:10.1126/science.275.5307.1777, 1997.
- Hogan, R. J., O’Connor, E. J., and Illingworth, A. J.: Verification of cloud-fraction forecasts, *Q. J. R. Meteorol. Soc.*, 135, 1494–1511, doi:10.1002/qj.481, 2009.

- Illingworth A. J., Hogan R. J., O'Connor E. J., Bouniol D., Delanoë J., Pelon J., Protat A., Brooks M. E., Gaussiat N., Wilson D. R., Donovan D. P., Baltink H. Klein, G.-J., v. Z., Eastment J. D., Goddard J. W. F., Wrench C. L., Haeffelin M., Krasnov O. A., Russchenberg H. W. J., Piriou J.-M., Vinit F., Seifert A., Tompkins A. M., and Willén U.: Cloudnet, *Bull. Amer. Meteorol. Soc.*, 88, 883–898, doi:[10.1175/BAMS-88-6-883](https://doi.org/10.1175/BAMS-88-6-883), 2007.
- Janssen, M. A.: Atmospheric remote sensing by microwave radiometry, John Wiley & Sons, 1993.
- Jiang, J. H., Su, H., Pawson, S., Liu, H., Read, W. G., Waters, J. W., Santee, M. L., Wu, D. L., Schwartz, M. J., Livesey, N. J., Lambert, A., Fuller, R. A., and Lee, J. N.: Five year (2004–2009) observations of upper tropospheric water vapor and cloud ice from MLS and comparisons with GEOS-5 analyses, *Journal of Geophysical Research: Atmospheres*, 115, doi:[10.1029/2009JD013256](https://doi.org/10.1029/2009JD013256), d15103, 2010.
- Kalisch, J.: Der Einfluss von Wolken auf den Strahlungsantrieb der Erde, Ph.D. thesis, Mathematisch–Naturwissenschaftliche Fakultät der Christian–Albrechts–Universität zu Kiel, 2011.
- Kalman, R. E.: A new approach to linear filtering and prediction problems, *J. basic Eng-T ASME*, 82, 35–45, doi:[10.1115/1.3662552](https://doi.org/10.1115/1.3662552), 1960.
- Kalman, R. E. and Bucy, R. S.: New results in linear filtering and prediction theory, *J. basic Eng-T ASME*, 83, 95–108, doi:[10.1115/1.3658902](https://doi.org/10.1115/1.3658902), 1961.
- Kanitz, T.: Vertical distribution of aerosols above the Atlantic Ocean, Punta Arenas (Chile), and Stellenbosch (South Africa): Characterization, solar radiative effects and ice nucleating properties., Ph.D. thesis, Faculty III Process Sciences, Technische Universität Berlin, 2012.
- Kanitz, T., Seifert, P., Ansmann, A., Engelmann, R., Althausen, D., Casiccia, C., and Rohwer, E. G.: Contrasting the impact of aerosols at northern and southern midlatitudes on heterogeneous ice formation, *Geophys. Res. Lett.*, 38, L17 802, doi:[10.1029/2011GL048532](https://doi.org/10.1029/2011GL048532), 2011.
- Kanitz, T., Ansmann, A., Engelmann, R., and Althausen, D.: North-south cross sections of the vertical aerosol distribution over the Atlantic Ocean from multiwavelength Raman/polarization lidar during Polarstern cruises, *J. Geophys. Res. Atmos.*, 118, 2643–2655, doi:[10.1002/jgrd.50273](https://doi.org/10.1002/jgrd.50273), 2013a.
- Kanitz, T., Ansmann, A., Seifert, P., Engelmann, R., Kalisch, J., and Althausen, D.: Radiative effect of aerosols above the northern and southern Atlantic Ocean as determined from shipborne lidar observations, *J. Geophys. Res. Atmos.*, 118, 12, doi:[10.1002/2013JD019750](https://doi.org/10.1002/2013JD019750), 2013b.
- Karstens, U., Simmer, C., and Ruprecht, E.: Remote sensing of cloud liquid water, *Meteorol. Atmos. Phys.*, 54, 157–171, doi:[10.1007/BF01030057](https://doi.org/10.1007/BF01030057), 1994.
- Klett, J. D.: Stable analytical inversion solution for processing lidar returns, *Appl. Opt.*, 20, 211–220, doi:[10.1364/AO.20.000211](https://doi.org/10.1364/AO.20.000211), 1981.
- Koop, T., Luo, B., Tsias, A., and Peter, T.: Water activity as the determinant for homogeneous ice nucleation in aqueous solutions, 406, 611–614, doi:[10.1038/35020537](https://doi.org/10.1038/35020537), 2000.

- Küchler, N., Turner, D. D., Löhnert, U., and Crewell, S.: Calibrating ground-based microwave radiometers: Uncertainty and drifts, *Radio Sci.*, 51, 311–327, doi:10.1002/2015RS005826, 2015RS005826, 2016.
- Leblanc, T., McDermid, I. S., and Walsh, T. D.: Ground-based water vapor raman lidar measurements up to the upper troposphere and lower stratosphere for long-term monitoring, *Atmos. Meas. Tech.*, 5, 17–36, doi:10.5194/amt-5-17-2012, 2012.
- Liebe, H. J., Hufford, G. A., and Manabe, T.: A model for the complex permittivity of water at frequencies below 1 THz, *I. J. Infrared Milli.*, 12, 659–675, 1991.
- Liebe, H. J., Hufford, G. A., and Cotton, M. G.: Propagation modeling of moist air and suspended water/ice particles at frequencies below 1000 GHz, in: In AGARD, Atmospheric Propagation Effects Through Natural and Man-Made Obscurants for Visible to MM-Wave Radiation 11 p (SEE N94-30495 08-32), vol. 1, 1993.
- Löhnert, U. and Crewell, S.: Accuracy of cloud liquid water path from ground-based microwave radiometry 1. Dependency on cloud model statistics, *Radio Sci.*, 38, 8041, doi:10.1029/2002RS002654, 2003.
- Löhnert, U. and Maier, O.: Operational profiling of temperature using ground-based microwave radiometry at Payerne: prospects and challenges, *Atmos. Meas. Tech.*, 5, 1121–1134, doi:10.5194/amt-5-1121-2012, 2012.
- Löhnert, U., Crewell, S., and Simmer, C.: An Integrated Approach toward Retrieving Physically Consistent Profiles of Temperature, Humidity, and Cloud Liquid Water., *J. Appl. Meteorol.*, 43, 1295–1307, doi:10.1175/1520-0450(2004)043<1295:AIATRP>2.0.CO;2, 2004.
- Löhnert, U., Crewell, S., Krasnov, O., O'Connor, E., and Russchenberg, H.: Advances in Continuously Profiling the Thermodynamic State of the Boundary Layer: Integration of Measurements and Methods, *J. Atmos. Oceanic Technol.*, 25, 1251–1266, doi:10.1175/2007JTECHA961.1, 2008.
- Löhnert, U., Turner, D. D., and Crewell, S.: Ground-Based Temperature and Humidity Profiling Using Spectral Infrared and Microwave Observations. Part I: Simulated Retrieval Performance in Clear-Sky Conditions, *J. Appl. Meteorol. and Clim.*, 48, 1017–1032, doi:10.1175/2008JAMC2060.1, 2009.
- Löhnert, U., Schween, J. H., Acquistapace, C., Ebell, K., Maahn, M., Barrera-Verdejo, M., Hirsikko, A., Bohn, B., Knaps, A., O'Connor, E., Simmer, C., Wahner, A., and Crewell, S.: JOYCE: Jülich Observatory for Cloud Evolution, *Bulletin of the American Meteorological Society*, 96, 1157–1174, doi:10.1175/BAMS-D-14-00105.1, 2015.
- Macke, A., Kalisch, J., Zoll, Y., and Bumke, K.: Radiative effects of the cloudy atmosphere from ground and satellite based observations, in: European Physical Journal Web of Conferences, vol. 9 of *European Physical Journal Web of Conferences*, p. 83, doi:10.1051/epjconf/201009006, 2010.
- Macke, A., Seifert, P., Baars, H., Beekmans, C., Behrendt, A., Bohn, B., Bühl, J., Crewell, S., Damian, T., Deneke, H., Düsing, S., Foth, A., Di Girolamo, P., Hammann, E., Heinze, R., Hirsikko, A., Kalisch, J., Kalthoff, N., Kinne, S., Kohler, M., Löhnert, U., Madhavan, B. L., Maurer, V., Muppa, S. K., Schween, J., Serikov, I., Siebert, H., Simmer, C., Späth, F., Steinke, S., Träumner, K., Wehner, B., Wieser, A., Wulfmeyer, V., and Xie, X.: The

- HD(CP)2 Observational Prototype Experiment HOPE – An Overview, *Atmos. Chem. Phys. Discuss.*, 2016, 1–37, doi:[10.5194/acp-2016-990](https://doi.org/10.5194/acp-2016-990), 2016.
- Madonna, F., Amodeo, A., Boselli, A., Cornacchia, C., Cuomo, V., D’Amico, G., Giunta, A., Mona, L., and Pappalardo, G.: CIAO: the CNR-IMAA advanced observatory for atmospheric research, *Atmos. Meas. Tech.*, 4, 1191–1208, doi:[10.5194/amt-4-1191-2011](https://doi.org/10.5194/amt-4-1191-2011), 2011.
- Maschwitz, G., Löhnert, U., Crewell, S., Rose, T., and Turner, D. D.: Investigation of ground-based microwave radiometer calibration techniques at 530 hPa, *Atmos. Meas. Tech.*, 6, 2641–2658, doi:[10.5194/amt-6-2641-2013](https://doi.org/10.5194/amt-6-2641-2013), 2013.
- Mattis, I., Ansmann, A., Althausen, D., Jaenisch, V., Wandinger, U., Müller, D., Arshinov, Y. F., Bobrovnikov, S. M., and Serikov, I. B.: Relative-humidity profiling in the troposphere with a Raman lidar., *Appl. Opt.*, 41, 6451–62, doi:[10.1364/AO.41.006451](https://doi.org/10.1364/AO.41.006451), 2002.
- Maurer, V., Kalthoff, N., Wieser, A., Kohler, M., Mauder, M., and Gantner, L.: Observed spatiotemporal variability of boundary-layer turbulence over flat, heterogeneous terrain, *Atmos. Chem. Phys.*, 16, 1377–1400, doi:[10.5194/acp-16-1377-2016](https://doi.org/10.5194/acp-16-1377-2016), 2016.
- Melfi, S. H.: Remote measurements of the atmosphere using Raman scattering, *Appl. Opt.*, 11, 1605–1610, doi:[10.1364/AO.11.001605](https://doi.org/10.1364/AO.11.001605), 1972.
- Melfi, S. H., Lawrence, J. D., and McCormick, M. P.: Observation of Raman scattering by water vapor in the atmosphere, *Appl. Phys. Lett.*, 15, 295–297, doi:[10.1063/1.1653005](https://doi.org/10.1063/1.1653005), 1969.
- Miloshevich, L. M., Vömel, H., Paukkunen, A., Heymsfield, A. J., and Oltmans, S. J.: Characterization and Correction of Relative Humidity Measurements from Vaisala RS80-A Radiosondes at Cold Temperatures, *J. Atmos. Oceanic Technol.*, 18, 135–156, doi:[10.1175/1520-0426\(2001\)018<0135:CACORH>2.0.CO;2](https://doi.org/10.1175/1520-0426(2001)018<0135:CACORH>2.0.CO;2), 2001.
- Miloshevich, L. M., Vömel, H., Whiteman, D. N., Lesht, B. M., Schmidlin, F. J., and Russo, F.: Absolute accuracy of water vapor measurements from six operational radiosonde types launched during AWEX-G and implications for AIRS validation, *J. Geophys. Res. Atmos.*, 111, doi:[10.1029/2005JD006083](https://doi.org/10.1029/2005JD006083), d09S10, 2006.
- Mona, L., Cornacchia, C., D’Amico, G., Di Girolamo, P., Pappalardo, G., Pisani, G., Summa, D., Wang, X., and Cuomo, V.: Characterization of the variability of the humidity and cloud fields as observed from a cluster of ground-based lidar systems, *Q. J. R. Meteorol. Soc.*, 133, 257–271, doi:[10.1002/qj.160](https://doi.org/10.1002/qj.160), 2007.
- Müller, D., Ansmann, A., Mattis, I., Tesche, M., Wandinger, U., Althausen, D., and Pisani, G.: Aerosol-type-dependent lidar ratios observed with Raman lidar, *J. Geophys. Res.*, 112, D16 202, doi:[10.1029/2006JD008292](https://doi.org/10.1029/2006JD008292), 2007.
- Myhre, G., Shindell, D., Bréon, F.-M., Collins, W., Fuglestvedt, J., Huang, J., Koch, D., Lamarque, J.-F., Lee, D., Mendoza, B., Nakajima, T., Robock, A., Stephens, G., Takemura, T., and Zhang, H.: Anthropogenic and Natural Radiative Forcing, in: *Climate Change 2013: The Physical Science Basis. Contribution of Working Group I to the Fifth Assessment Report of the Intergovernmental Panel on Climate Change*, edited by Stocker, T., Qin, D., Plattner, G., Tignor, M., Allen, S., Boschung, J., Nauels, A., Xia, Y., Bex, V., and Midgley, P., Cambridge University Press, Cambridge, United Kingdom and New York, NY, USA, 2013.

- Nash, J., Smout, R., Oakley, T., Pathack, B., and Kurnosenko, S.: WMO intercomparison of high quality radiosonde systems: Final report, WMO Rep., p. 118 pp, 2005.
- Nash, J., Oakley, T., Vömel, H., and Wei, L.: WMO Intercomparison of High Quality Radiosonde Systems, WMO Rep., 2011.
- Navas-Guzmán, F., Fernández-Gálvez, J., Granados-Muñoz, M. J., Guerrero-Rascado, J. L., Bravo-Aranda, J. A., and Alados-Arboledas, L.: Tropospheric water vapour and relative humidity profiles from lidar and microwave radiometry, *Atmos. Meas. Tech.*, 7, 1201–1211, doi:10.5194/amt-7-1201-2014, 2014.
- Newsom, R. K., Turner, D. D., Mielke, B., Clayton, M., Ferrare, R., and Sivaraman, C.: Simultaneous analog and photon counting detection for Raman lidar, *Appl. Opt.*, 48, 3903–3914, doi:10.1364/AO.48.003903, 2009.
- O'Dell, C. W., Wentz, F. J., and Bennartz, R.: Cloud Liquid Water Path from Satellite-Based Passive Microwave Observations: A New Climatology over the Global Oceans, *J. Climate*, 21, 1721–1739, doi:10.1175/2007JCLI1958.1, 2008.
- Phalippou, L.: Variational retrieval of humidity profile, wind speed and cloud liquid-water path with the SSM/I: Potential for numerical weather prediction, *Q. J. R. Meteorol. Soc.*, 122, 327–355, doi:10.1002/qj.49712253002, 1996.
- Pierce, D. W., Barnett, T. P., Fetzer, E. J., and Gleckler, P. J.: Three-dimensional tropospheric water vapor in coupled climate models compared with observations from the AIRS satellite system, *Geophys. Res. Lett.*, 33, doi:10.1029/2006GL027060, 121701, 2006.
- Pospichal, B.: Diurnal to annual variability of the Atmospheric Boundary Layer over West Africa: A comprehensive view by remote sensing observations, Ph.D. thesis, Faculty of Mathematics and Natural Sciences, University of Cologne, 2009.
- Randall, D. A., Wood, R. A., Bony, S., Colman, R., Fichefet, T., Fyfe, J., Kattsov, V., Pitman, A., Shukla, J., Srinivasan, J., Stouffer, R. J., Sumi, A., and Taylor, K. E.: Climate Change 2007: The Physical Science Basis. Contribution of Working Group I to the Fourth Assessment Report of the Intergovernmental Panel on Climate Change, in: *Climate Models and Their Evaluation*, edited by Solomon, S., Qin, D., Manning, M., Chen, Z., Marquis, M., Averyt, K. B., Tignor, M., and Miller, H. L., Cambridge University Press, United Kingdom and New York, NY, USA., Cambridge, United Kingdom and New York, NY, USA, 2007.
- Reichardt, J., Wandinger, U., Klein, V., Mattis, I., Hilber, B., and Begbie, R.: RAMSES: German Meteorological Service autonomous Raman lidar for water vapor, temperature, aerosol, and cloud measurements., *Appl. Opt.*, 51, 8111–31, doi:10.1364/AO.51.008111, 2012.
- Renaut, D., Pourny, J. C., and Capitini, R.: Daytime Raman-lidar measurements of water vapor, *Opt. Lett.*, 5, 233–235, doi:10.1364/OL.5.000233, 1980.
- Rodgers, C. D.: *Inverse Methods for Atmospheric Sounding - Theory and Practice*, vol. 2, World Scientific Publishing, 2000.
- Rose, T., Crewell, S., Löhnert, U., and Simmer, C.: A network suitable microwave radiometer for operational monitoring of the cloudy atmosphere, *Atmos. Res.*, 75, 183–200, doi:10.1016/j.atmosres.2004.12.005, 2005.

- Rosenkranz, P. W.: Water vapor microwave continuum absorption: A comparison of measurements and models, *Radio Sci.*, 33, 919–928, 1998.
- Sakai, T., Nagai, T., Nakazato, M., Matsumura, T., Orikasa, N., and Shoji, Y.: Comparisons of Raman Lidar Measurements of Tropospheric Water Vapor Profiles with Radiosondes, Hygrometers on the Meteorological Observation Tower, and GPS at Tsukuba, Japan, *J. Atmos. Oceanic Technol.*, 24, 1407–1423, doi:[10.1175/JTECH2056.1](https://doi.org/10.1175/JTECH2056.1), 2007.
- Sasano, Y., Browell, E. V., and Ismail, S.: Error caused by using a constant extinction/backscattering ratio in the lidar solution, *Appl. Opt.*, 24, 3929–3932, doi:[10.1364/AO.24.003929](https://doi.org/10.1364/AO.24.003929), 1985.
- Schneebeli, M.: Advancements in Ground-Based Microwave Remote Sensing of the Troposphere - Calibration, Data Retrieval and Applications, Ph.D. thesis, Institute of Applied Physics, University of Bern, 2009.
- Seemann, S. W., Li, J., Menzel, W. P., and Gumley, L. E.: Operational Retrieval of Atmospheric Temperature, Moisture, and Ozone from MODIS Infrared Radiances, *J. Appl. Meteorol.*, 42, 1072–1091, doi:[10.1175/1520-0450\(2003\)042<1072:OROATM>2.0.CO;2](https://doi.org/10.1175/1520-0450(2003)042<1072:OROATM>2.0.CO;2), 2003.
- Seifert, P.: Dust-related ice formation in the troposphere – A statistical analysis based on 11 years of lidar observations of aerosols and clouds over Leipzig, Ph.D. thesis, Faculty of Physics and Geoscience, University of Leipzig, 2010.
- Sengupta, M., Clothiaux, E. E., and Ackerman, T. P.: Climatology of Warm Boundary Layer Clouds at the ARM SGP Site and Their Comparison to Models, *J. Climate*, 17, 4760–4782, doi:[10.1175/JCLI-3231.1](https://doi.org/10.1175/JCLI-3231.1), 2004.
- Sherlock, V., Garnier, A., Hauchecorne, A., and Keckhut, P.: Implementation and validation of a Raman lidar measurement of middle and upper tropospheric water vapor, *Appl. Opt.*, 38, 5838–5850, doi:[10.1364/AO.38.005838](https://doi.org/10.1364/AO.38.005838), 1999.
- Simmer, C.: Satellitenfernerkundung hydrologischer Parameter der Atmosphäre mit Mikrowellen, Kovač, 1994.
- Soden, B. J. and Held, I. M.: An Assessment of Climate Feedbacks in Coupled Ocean Atmosphere Models, *J. Climate*, 19, 3354–3360, doi:[10.1175/JCLI3799.1](https://doi.org/10.1175/JCLI3799.1), 2006.
- Solheim, F., Godwin, J. R., Westwater, E. R., Han, Y., Keihm, S. J., Marsh, K., and Ware, R.: Radiometric profiling of temperature, water vapor and cloud liquid water using various inversion methods, *Radio Sci.*, 33, 393–404, doi:[10.1029/97RS03656](https://doi.org/10.1029/97RS03656), 1998.
- Stankov, B. B.: Multisensor Retrieval of Atmospheric Properties, *Bull. Amer. Meteorol. Soc.*, 79, 1835–1854, doi:[10.1175/1520-0477\(1998\)079<1835:MROAP>2.0.CO;2](https://doi.org/10.1175/1520-0477(1998)079<1835:MROAP>2.0.CO;2), 1998.
- Steinke, S., Eikenberg, S., Löhnert, U., Dick, G., Klocke, D., Di Girolamo, P., and Crewell, S.: Assessment of small-scale integrated water vapour variability during HOPE, *Atmos. Chem. Phys.*, 15, 2675–2692, doi:[10.5194/acp-15-2675-2015](https://doi.org/10.5194/acp-15-2675-2015), 2015.
- Stevens, B. and Bony, S.: Water in the atmosphere, *Phys. Today*, 66, 29, doi:[10.1063/PT.3.2009](https://doi.org/10.1063/PT.3.2009), 2013.

- Su, H., Waliser, D. E., Jiang, J. H., Li, J., Read, W. G., Waters, J. W., and Tompkins, A. M.: Relationships of upper tropospheric water vapor, clouds and SST: MLS observations, ECMWF analyses and GCM simulations, *Geophys. Res. Lett.*, 33, doi:10.1029/2006GL027582, 122802, 2006.
- Thome, K. J., Herman, B. M., and Reagan, J. A.: Determination of Precipitable Water from Solar Transmission, *J. Appl. Meteorol.*, 31, 157–165, doi:10.1175/1520-0450(1992)031<0157:DOPWFS>2.0.CO;2, 1992.
- Tompkins, A. M.: A Prognostic Parameterization for the Subgrid-Scale Variability of Water Vapor and Clouds in Large-Scale Models and Its Use to Diagnose Cloud Cover., *J. Atmos. Sci.*, 59, 1917–1942, doi:10.1175/1520-0469(2002)059<1917:APPFTS>2.0.CO;2, 2002.
- Turner, D. D. and Goldsmith, J. E. M.: Twenty-Four-Hour Raman Lidar Water Vapor Measurements during the Atmospheric Radiation Measurement Program’s 1996 and 1997 Water Vapor Intensive Observation Periods, *J. Atmos. Oceanic Technol.*, 16, 1062–1076, doi:10.1175/1520-0426(1999)016<1062:TFHRLW>2.0.CO;2, 1999.
- Turner, D. D., Ferrare, R. A., Brasseur, L. A. H., Feltz, W. F., and Tooman, T. P.: Automated Retrievals of Water Vapor and Aerosol Profiles from an Operational Raman Lidar, *J. Atmos. Oceanic Technol.*, 19, 37–50, doi:10.1175/1520-0426(2002)019<0037:AROWVA>2.0.CO;2, 2002.
- Turner, D. D., Lesht, B. M., Clough, S. A., Liljegren, J. C., Revercomb, H. E., and Tobin, D. C.: Dry Bias and Variability in Vaisala RS80-H Radiosondes: The ARM Experience, *J. Atmos. Oceanic Technol.*, 20, 117–132, doi:10.1175/1520-0426(2003)020<0117:DBAVIV>2.0.CO;2, 2003.
- Turner, D. D., Cadeddu, M. P., Lohnert, U., Crewell, S., and Vogelmann, A. M.: Modifications to the Water Vapor Continuum in the Microwave Suggested by Ground-Based 150-GHz Observations, *IEEE Transactions on Geoscience and Remote Sensing*, 47, 3326–3337, doi:10.1109/TGRS.2009.2022262, 2009.
- Twomey, S.: Aerosols, clouds and radiation, *Atmos. Environ.*, 25, 2435–2442, doi:10.1016/0960-1686(91)90159-5, 1991.
- Ulaby, F. T., Moore, R. K., Fung, A. K., and House, A.: Microwave remote sensing: active and passive, vol. 1, Addison-Wesley Reading, MA, 1981.
- van Heerwaarden, C. C. and de Arellano, J. V. G.: Relative Humidity as an Indicator for Cloud Formation over Heterogeneous Land Surfaces, *J. Atmos. Sci.*, 65, 3263–3277, doi:10.1175/2008JAS2591.1, 2008.
- Wandinger, U.: Raman Lidar, in: Lidar – Range-Resolved Optical Remote Sensing of the Atmosphere, edited by Weitkamp, C., vol. 102 of *Springer Series in Optical Sciences*, pp. 241–271, Springer Berlin/Heidelberg, 2005.
- Wandinger, U. and Ansmann, A.: Experimental determination of the lidar overlap profile with Raman lidar, *Appl. Opt.*, 41, 511–514, doi:10.1364/AO.41.000511, 2002.
- Wandinger, U., Seifert, P., Engelmann, R., Bühl, J., Wagner, J., Schmidt, J., Pospichal, B., Baars, H., Hiebsch, A., Kanitz, T., et al.: Observations of aerosol-cloud-turbulence interaction with integrated remote-sensing instrumentation, in: Proceedings of the 9th

- International Symposium on Tropospheric Profiling, edited by: Cimini, D., Di Girolamo, P., Marzano, FS, and Rizi, vol. 50, 2012.
- Wang, J. and Zhang, L.: Systematic Errors in Global Radiosonde Precipitable Water Data from Comparisons with Ground-Based GPS Measurements, *J. Climate*, 21, 2218–2238, doi:[10.1175/2007JCLI1944.1](https://doi.org/10.1175/2007JCLI1944.1), 2008.
- Wang, J., Rossow, W. B., Uttal, T., and Rozendaal, M.: Variability of Cloud Vertical Structure during ASTEX Observed from a Combination of Rawinsonde, Radar, Ceilometer, and Satellite, *Mon. Weather Rev.*, 127, 2484, doi:[10.1175/1520-0493\(1999\)127<2484:VOCVSD>2.0.CO;2](https://doi.org/10.1175/1520-0493(1999)127<2484:VOCVSD>2.0.CO;2), 1999.
- Ware, R., Carpenter, R., Güldner, J., Liljegren, J., Nehr Korn, T., Solheim, F., and Vandenberghe, F.: A multichannel radiometric profiler of temperature, humidity, and cloud liquid, *Radio Sci.*, 38, doi:[10.1029/2002RS002856](https://doi.org/10.1029/2002RS002856), 8079, 2003.
- Weckwerth, T. M., Parsons, D. B., Koch, S. E., Moore, J. A., Lemone, M. A., Demoz, B. B., Flamant, C., Geerts, B., Wang, J., and Feltz, W. F.: An Overview of the International H₂O Project (IHOP_2002) and Some Preliminary Highlights., *Bull. Amer. Meteorol. Soc.*, 85, 253–277, doi:[10.1175/BAMS-85-2-253](https://doi.org/10.1175/BAMS-85-2-253), 2004.
- Westbrook, C. D., Illingworth, A. J., O'Connor, E. J., and Hogan, R. J.: Doppler lidar measurements of oriented planar ice crystals falling from supercooled and glaciated layer clouds, *Q. J. R. Meteorol. Soc.*, 136, 260–276, doi:[10.1002/qj.528](https://doi.org/10.1002/qj.528), 2010.
- Westwater, E. R.: Remote sensing of tropospheric temperature and water vapor by integrated observing systems: The remote sensing lecture, *Bull. Amer. Meteorol. Soc.*, 78, 1991–2006, 1997.
- Westwater, E. R., Crewell, S., Mätzler, C., and Cimini, D.: Principles of surface-based microwave and millimeter wave radiometric remote sensing of the troposphere, *Quad. Soc. Ital. Elettromagnetismo*, 1, 50–90, 2005.
- Whiteman, D. N.: Examination of the traditional Raman lidar technique. II. Evaluating the ratios for water vapor and aerosols, *Appl. Opt.*, 42, 2593–2608, doi:[10.1364/AO.42.002593](https://doi.org/10.1364/AO.42.002593), 2003.
- Whiteman, D. N., Melfi, S. H., and Ferrare, R. A.: Raman lidar system for the measurement of water vapor and aerosols in the earth's atmosphere, *Appl. Opt.*, 31, 3068–3082, doi:[10.1364/AO.31.003068](https://doi.org/10.1364/AO.31.003068), 1992.
- Whiteman, D. N., Demoz, B., di Girolamo, P., Comer, J., Veselovskii, I., Evans, K., Wang, Z., Cadirola, M., Rush, K., Schwemmer, G., Gentry, B., Melfi, S. H., Mielke, B., Venable, D., and van Hove, T.: Raman Lidar Measurements during the International H₂O Project. Part I: Instrumentation and Analysis Techniques, *J. Atmos. Oceanic Technol.*, 23, 157–169, doi:[10.1175/JTECH1838.1](https://doi.org/10.1175/JTECH1838.1), 2006a.
- Whiteman, D. N., Demoz, B., di Girolamo, P., Comer, J., Veselovskii, I., Evans, K., Wang, Z., Sabatino, D., Schwemmer, G., Gentry, B., Lin, R.-F., Behrendt, A., Wulfmeyer, V., Browell, E., Ferrare, R., Ismail, S., and Wang, J.: Raman Lidar Measurements during the International H₂O Project. Part II: Case Studies, *J. Atmos. Oceanic Technol.*, 23, 170–183, doi:[10.1175/JTECH1839.1](https://doi.org/10.1175/JTECH1839.1), 2006b.

- Wirth, M., Fix, A., Mahnke, P., Schwarzer, H., Schrandt, F., and Ehret, G.: The airborne multi-wavelength water vapor differential absorption lidar WALES: system design and performance, *Appl. Phys. B*, 96, 201–213, doi:[10.1007/s00340-009-3365-7](https://doi.org/10.1007/s00340-009-3365-7), 2009.
- Wulfmeyer, V., Behrendt, A., Kottmeier, C., Corsmeier, U., Barthlott, C., Craig, G. C., Hagen, M., Althausen, D., Aoshima, F., Arpagaus, M., Bauer, H.-S., Bennett, L., Blyth, A., Brandau, C., Champollion, C., Crewell, S., Dick, G., di Girolamo, P., Dorninger, M., Dufournet, Y., Eigenmann, R., Engelmann, R., Flamant, C., Foken, T., Gorgas, T., Grzeschik, M., Handwerker, J., Hauck, C., Höller, H., Junkermann, W., Kalthoff, N., Kiemle, C., Klink, S., König, M., Krauss, L., Long, C. N., Madonna, F., Mobbs, S., Neininger, B., Pal, S., Peters, G., Pigeon, G., Richard, E., Rotach, M. W., Russchenberg, H., Schwitalla, T., Smith, V., Steinacker, R., Trentmann, J., Turner, D. D., van Baelen, J., Vogt, S., Volkert, H., Weckwerth, T., Wernli, H., Wieser, A., and Wirth, M.: The Convective and Orographically-induced Precipitation Study (COPS): the scientific strategy, the field phase, and research highlights, *Q. J. R. Meteorol. Soc.*, 137, 3–30, doi:[10.1002/qj.752](https://doi.org/10.1002/qj.752), 2011.
- Zängl, G., Reinert, D., Rípodas, P., and Baldauf, M.: The ICON (ICOsahedral Non-hydrostatic) modelling framework of DWD and MPI-M: Description of the non-hydrostatic dynamical core, *Q. J. R. Meteorol. Soc.*, 141, 563–579, doi:[10.1002/qj.2378](https://doi.org/10.1002/qj.2378), 2015.
- Zoll, Y.: Bestimmung des Flüssigwasserpfadens auf See mit Hilfe der passiven Mikrowellenradiometrie, Ph.D. thesis, Mathematisch–Naturwissenschaftliche Fakultät der Christian–Albrechts–Universität zu Kiel, 2012.

Nomenclature

Abbreviations

Abbr.	Description
1D-VAR	One-Dimensional VARiational
BASIL	University of Basilicata lidar system
COPS	Convective and Orographically-induced Precipitation Study
COSMO	COnsortium for Small-scale MOdelling
CV	Coefficient of Variation
DIAL	Differential Absorption Lidar
DWD	Deutscher WetterDienst, German weather service
FT	Free Troposphere
GCOS	Global Climate Observing System
GPS	Global Positioning System
GRUAN	GCOS Reference Upper-Air Network
HATPRO	Humidity And Temperature PROfiler
HD(CP) ²	High Definition Clouds and Precipitation for advancing Climate Prediction
HOPE	HD(CP) ² Observational Prototype Experiment
ICON	ICOsahedral Nonhydrostatic
IHOP	International H ₂ O Project
IOP	Intense Observation Period
IPCC	Intergovernmental Panel on Climate Change
IPT	Integrated Profiling Technique
ITCZ	InterTropical Convergence Zone
JOYCE	Jülich ObservatorY for Cloud Evolution
KIT	Karlsruhe Institute of Technology
LACROS	Leipzig Aerosol and Cloud Remote Observations System
LEM	Large Eddy Model

MWR	MicroWave Radiometer
NWP	Numerical Weather Prediction
OEM	Optimal Estimation Method
PBL	Planetary Boundary Layer
Polly ^{XT}	PORtabLe Lidar sYstem eXTended
RAMSES	Raman lidar for Atmospheric Moisture SEnSing
RAO	Richard Aßmann Observatory
RASS	Radio Acoustic Sounding System
RMSE	Root Mean Square Error
RS	Radiosonde
RTM	Radiative Transfer Model
RTO	Radiative Transfer Operator
RV	Research Vessel
UTC	Coordinated Universal Time

Acronym

Symbol	Description	Dimensions	Units
AOD _λ	Aerosol optical depth	–	–
IWV	Integrated water vapour	–	kg m ⁻²
LWC	Liquid water content	n	g m ⁻³
LWP	Liquid water path	–	g m ⁻²

Constants

Symbol	Description	Value	Units
c	Speed of light	$2.997\,925 \times 10^8$	m s ⁻¹
h	<i>Planck's</i> constant	6.6262×10^{-34}	J s
k_B	<i>Boltzmann's</i> constant	1.3805×10^{-23}	J K ⁻¹

Greek Symbols

Symbol	Description	Dimensions	Units
α_λ	Total extinction coefficient	m_y	m ⁻¹
α_ν^a	Volume absorption coefficient	–	m ⁻¹
α_λ^m	Molecular extinction coefficient	m_y	m ⁻¹

α_λ^P	Particle extinction coefficient	m_y	m^{-1}
β_λ	Total backscatter coefficient	m_y	$m^{-1} \text{ sr}^{-1}$
β_λ^m	Molecular backscatter coefficient	m_y	$m^{-1} \text{ sr}^{-1}$
β_λ^P	Particle backscatter coefficient	m_y	$m^{-1} \text{ sr}^{-1}$
χ^2	Statistical quantity	–	–
χ_{thr}^2	Threshold value for χ^2 test	–	–
ϵ	Emissivity	–	–
ϵ_t	Transition error	n	g kg^{-1}
η_λ	Receiver transmission	–	–
ϵ_y	Lidar measurement error	m_y	g kg^{-1}
λ	Wavelength	–	m
λ_0	Emitted wavelength	–	m
λ_R	Wavelength of the Raman-scattered light	–	m
ν	Frequency	–	GHz
Ω	Solid angle	–	sr
ρ	Density	–	kg m^{-3}
σ_{λ_R}	Scattering cross section	–	m^2
ϑ	Temperature	n	$^\circ\text{C}$
τ_ν	Optical depth	–	–
Θ	Elevation angle	–	$^\circ$

Roman Symbols

Symbol	Description	Dimensions	Units
\hat{A}_α	Extinction-related Ångström exponent	m_y	–
A	Averaging kernel matrix	$n \times n$	–
\mathbf{a}_{area}	Area of the averaging kernel matrix	n	–
A_T	Area of the receiver telescope	–	m^2
B_ν	Spectral <i>Planck</i> -function	–	$\text{W m}^{-2} \text{ sr}^{-1} \text{ nm}^{-1}$
d	Degree of Freedom	–	–
d_{acc}	Accumulated degree of Freedom	–	–

Nomenclature

e	Vapour pressure	–	hPa
E_λ	System efficiency	–	m^3
E_s	Saturation vapour pressure	–	hPa
$E_{s,\text{ice}}$	Saturation vapour pressure above ice	–	hPa
$E_{s,\text{liq}}$	Saturation vapour pressure above liquid water	–	hPa
F	Forward model	–	–
f	Density ratio between reference gas and dry air	–	–
\mathbf{G}_z	Gain, or contribution function, matrix	$m_z \times n$	$\text{g kg}^{-1} \text{K}^{-1}$
\mathbf{G}^{K}	Kalman gain, or contribution function, matrix	$m_y \times n$	–
H	Evolution operator	$m_y \times n$	–
I_ν	Monochromatic Radiance	–	$\text{W m}^{-2} \text{sr}^{-1} \text{nm}^{-1}$
J	Cost function	–	–
J_a	A priori costs	–	–
J_p	Penalty term (supersaturation)	–	–
\mathbf{J}_{sup}	Penalty function (supersaturation)	n	–
$\dot{\mathbf{J}}_{\text{sup}}$	First derivative of \mathbf{J}_{sup}	n	–
$\ddot{\mathbf{J}}_{\text{sup}}$	Second derivative of \mathbf{J}_{sup}	$n \times n$	–
J_z	Observation costs	–	–
K	Weighting function matrix (also Kernel or Jacobian)	$n \times m_y$	K kg g^{-1}
K	King factor	–	sr
k	Time index	–	–
M	Transition matrix	$n \times n$	–
M	Molar mass	–	kg mol^{-1}
m_ν	Number of frequencies	–	–
m_y	Length of the lidar measurement vector	–	–
m_z	Length of the observation vector	–	–
n	Length of the state vector	–	–

N_R	Molecule number density	m_y	m^{-3}
O	Overlap function	–	–
P_0	Emitted laser energy	–	W
\mathbf{p}	Pressure	n	hPa
P	Lidar signal / detected energy	–	W
q	Log-transformed mixing ratio	–	$g\ kg^{-1}$
q_{mr}	Mixing ratio	–	$g\ kg^{-1}$
q_s	Log-transformed surface mixing ratio	–	$g\ kg^{-1}$
q_{ice}^{sat}	Saturation mixing ratio above ice	–	$g\ kg^{-1}$
q_{lin}^{sat}	Linear transition function between q_{liq}^{sat} and q_{ice}^{sat}	–	$g\ kg^{-1}$
q_{liq}^{sat}	Saturation mixing ratio above liquid water	–	$g\ kg^{-1}$
r	Range	–	m
\mathbf{S}_a	A priori covariance matrix	$n \times n$	$g^2\ kg^{-2}$
$\mathbf{S}_{\delta z}$	Covariance matrix between \mathbf{z} and $\mathbf{F}(\hat{\mathbf{x}})$	$n \times n$	$g^2\ kg^{-2}$
\mathbf{S}^E	Covariance matrix of the estimated state	$n \times n$	$g^2\ kg^{-2}$
\mathbf{S}^F	Covariance matrix of the filtered state	$n \times n$	$g^2\ kg^{-2}$
S_λ^m	Molecular lidar ratio	m_y	sr
S_λ^p	Particle lidar ratio	m_y	sr
$\hat{\mathbf{S}}$	Covariance matrix of the retrieved state (a posteriori)	$n \times n$	$g^2\ kg^{-2}$
\mathbf{S}_t	State transition covariance matrix	$n \times n$	$g^2\ kg^{-2}$
\mathbf{S}_y	Lidar measurement covariance matrix	$m_y \times m_y$	$g^2\ kg^{-2}$
\mathbf{S}_z	Microwave radiometer measurement covariance matrix	$m_z \times m_z$	K^2
t_p	Temporal pulse length	–	s
T_B	Brightness temperature (Planck equivalent temperature)	–	K
$T_{B_{cos}}$	Cosmic background brightness temperature	–	K

Nomenclature

\mathbf{T}	Temperature	n	K
U	Relative humidity	–	–
\mathbf{x}	State vector	n	g kg^{-1}
\mathbf{x}_a	A priori state	n	g kg^{-1}
\mathbf{x}^{E}	Estimated state	n	g kg^{-1}
\mathbf{x}^{F}	Filtered state	n	g kg^{-1}
$\hat{\mathbf{x}}$	Retrieved state	n	g kg^{-1}
\mathbf{y}	Lidar measurement vector	m_y	g kg^{-1}
\mathbf{z}	Observation vector	m_z	–

Acknowledgements

This work was performed at the Leipzig Institute for Meteorology, University of Leipzig. It was funded by the Federal Ministry of Education and Research in Germany (BMBF) through the research programme High Definition Clouds and Precipitation for Climate Prediction HD(CP)².

A major part of the analyses done in this work is based on instrument observations. I would like to thank the assiduously working measurement teams from the LACROS, JOYCE and RAO and especially all supporters of the HOPE campaign. Special thanks to Holger Baars and Paolo Di Girolamo for their help in handling Polly^{XT} and BASIL capabilities and performances, respectively. Thanks to Patric Seifert for his help in implementing the retrieval into the Cloudnet processing.

Ein großes Dankeschön geht an alle Teilnehmer und Besatzungsmitglieder der Polarsternfahrt ANT-XXIX/10. Ihr wart immer für jeden Spaß zu haben und habt diesen Trip zu einem unvergesslichen Erlebnis werden lassen. Besonders möchte ich mich bei Basti bedanken, der über 5 Wochen mit mir eine Kabine geteilt hat und immer dafür gesorgt hat, dass ich mich wie Zuhause fühle.

Ein besonderer Dank geht natürlich an die Strahlungsgruppe des LIM, die mich immer bei Spieleabenden, Gruppenausflügen oder Pub-Quiz-Abenden aufgenommen haben. Das hat mir immer sehr viel Spaß gemacht. Ebenso möchte ich mich auch bei meinem Bürokollegen Frank, Marlen, Trismono und Felix bedanken. Die vielen Späße, Wett- und Tippspiele, sowie "einfach mal Quatsch machen" haben mir sehr durch anstrengende Phasen der Promotion geholfen. Aber auch die vielen Tipps und Hinweise für das Leben als Doktorand waren hilfreich um so manche Fehler zu vermeiden und sinnlose zeitintensive Arbeit zu sparen.

Natürlich auch Danke an Bernhard, meinen Betreuer, der sich immer unglaublich viel Zeit für mich, meine Ideen oder meine Probleme genommen hat. Danke für die gute Betreuung und die Unterstützung während meiner Doktorandenzeit.

Ich möchte mich auch bei allen anderen bedanken, die mich während meiner Promotion unterstützt haben, hier aber nicht namentlich erwähnt sind.

Großer Dank gilt auch meinen Eltern, die mir das Meteorologiestudium ermöglicht und mich immer unterstützt und ermutigt haben. Auch mein Bruder Marcus war mir eine große Hilfe, wenn es darum ging mal abzuschalten und abgelenkt zu werden.

Zuletzt danke ich meiner Freundin Emily, die immer für mich da war und sich geduldig meine Probleme angehört hat. Danke auch an meinen Sohn Julius, der es immer leicht geschafft hat mich nach einem anstrengenden Tag schnell abzulenken und meine Probleme vergessen zu lassen.

Andreas Foth

Curriculum Vitae

Personal Details

Date of birth and place August 11, 1985 in Blankenburg/ Harz, Germany
Citizenship German

Academic Education

- Since 01/2013 **PhD Student**
Leipzig Institute for Meteorology (LIM), University of Leipzig, Germany
Project framework: HD(CP)² – High Definition Clouds and Precipitation for advancing Climate Prediction
Dissertation thesis: *“Optimal estimation of water vapour profiles using a combination of Raman lidar and microwave radiometer”*.
- 2010–2012 **Master of Science in Meteorology**
Leipzig Institute for Meteorology (LIM), University of Leipzig, Germany
Master thesis: *“Bestimmung der vertikalen Aerosolverteilung über Punta Arenas, Chile (53.2°S, 70.9°W)”*.
- 2006–2010 **Bachelor of Science in Meteorology**
Leipzig Institute for Meteorology (LIM), University of Leipzig, Germany
Bachelor thesis: *“Stadtklima und Luftschadstoffe in Leipzig”*.

Work Experiences

- since 01/2013 **Scientific employee**
Leipzig Institute for Meteorology (LIM), University of Leipzig, Germany
Humidity profiling based on remote sensing.
- 09/2012–12/2012 and 09/2011–06/2012 **Research assistant**
Leibniz Institute for Tropospheric Research (TROPOS), Leipzig, Germany
Handling and maintenance of the TROPOS CALIPSO database.
- 07/2012–08/2012 **Research assistant**
Leibniz Institute for Tropospheric Research (TROPOS), Leipzig, Germany
Organization field of the 16th International Conference on Clouds and Precipitation (ICCP-2012).
- Summer term 2011, 2010 and 2009 **Student assistant**
Leipzig Institute for Meteorology (LIM), University of Leipzig, Germany
Supervising the “practical course meteorology”.

Andreas Foth: Ph.D. Thesis

Campaigns

- 03–04/2014 OCEANET, lidar and microwave radiometer observations aboard the research vessel Polarstern during the meridional transatlantic cruise ANT-XXIX/10

Publications

- 11/2016 Macke, A. et al. including **Foth, A.**: The HD(CP)² Observational Prototype Experiment HOPE – An Overview, *Atmos. Chem. Phys. Discuss.*, doi:10.5194/acp-2016-990, in review, 2016.
- 06/2016 **Foth, A.**, Baars, H., Di Girolamo, P., and Pospichal, B.: Continuous Time Series of Water Vapor Profiles from a Combination of Raman Lidar and Microwave Radiometer, *EPJ Web of Conferences*, 119, 05001, doi:10.1051/epjconf/201611905001, 2016.
- 10/2015 Baars, H. et al. including **Foth, A.**: An overview of the first decade of PollyNET: an emerging network of automated Raman- polarization lidars for continuous aerosol profiling, *Atmos. Chem. Phys.*, 16, 5111-5137, doi:10.5194/acp-16-5111-2016, 2016.
- 03/2015 **Foth, A.**, Baars, H., Di Girolamo, P., and Pospichal, B.: Water vapour profiles from Raman lidar automatically calibrated by microwave radiometer data during HOPE, *Atmos. Chem. Phys.*, 15, 7753-7763, doi:10.5194/acp-15-7753-2015, 2015.
- 07/2014 Kanitz, T., Ansmann, A., **Foth, A.**, Seifert, P., Wandinger, U., Engelmann, R., Baars, H., Althausen, D., Casiccia, C., and Zamorano, F.: Surface matters: limitations of CALIPSO V3 aerosol typing in coastal regions, *Atmos. Meas. Tech.*, 7, 2061-2072, doi:10.5194/amt-7-2061-2014, 2014.
- 06/2012 Kanitz T., **Foth, A.**, Wandinger U., Ansmann A., Engelmann R., Althausen D., Casiccia C., and Zamorano F.: CALIOP observations in coastal regions at southern midlatitudes compared to PollyXT measurements, Reviewed extended abstracts of the 26th International Laser Radar Conference (ILRC), Porto Heli, Greece, 25 - 29 June, 2012

Poster Presentations at Conferences

- 02/2016 **Foth, A.**, and Pospichal, B.: Continuous time series of water vapor profiles from a combination of Raman lidar and microwave radiometer, *Understanding Clouds and Precipitation*, Berlin, Germany, 15 - 19 February, 2016
- 07/2015 **Foth, A.**, Baars, H., Di Girolamo, P., and Pospichal, B.: Continuous time series of water vapor profiles from a combination of Raman lidar and microwave radiometer, 27th International Laser Radar Conference (ILRC), New York, NY, USA, 5 - 10 July, 2015